UNIVERSITY OF CALIFORNIA, MERCED

Insights into Quantum Optical Phenomena

A dissertation submitted in partial satisfaction of the
requirements for the degree
Doctor of Philosophy

in

Physics

by

Jonathan Daniel

Committee in charge:

Professor Lin Tian , Chair
Professor Jay Sharping
Professor Chih-Chun Chien

2024

The dissertation of Jonathan Daniel is approved, and it is acceptable in quality and form for publication on microfilm and electronically:

(Professor Jay Sharping)

(Professor Chih-Chun Chien)

(Professor Lin Tian , Chair)

University of California, Merced

2024

DEDICATION

I dedicate this dissertation to my recently passed grandfather John Daniel, grandmother Laini Freitas, aunt Constance Gottschall and uncle Melvin Warthen; each of them inspired me to pursue my wildest dreams, they may be gone but they will forever live on in my fondest memories and will continue to inspire me to be the best person I can be.

EPIGRAPH

The purpose of life is not to be happy. It is to be useful, to be honorable, to be compassionate, to have it make some difference that you have lived and lived well.

—Ralph Waldo Emerson

TABLE OF CONTENTS

LIST OF FIGURES

ACKNOWLEDGEMENTS

If there is one person I must thank it is my wife Lily. She is my biggest fan, supporter, motivator and critic. Not only does she pick me up when I am at my lowest, she makes sure that my head doesn't stray too far into the clouds. I would not be the person I am today without her influence and will be forever grateful.

I thank my parents Nancy Daniel and Joseph Daniel I could not have made it this far in life without their support and love. Throughout all the good and bad in life they stood by me with praise and words of encouragement.

The next person I would like to thank is my advisor Dr. Jay Sharping. From the moment he became my Cal-Bridge mentor he was nothing but encouraging. He supported me through the end of my undergraduate career and welcomed me into his lab as a graduate student. In moments I felt lost he showed me a path forward. I can not begin to imagine what a better mentor would look like and I hope that one day I will be able to have the same effect on my future students.

Following in the same vain I would like to thank Dr. Wing To. He was my research mentor during my undergraduate studies at CSU Stanislaus. He showed me what it meant to be a scientist and a good educator. Every opportunity that I was lucky enough to beneficent from is due to his constant mentorship and never waning dedication to helping his students.

Finally, I would like to thank all of the friends I made along the way. Each and everyone of you have had a tremendous impact on my life. If I tried to list all of you and all you have done for me my dissertation would never end. I hope the same holds true for you all and I hope we continue to support each other through the rest of our lives.

Jonathan K. Daniel

Email:
jonathan.daniel@csusb.edu
LinkedIn:
linkedin.com/in/jonathan-daniel-9102982b9

Education

University of California, Merced — Merced, CA
Ph.D. in Physics, Advisor: Dr. Jay Sharping — 2018–2024
- Thesis: "Insights into Quantum Optical Phenomena"

University of California, Merced — Merced, CA
M.S. in Physics — 2018–2021

California State University Stanislaus — Turlock, CA
B.S. in Physics — 2014–2018

Experience

California State University, San Bernardino — San Bernardino, California
Cal-Bridge Post Doctoral Fellow — 2024

University of California, Merced — Merced, California
Graduate Student Researcher — 2019-2021

University of California, Merced — Merced, California
Graduate Teaching Assistant — 2018,2019,2024

University of California, Merced — Merced, California
Instructor — 2021-2023

Publications and Presentations

1. **Daniel, J.**, "Insights into Quantum Optical Phenomena", *[Doctoral dissertation, University of California Merced] December 2024*
2. **Daniel, J.**, "Exploring the scalar Aharonov-Bohm effect through observations of a N-type system", *[Manuscript in preparation]*
3. **Daniel, J.**, "Exploring the AB effect through observations of an N-type system", *American Physics Society, Minneapolis, March 2024 (Oral Presentation)*

4. **Daniel, J.**, Morales, R., Kaur, D., "The Missing Piece of the Universe", *2016 Quadrennial Physics Congress, San Francisco, November 2016 (Poster)*

5. **Daniel, J.**, "Xenon Based Dark Matter Detection", *Stanford, August 2017 (Poster)*

6. **Daniel, J.**,"Xenon Based Dark Matter Detection", *CAMPARE, Cal-Poly Pomona, August 2015 (Invited speaker)*

7. **Daniel, J.**"Xenon Based Dark Matter Detection", *LSAMP, California State University Stanislaus, September 2017 (Invited speaker)*

8. **Daniel, J.**, "Direct Dark Matter Detection through the use of a Xenon Based TPC Detector", *American Astronomical Society, Washington D.C., January 2018*

Skills

- **Programming Languages:** Python, C++, Root, Labview, Maple , MATLAB, G-code, LaTeX
- **Instrumentation:** Free Space Optics, Fiber Optics,Low-Light Detection,High-Energy Particle Detection, Cryogenics, Circuitry
- **Computer Aided Design:** 3D modeling and printing, 2D drafting; certified in SolidWorks and AutoCAD
- **Computer Operating Systems:** Windows, various Linux distributions, and Macintosh

Scholarships and Awards

- Cal-Bridge Post-Doc Fellowship 2024–Current
- Cal-Bridge Graduate Fellowship 2024
- CADE Teaching Fellowship, 2022
- UC Merced Summer Research Fellowship 2019
- Cal-Bridge Graduate Fellowship 2018
- Cal-Bridge Scholarship 2017
- ONE PURPOSE Academic Scholarship 2017
- CAMPARE Research Internship 2017
- LSAMP Research Internship 2016–2017

ABSTRACT OF THE DISSERTATION

Insights into Quantum Optical Phenomena

by

Jonathan Daniel
Doctor of Philosophy in Physics
University of California Merced, 2024
Professor Lin Tian , Chair

The first chapter of this dissertation will focus on an overview of quantum optics, the history, and some of the key concepts important to experimentation in this field. We will dissect the broad field of quantum optics into five smaller categories; Beginning with photonics, the study of the fundamental particle of light known as a photon and their subsequent creation. Then the optical manipulation of light through various classic effects and techniques will be explored. We will then discuss photon statistics and its importance to the various methods of photon detection. Beginning to touch on the quantum realm we will delve into photon interactions with matter and the resultant quantum effects. This overview will be concluded by a dive into the theory of quantum entanglement and the generation of entangled photons through the non-linear optical process of spontaneous parametric down conversion. The general overview of quantum optics will be followed by a set of two studies on entanglement, the generation of bi-photon pairs, and the effect of outside stimulus on the entanglement in question. While neither of these studies were executed to completion, they resulted in the development of necessary knowledge and skills, while also laying the ground work for promising future research endeavors and technological applications. A third more in depth study into the electric scalar Aharonov-Bohm effect will be presented and is the vast majority of this PhD work. At the end of each experimental section important outcomes for the development of the field will be highlighted and possible technological appli-

cations will be proposed. The final section of this work will be used to present the next steps in my academic career and will outline the avenues for future efforts made to explore various experimental works.

Chapter 1

Introduction to Quantum Optics

Quantum optics is a branch of physics that deals with the interaction of light and matter at the level of individual quanta of energy, known as photons, and individual quantum states of matter. While the majority of this work considers the particle-like nature of light,for which we will be referring to 'photons', we will evaluate various phenomena resulting from the wave-like nature of light [2]. Exploring phenomena where the quantum nature of light and its interaction with matter are significant, often involving processes such as emission, absorption, transmission, reflection, and detection of photons [3, 4]. Quantum optics plays a crucial role in advancing technologies such as quantum computing, quantum cryptography, and high-precision measurement devices [5, 6]. It also provides insights into fundamental quantum phenomena and contributes to our understanding of the role of quantum mechanics in the interactions of light and matter. This chapter will introduce a few key concepts of quantum optics, explored in my research, followed by some of the related experimental techniques used to probe them. The subsequent chapters will consist of three studies into varying quantum optical phenomena. The first of which will be an exploration of the effect Doppler shift has on entangled photon pairs. Beginning with the generation of degenerate bi-photons through type-0 SPDC in a periodically polled potassium titanyl phosphate nonlinear crystal. Culminating in a proposed entanglement-enhanced LiDAR measurement. The second study will investigate the effects of quantum interference on bi-photons generated via four-wave mixing in a $\chi^{(3)}$ nonlinear fiber. With the outcome leveraging

a time-reversed Hong-Ou-Mandel effect measurement to discern the effect quantum interference has on bi-photon indistinguishability. The final and most robust study follows the development of a measurement scheme to probe the electric scalar Ahranov-Bohm effect via spectroscopic observations of Rubidium. The final chapter will layout the overall results of this Ph.D. work as well as establish motivation for continued work in these various areas. An extension of results of this research will be applied to current understanding of machine learning approaches with the hopes of developing a quantum optics based fully optical neural network. Resulting technological applications will be outlined along with a presentation of future research efforts into combining quantum optics and machine learning.

1.1 Photonics

Photonics was coined by John W. Cambel in 1954 as a 'new science' with the inspiration drawn from the relationship between electronics and electrical engineering [7]. Photonics represents the study of photons as the fundamental units of light, focusing on their generation, manipulation, and detection. Utilization of photonics-based techniques is crucial in the efforts to characterize any optical based system.

1.1.1 Photon Generation

The field of photonics was solidified with the creation of the maser and laser leading to a rapid expansion in optical based research [8]. Maser stands for Microwave Amplification by Stimulated Emission of Radiation, representing a system which produces coherent microwaves with wavelengths that are reproducible and stable, providing a nearly perfect clock source. The maser was first suggested by Joseph Webber then later developed by Charles Townes, James P. Gordan and Herbert J Zeiger in 1953 [9]. The working principle is based on creating a system in which a gain of energy due to stimulated molecular transitions outweighs any losses. The first demonstration of the maser is denoted in figure 1.1 where a molecular excitation media of ammonia, with well know transition of $E_1 \Rightarrow E_0, 0.79cm^{-1}$

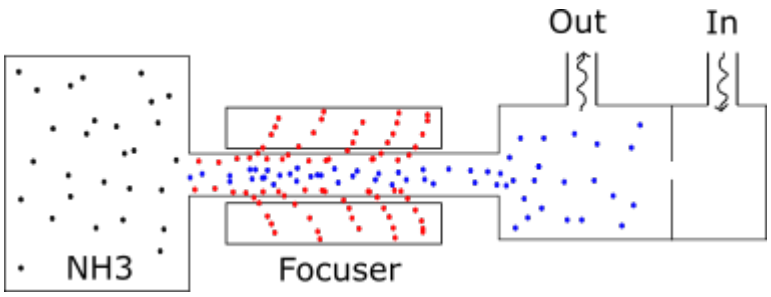

Figure 1.1: An example of the layout of a MASER, in which ammonia is placed in a resonant cavity,left portion of figure, and diffuses into an array of repeating positively and negatively charged rods,middle portion of figure. This array acts as a filter only allowing excited molecules to pass to another resonant cavity and the rest are diverted away. The excited molecules will result in an oscillating electromagnetic field and which is emitted at the output as microwaves, occuring in right side portion of the figure.

used as the transition of focus, is placed in a resonant cavity and allowed to diffuse into an array of oppositely repeating positively and negatively charged rods. The array acts as a filter and focuser causing any diffused molecules not in the excited state to be removed and any excited molecules to be focused into another cavity. The excited molecules will cause an oscillating electromagnetic field in the output cavity emitting microwaves at the output [10]. The discovery of the maser is the foundation of photonics and led to the creation of the laser, the premier tool in current optics research [11–13].

Similar to the maser, the term 'laser' stands for Light Amplication by Stimulated Emission of Radiation. The laser was experimentally realized by Theodore Maiman in 1960 based on the theoretical work of Charles H. Townes and Arthur Leonard Schawlow [14]. Unlike masers, lasers produce coherent 'light' at optical frequencies above 300GHz. Lasers allow for spatial and temporal coherence resulting in tightly focused beams with narrow frequency ranges. Just like the maser, the laser requires a population inversion in which the atoms of an excitation media are predominantly in an excited state and forced into resonate positive feedback loop. The common representation of a laser is depicted in figure 1.2. An excitation or gain media is used to amplify light of a specific wavelength and placed in an op-

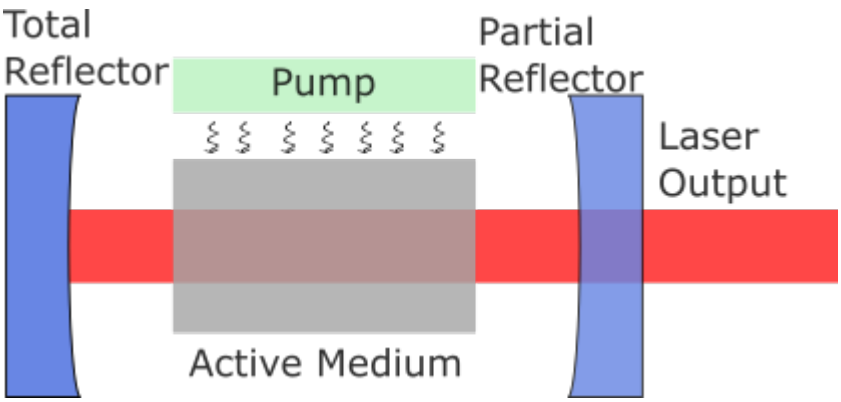

Figure 1.2: A simple figure of the operating principles of a LASER. An active medium, which amplifies light of a specific wavelength, is placed into an optical cavity and pumped. The cavity creates a feedback channel that causes stimulated emission in the medium and an overall amplification of the dominating frequency. One side of the cavity is partially transmissive allowing for output coupling.

tical cavity. The gain media is 'pumped' either electrically or optically by another light source. The optical cavity is formed by enclosing the gain media between two mirrors forming an optical feedback channel that enables stimulated emission in the gain media, each pass through the gain media results in amplification. Eventually the stimulated emission grows until there is a dominating frequency creating a coherent beam. One of the mirrors is partially transparent and allows for output coupling. Based on the geometry of the cavity and other applied optical elements, the various parameters of the beam can be controlled, such as the beam shape, polarization and wavelength. The invention of the laser allows for a robust optical light source that has seemingly infinite applications to scientific research [15–17].

1.2 Light Manipulation

Another important tool for optical research is the ability to manipulate and understand the various parameters of light. The main parameters of interest in the research presented in this manuscript are the frequency, polarization and beam shape of our optical sources. To characterize any light source or experimental result will require a study of all three parameters.

1.2.1 Frequency of Light

The frequency of light directly corresponds to the energy contained in a single photon. The energy of a photon is represented by $E_p = \frac{\hbar}{\omega}$, where $\hbar$ is plank's constant and ω is the frequency of light. As a result, manipulation of the frequency of light directly manipulates the energy of the light. Optical experiments are often based on specific preferred energy levels or transitions and therefore require accurate control of frequency. From atomic clocks to dazzling laser shows , from precise medical procedures to the detection of gravitational waves, the accurate manipulation of frequency is a necessity [18–21]. There are two main techniques used in this manuscript to control the frequency of light. The first and most used is frequency selection, mediated by optical elements or processes. The second method is to optically or mechanically shift the frequency of light.

1.2.2 Frequency Selection

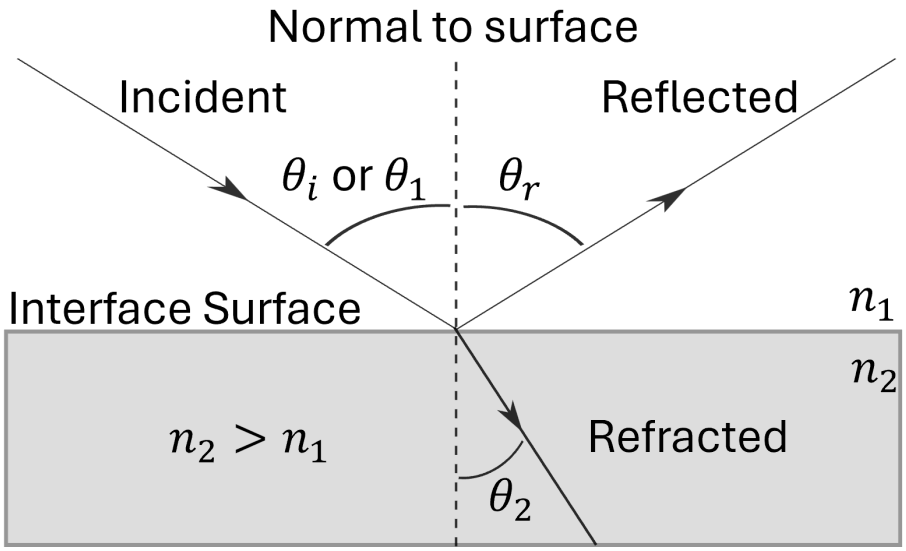

Figure 1.3: A model of reflection and refraction. An incident light beam interacts with an optical medium. The beam is both reflected and refracted. The angle of the reflected beam is directly equal to the angle of the incident beam with respect to the normal of the surface. The angle of the refracted beam follows Snell's law and is dependent on the ratio of the index of refraction at the interface.

The most common optical elements used for frequency selection are based on the basic principles of reflection and refraction [22]. Light of a specific frequency interacting with an object causes the electrons of the atoms contained in the object to begin vibrating at that specific frequency. If the vibrations are not resonant with the natural vibrational modes, the induced vibrations will be small in amplitude and short in duration. If the vibrations are passed to neighboring electrons through the bulk material the light is 'Transmitted' to the other side of the object and the material is deemed transparent to that specific frequency of light. If the vibrations are not passed to neighboring electrons the light is 'Reflected' and the material is determined to be opaque to that frequency of light [23]. Figure 1.3 demonstrates the path of reflected light can be determined by the law of reflection, $\theta_i = \theta_r$, stating that a light ray impinging on a surface will be reflected at an angle θ_r from the normal of the surface, equal to the original angle of incidence θ_i normal to the surface. The law of reflection holds true for non-planar surfaces and imperfect surfaces leading to diffuse reflection [24]. The transmission path of light through a material, also shown in figure 1.3, is slightly more complicated and follows Snell's Law , $n_1 \sin\theta_1 = n_2 \sin\theta_2$, where n_1 and n_2 represent the index of refraction for the first and second material, θ_1 and θ_2 represent the angles of the light's path relative to the normal of the surface. The index of refraction n of a material determines the amount the light's path is bent when entering the material, the value of the index of refraction can be thought of as a factor given by the ratio of values of speed and wavelength of light in a material when compared to that in a vacuum. The speed of light in a material $v = c/n$ and the wavelength $\lambda = \lambda_0/n$, where c and λ_0 are the speed of light and wavelength of light in a vacuum respectively. The index of refraction in a vacuum is then assumed to be equal to 1. Since the wavelength of light can vary in a material so too can the index of refraction. This means that for different frequencies of light, there will exist different pathways for specific values of frequency. This results in a splitting of frequencies known as dispersion and allows for a spatial based selection of frequency [25]. Mirrors, lenses, prisms and filters are some of the foundational optical elements used in this manuscript, all of them based on the working principles previously presented. The optical process of

absorption is also a tool used to selectively filter out frequencies. Absorption occurs when light interacts with an object in resonance with the natural frequency of vibrational modes of the electrons [26]. Since the process of absorption is based on the natural frequency of vibrational modes, different atoms will result in absorption of different frequencies. The process of absorption can then be leveraged to filter out specific frequencies of light. Another common form of frequency manipulation of light is attributed to the mechanical applications of the Doppler effect and Bragg scattering through the use of an acousto-optic modulator (AOM) [27]. The operating principles of an AOM are depicted in figure 1.4. The effective operation of an AOM requires the Bragg condition to be satisfied, which states that the interacting light must be incident at a specific angle perpendicular to an acoustic wave propagating through a bulk crystal [28]. The Bragg condition is determined by $\theta_B \approx \sin\theta_B = \lambda/\Lambda$ where θ_B is known as the Bragg angle, λ is the wavelength of light and Λ is the wavelength of the propagating acoustic wave. With the Bragg condition satisfied a diffraction pattern will emerge at the output of the AOM, following $2\Lambda \sin\theta_B = m\lambda$ Where m is the order of diffraction. Notably the angular separation of orders is roughly twice the Bragg angle and determined by $2\theta_B \approx \lambda/\Lambda$. The use of an AOM allows for tunability as well as spatial isolation of specific frequencies of light and hence is an integral part of many optical experiments [29–32].

1.2.3 Polarization

The polarization of light is another important parameter to be able to characterize and control [33]. The polarization of light is often described using transverse waves propagating in non-attenuating homogeneous isotropic media [34]. For non-transverse waves, those in anisotropic media such as birefringent crystals, polarization takes on more complex descriptions and results in interesting optical effects [35]. For simplicity this section will focus on the polarization of the simple transverse waves. Figure (1.4) depicts the commonly used description of a transverse electromagnetic wave with vertical polarization. The electric field $\vec{E}$ and the magnetic field $\vec{B}$ oscillate perpendicular to the direction of propagation

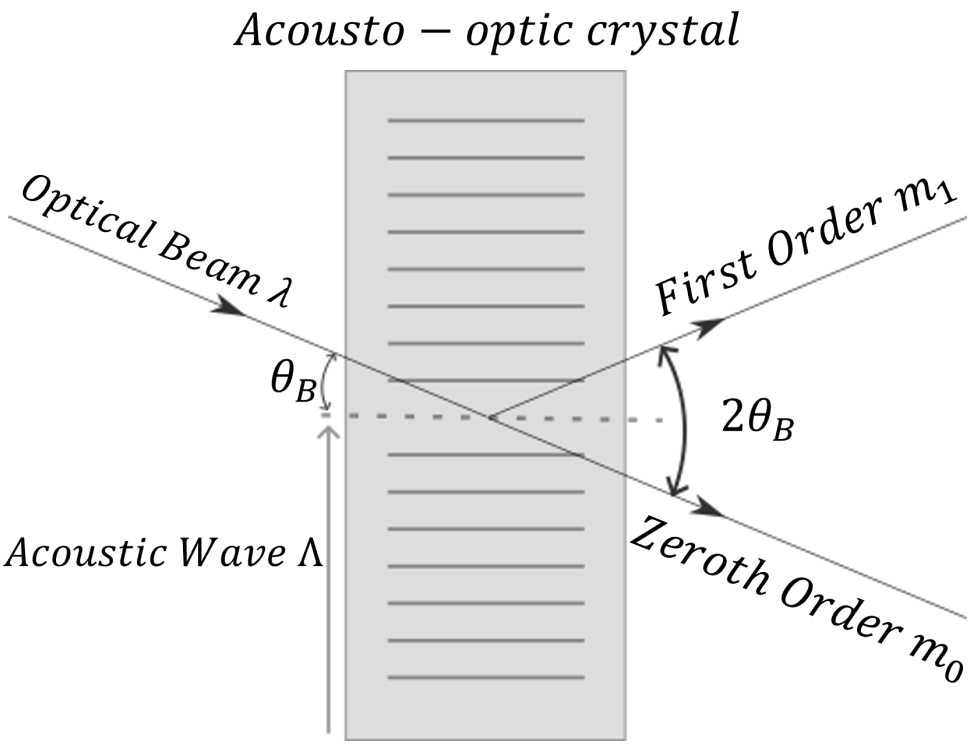

Figure 1.4: A diagram of the working principle of acousto-optic modulation in an optical crystal. An beam of light enters an optical crystal with an incident angle equal to the Bragg angle of the crystal. An acoustic wave is propagating in the crystal leading to Doppler shift of the optical frequency of the light beam.

of the electromagnetic wave. The 'polarization' direction is commonly determined by the direction of oscillation of the electric field. As a result, the commonly used types of polarization are defined as vertical, horizontal, circular and elliptical polarization [36]. Polarization can numerically be defined by pure polarization states using Jones vectors, these vectors are expressed in terms of a plane wave's complex amplitudes as a column vector following equation (1.1) [37]. Eqs. (1.2-1.5) represent a few of the common polarization states of light, starting with the linear x-polarization and ending with left-handed circular polarization.

$$\vec{E} = \begin{bmatrix} E_x \\ E_y \end{bmatrix} = \begin{bmatrix} A_x e^{i\delta_x} \\ A_y e^{i\delta_y} \end{bmatrix} \tag{1.1}$$

$$\hat{x} = \begin{bmatrix} 1 \\ \\ 0 \end{bmatrix} \tag{1.2}$$

$$\hat{y} = \begin{bmatrix} 0 \\ \\ 1 \end{bmatrix} \tag{1.3}$$

$$\hat{R} = \frac{1}{\sqrt{2}} \begin{bmatrix} 1 \\ \\ +i \end{bmatrix} \tag{1.4}$$

$$\hat{L} = \frac{1}{\sqrt{2}} \begin{bmatrix} 1 \\ \\ -i \end{bmatrix} \tag{1.5}$$

Polarization of light can be controlled by isolation or selection of states and manipulation of the oscillation direction of the electric field, where the optical effects of birefringent materials and the Faraday effect are often the mechanisms used [34]. The commonly used optical elements that employ these principles are wave-plates and optical isolators [38].

1.2.4 Beam Shaping

The final parameter of interest is the shape of the beam of light itself. By being able to control the shape of a light beam one is able to variably control the intensity, geometry and locality of any light-matter interaction [39]. The act of beam shaping requires all of the previously discussed principles of light manipulation. Based on our brief overview of optics we can utilize specific configurations of optical materials to produce interesting optical properties, allowing for control over the frequency, polarization and most importantly the pathway light travels through an object. Some of the most important optical elements used in beam shaping

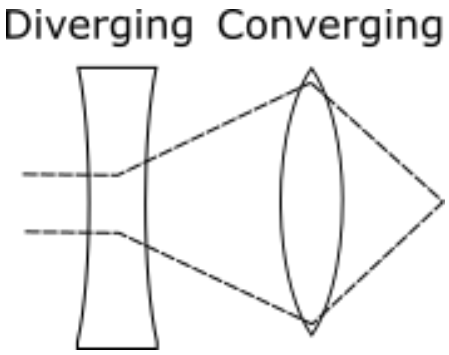

Figure 1.5: A light beam passing through a diverging (concave) lens, causing the beam diameter to expand. The beam then passes through a converging (convex) lens resulting in a focusing of the beam of light.

.

are lenses and based on their material makeup and geometry they can be used to control the diameter of a propagating beam of light [40]. Two of the most commonly used lenses are depicted in figure (1.5). The lenses themselves are used either to converge light beams towards a localized point, reducing the beam diameter, or create divergence of the light beams, increasing the beam diameter. For simple cases the path and size of a light beam propagating through a lens can be approximated based on the ideal thin lens. Equation (1.6) describes the radius of curvature of an optical wavefront as a function of distance from the lens. For more complex geometries or materials we can often rely on Gaussian beam propagation calculations, which we will later discuss in more detail [41].

$$\frac{1}{f} = \frac{1}{R(s)} + \frac{1}{R(s')} \tag{1.6}$$

Along with controlling the diameter of a beam of light we can also control the actual geometric shape of the beam itself [42]. Displayed in figures (1.6-1.7) are two common instrumentation used to manipulate the geometric shape of a beam of light utilizing an anamorphic prism pair and spatial filter. [43, 44].

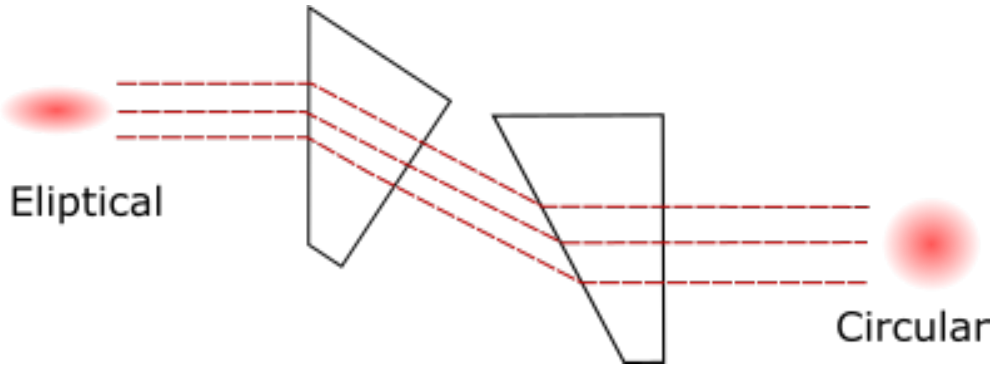

Figure 1.6: An example of an anamorphic prism pair changing the beam shape from an elliptical one to a circular one. The setup consists of two right angle prisms, which act on the propagating beam through the index of refraction. The beam is elongated along one axis and the other is kept fixed.

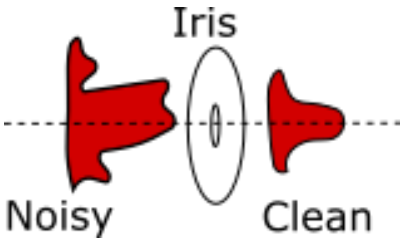

Figure 1.7: Example of a noisy beam being spatially filtered by an iris. Physically blocking the edges of the optical beam only allowing a specific portion of the beam to go through. The iris has a variable diameter and as a result can be used to selectively filter the beam.

1.3 Photon Statistics and Detection

While the manipulation of light is an integral part of optical science, being able to detect and classify light is what allows us to draw specific conclusions about its origins [45]. Observations of light at the fundamental level of individual photons is key to any understanding of optical processes [4]. This section will discuss the common methods and mechanisms used to detect and classify photons and their sources.

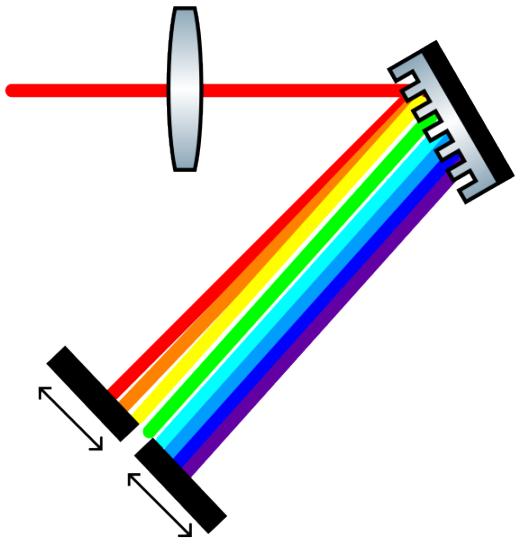

Figure 1.8: The basic operating principles of an optical spectrum analyzer. A multi-wavelength beam of light is split up into multiple propagating paths dependent on wavelength, this is done by a defraction grating. The multiple propagating beams can then be spatially isolated by a slit and independently measured by moving the slit corresponding to the desired beams path.

.

1.3.1 Detection Methods

Photon detection refers to the process of measuring the properties of individual photons [46]. The devices used to detect photons are often referred to as photodetectors and are classified by their mechanisms of detection [47]. Most methods of detection rely on the photoelectric effect, in which a photon deposits enough energy in an electron within a material liberating the electron from its atom [48, 49]. This liberated electron is known as a photoelectron and is utilized as an indirect measure of the original photon, often through current and timing measurements [50]. Semiconductor detectors rely on the photoconductive effect where the photons' energy excites the electrons from the valence band into the conduction band of the material, increasing the conductivity of the material [51]. The most commonly used

photodetectors are Photo-Multiplier Tubes (PMTs) and Avalanche Photodiodes (APDs). PMTs are vacuum tubes that amplify the current produced by incident photons through a photocathode and a series of dynodes [52]. APDs are semiconductor devices, where a single photon can trigger an avalanche of electron-hole pairs, resulting in a measurable current pulse [53]. Less common but more interesting forms of photon detection: Superconducting Nanowire Single-Photon Detectors (SNSPDs) and Quantum Dots. SNSPDs are ultra-sensitive detectors exploiting the superconducting properties of specific materials to detect single photons with high efficiency and low noise [54]. Quantum Dots are nanoscale structures that absorb photons and generate electron-hole pairs, enabling single-photon detection [55]. Combining photodetectors and frequency selective optical elements allows one to dissect multi-wavelength light. An Optical Spectrum Analyzer (OSA) is one such device used to determine the spectrum of wavelengths and the relative amplitudes of the various wavelengths [56]. The general working principle of a spectrum analyzer is based on a defraction grating which disperses multi-wavelength light based on its wavelength. Figure (1.8) represents the basic operating principles of an OSA. Being able to detect and measure photons allows us to characterize not only the photons themselves but the underlying process generating them. Another important characteristic quantity to consider is the statistical properties of light, which reveals information about the light source.

1.3.2 Photon Statistics

Photon statistics refers to the statistical properties of light, particularly concerning the distribution of photons in time, space, and other characteristics [57]. A statistical tool often used in optics is individual photon counting [58]. By observing the underlying numerical distribution of individual photons reveals information about the generation processes occurring at the light source. Light can generally be characterized by a Poissanian distribution, $P_n = \frac{\langle n \rangle^n}{n!} e^{-\langle n \rangle}$,falling into three relative regimes detailed in figure (1.9) [59]. Poissonian light is described by the variance of photon number equaling the mean value of photon number distribution, $\Delta n^2 = \langle n \rangle$, this implies a coherent light source such as a laser [60]. In some cases,

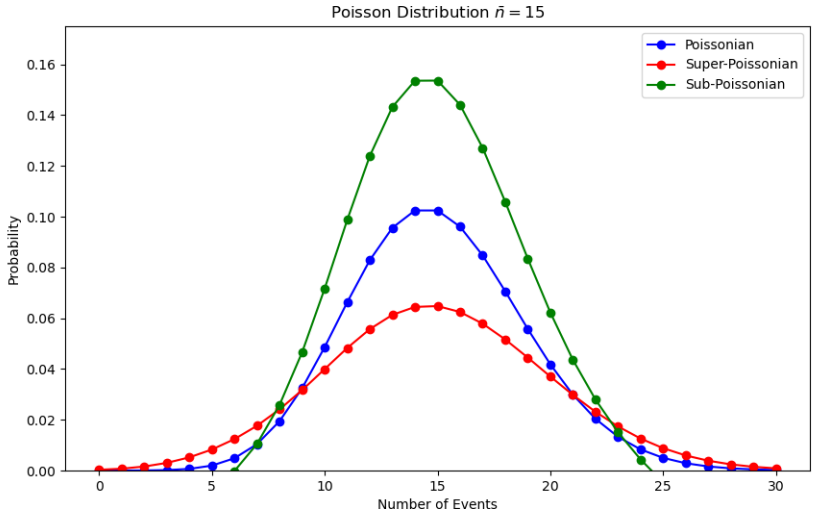

Figure 1.9: An example of the Poissonian distribution in photon statistics. The three regimes of the Poissonian distribution are overlaid depicting the probability of coincident detection events. Each regime is separated from the others based on the comparison between its mean value $\langle n \rangle$ and the width of the distribution or variance Δn^2

the photon number distribution can exhibit super-Poissonian statistics, where the variance of the photon number exceeds the mean, $\Delta n^2 > \langle n \rangle$. This can occur in chaotic or amplified light fields [61]. Conversely, sub-Poissonian statistics occur when the variance of the photon number is less than the mean, $\Delta n^2 < \langle n \rangle$, such as single photon emitters or squeezed states in quantum optics [62].

$$\gamma^{(1)}(\tau) = \frac{\langle E^*(t)E(t+\tau)\rangle}{\langle |E(t)|^2 \rangle} \tag{1.7}$$

$$g^{(2)}(\tau) = \frac{\langle I(t)I(t+\tau)\rangle}{\langle I(t)\rangle^2} \tag{1.8}$$

Another important statistical characteristic, photon correlation, examines how photons are correlated in time or space. The first and second order correlation functions, equations (1.7-1.8), are often used to determine the relative coherence of a light source [63]. Table (1.1) shows a few general trends and interpretations

Single Frequency Light	$\gamma^{(1)}(\tau) = e^{i\omega_0\tau}$	
Lorentzian Chaotic Light	$\gamma^{(1)}(\tau) = e^{i\omega_0\tau - \frac{\tau}{\tau_c}}$	
Gaussian Chaotic Light	$\gamma^{(1)}(\tau) = e^{i\omega_0\tau - \frac{\pi}{2}(\frac{\tau}{\tau_c})^2}$	
Coherent	$g^{(2)}(0) = 1$	$g^{(2)}(0) \geq g^{(2)}(\tau)$
Bunched	$g^{(2)}(0) > 1$	$g^{(2)}(0) \geq g^{(2)}(\tau)$
Anti-Bunched	$g^{(2)}(0) < 1$	$g^{(2)}(0) < g^{(2)}(\tau)$

Table 1.1: Interpretation of correlation functions.

of the correlation functions. First-order coherence is directly related to the visibility of interference patterns in optical experiments and is characterized by the first-order correlation function $\gamma^{(1)}(\tau)$, where τ is a time delay between measurements. Interference occurs when two or more coherent light beams (or parts of the same beam) overlap in space or time [25]. High first-order coherence leads to sharp interference fringes, while low coherence results in diminished or washed-out fringes [64]. Second-order coherence in optics provides insights into the statistical properties of light, particularly concerning the correlations between intensity fluctuations at different points in space or time. It is characterized by the second-order correlation function $g^{(2)}(\tau)$. The second-order correlation function at $\tau = 0$, $g^{(2)}(0)$, indicates whether photons tend to arrive together (bunching) or avoid arriving together (anti-bunching). Based on the grouping of photon arrivals we can infer how the light was generated [3]. Bunched light reveals that the source is chaotic, such as thermal radiation from black bodies [65]. Anti-bunched light suggests that a quantum mechanism is responsible for the photon generation, such as single photon emitting quantum dots [66]. Completely randomized grouping of light is expected for coherent light sources, such as lasers [67].

$$NEP = \frac{I_n}{R_i} \tag{1.9}$$

$$NEP(\lambda) = NEP_{min}\frac{R_{max}}{R(\lambda)} \tag{1.10}$$

$$P_{min} = NEP(\lambda)\Delta f^{\frac{1}{1}} \tag{1.11}$$

$$I_{sn} = [2q(I_d + I_{ph})\Delta f]^{\frac{1}{2}} \tag{1.12}$$

$$I_{jn} = \left[\frac{4kT\Delta f}{R_0}\right]^{\frac{1}{2}} \tag{1.13}$$

$$I_n = \left[I_{sn}^2 + I_{jn}^2 + I_{other}^2\right] \tag{1.14}$$

With the arrival time of photons being an important metric to the statistical study of light, one can argue that photon noise is an even more important quantity to characterize [68]. Photon noise arises due to the statistical fluctuations in the arrival times or intensities of photons and is the ultimate limitation of any discrete photon measurement. One common metric used to define the sensitivity of a detector to noise is given by the Noise Equivalent Power (NEP). NEP is often described as the optical power incident on a detector causing a signal-to-noise ratio (SNR) of 1 at a specific modulation frequency, wavelength and noise bandwidth [69]. Equation (1.9)represents the general NEP formulation, where I_n and R_i are the noise current and responsivity of the detector respectively. Equation (1.10) represents the minimum NEP at a specific wavelength, λ, where R_{max} is the maximum responsivity of the detector and $R(\lambda)$ is the responsivity at that wavelength. The minimum power is then determined by equation (1.11) where Δf is the noise measurement bandwidth. The total noise in a photodetector I_n ,equation (1.14), is determined by a combination of shot noise I_{sn}, thermal noise (or Johnson noise) I_{jn} and other noise sources, equation (1.13). The shot noise, equation (1.12), is a relationship between the fluctuations of the dark current I_d and photocurrent I_{ph} [66]. The thermal noise is related to the photodetector's resistance which thermally generates charge carriers. Often the dominating contributions come from shot and thermal noise. By utilizing NEP we can create an estimate on the noise limited minimum measurable power of any given photodetector [69].

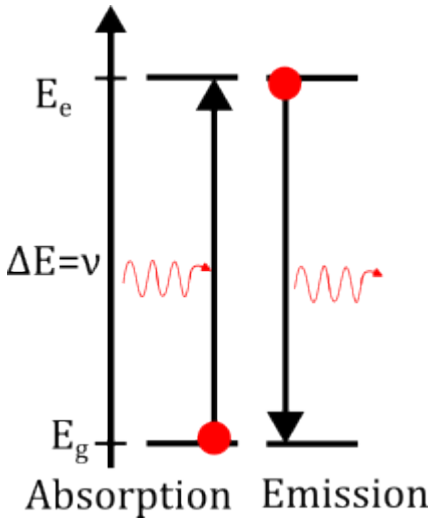

Figure 1.10: A two-level system in which a photon of frequency ν is absorbed and transitions the systems state to a higher energy level (Left). The excited system then spontaneously emits a photon of the same frequency to transition the state back to ground energy level(right).

1.4 Atom-Photon Interactions

The next fundamental concept in quantum optics is the physical interaction between atoms and photons in quantized systems, leading to phenomena like spontaneous emission, stimulated emission, and absorption [70]. The concept of absorption and emission in atom-photon interactions was first described by Bohr in 1913 [71]. Bohr suggested an atom will either absorb or emit a photon at an angular frequency equivalent to the separation of energy levels and dependent on the state of the atom itself, $E_2 - E_1 = \hbar\omega$. For simplification we can consider a single photon acting on a two-level atom with an angular frequency ω. In this simplified scenario, there are two likely outcomes based on the relationship between the photon's frequency and the natural frequency separation in the energy levels of the atom. If the photon's angular frequency matches that of the separation between energy states the photon is absorbed and the atom transitions to an excited state. To maintain a lower energy state an excited atom will emit a photon at an angular frequency equal to the state separation. The simplified process of absorption and emission can be seen in figure (1.10) where E_1 and E_2 are the ground and excited

states of an atom respectively. We can expand Bohr's frequency condition further by considering Einstein's 1917 work in describing the probability of absorption and emission [72]. Einstein defined two coefficients A and B. In a two-level system A_{12} corresponds to the probability of spontaneous absorption of a photon and A_{21} is the probability of spontaneous emission. The spontaneous emission coefficient can be defined by the decay lifetime from the excited state to the ground state, as $A_{21} = \frac{1}{\tau_{rad}}$. B_{12} and B_{21} are the coefficients for stimulated absorption and emission. Stimulated emission occurs when an excited atom is perturbed by a photon causing the atom to emit a second photon in phase with the original photon. The photons interfere constructively and as a result energy is emitted by the atom. Stimulated absorption is the inverse of this effect and corresponds to a photon perturbing an atom in the ground state, emitting a second photon in anti-phase, causing deconstructive interference and energy absorption [73]. We can describe the total rate of change of photons, in this two-level system, by summing the rates of all the processes, where N_ω represents the number of photons of frequency ω and n_i is the number of atoms in a specific state:

$$\left(\frac{dN_\omega}{dt}\right)_{absorption} = -B_{12}n_1N_\omega \tag{1.15}$$

$$\left(\frac{dN_\omega}{dt}\right)_{stimulatedemission} = B_{12}n_2N_\omega \tag{1.16}$$

$$\left(\frac{dN_\omega}{dt}\right)_{spontaneousemission} = A_{21}n_2 \tag{1.17}$$

$$\left(\frac{dN_\omega}{dt}\right)_{total} = B_{21}n_2N_\omega - B_{12}n_1N_\omega + A_{21}n_2 \tag{1.18}$$

For a steady state, in which the system is in equilibrium, the number of photons does not change:

$$B_{21}n_2N_\omega + A_{21}n_2 = B_{12}n_1N_\omega \tag{1.19}$$

Using the Boltzmann factor where k_B is the Boltzmann constant, g_i is the degeneracy of a given state and T is the temperature; we can obtain a probability ratio that only depends on the difference between energy levels [74]:

$$\frac{n_2}{n_1} = \frac{g_2}{g_1} \exp\left(\frac{-\hbar\omega}{k_B T}\right) \tag{1.20}$$

For a spontaneously emitting system we can apply Planck's law of radiation to find the energy density of the system at a given temperature resulting in equation (1.21). [75].

$$u(\omega) = \frac{\hbar\omega^3}{\pi^2 c^3} \frac{1}{\exp\left(\frac{\hbar\omega}{k_B T}\right) - 1} \tag{1.21}$$

Applying (1.19) and (1.20) to (1.21) we end up with an expression for the energy density of a two-level system expressed in Einstein coefficients:

$$u(\omega) = \frac{A_{21}}{B_{21}} \left(\frac{1}{\frac{B_{12} n_1}{B_{21} n_2} - 1}\right) \tag{1.22}$$

Noting the similarity between equation (1.21 and (1.22) we can find:

$$\frac{A_{21}}{B_{21}} = \frac{\hbar\omega^3}{\pi^2 c^3} \tag{1.23}$$

$$\frac{B_{12} n_1}{B_{21} n_2} = \exp\left(\frac{\hbar\omega}{k_B T}\right) \tag{1.24}$$

Simplifying equation (1.23) and applying (1.20) to (1.24) we end up with expressions for the Einstein coefficients:

$$A_{21} = \frac{\hbar\omega^3}{\pi^2 c^3} B_{21} \tag{1.25}$$

$$g_1 B_{12} = g_2 B_{21} \tag{1.26}$$

In this example we assumed that the system is in equilibrium and thus $\frac{n_2}{n_1} = 1$. Equilibrium is the simplest case, and all systems will tend towards this as a function of time, however an interesting case occurs when $\frac{n_2}{n_1} > 1$ and is analogous to what occurs in a laser. Since the emission rate is greater than that of absorption, the system is in a state of population inversion [76]. As a result, an applied source of photons with frequency $\omega = \frac{(E_2 - E_1)}{\hbar}$ will experience amplification due to stimulated emission. To maintain the population inversion state, optical pumping is often used otherwise the system will return to an equilibrium state after some time [77].

1.5 Quantum States of Light

Now that we have a grasp on photon generation, manipulation, detection and characterization we can begin exploring the quantum nature of light. Characterizing the quantum states of light requires quantum mechanical interpretations such as quantum states, superposition and entanglement. Though seemingly convoluted, the applications of the quantum interpretation of light leads to many useful applications such as quantum information processing, communication and sensing [78, 79].

1.5.1 Superposition

In 1924 Louis de Broglie theorized that matter can behave as a wave with a wavelength in relation to its momentum $\lambda = \frac{h}{p}$, where λ is the associated de Broglie wavelength, p is the momentum of the matter and h is Planck's constant [80]. Building on the interpretation of matter waves, Erwin Schrödinger developed a quantum analog to Newton's second law in which a particle could be described by an evolving wave equation, known as a wavefunction and symbolized by Ψ. The wavefunction describes the quantum state of a quantum system, for a position and time dependent wavefunction $\Psi(x, t)$ a complex value is assigned at each value of x for each time t. The mathematic representation of Schrödinger's work is a linear partial differential equation that describes the evolution of a wavefunction, $i\hbar\frac{d}{dt}|\Psi\rangle = \hat{H}|\Psi\rangle$ where $\hat{H}$ is the Hamiltonian and describes the total energy of the

system. The formulation is known as the time dependent Schrödinger equation, quickly becoming a pillar of quantum mechanics and ultimately leading to a Nobel prize [81]. Due to the linear nature of the Schrödinger equation any linear combination of solutions are also solutions to the Schrödinger equation, this feature leads to a phenomenon known as quantum superposition [82]. Simply put, quantum superposition is the ability of a quantum system to exist in multiple states at once, a concept that underpins many of the strange and powerful phenomena observed in quantum mechanics [83–85].

1.5.2 Entanglement

The term "entanglement" was originally coined by Schrödinger, translated from the German term "Verschränkung". This phenomenon implies that the total state of a composite system cannot be described by the product of the subsystems states. In summary, a state that is entangled cannot be solely described by its individual quantum states. Following one of Horodecki's examples we will explore entanglement as a quantum property of compound systems [86]. We will start with observing the "effect" of replacing the classical phase space by the abstract Hilbert space. This will result in a discontinuity in the description of composite systems. Here we will start off by considering a multipartite system containing n subsystems. When following the classical definition of a total state space, one can find the pure state as the *Cartesian* product of the n subsystems. This means the total state is always described by the product state of the n subsystems. Contrary, using the quantum formalism we find that the total Hilbert space H to be defined by the *tensor* product of the subsystems $H = \otimes_{l=1}^{n} H_l$. Using the superposition principle we can write the total state of the system as the following equation:

$$|\Psi\rangle = \sum_{i_1,\ldots,i_n} C_{i_1,\ldots,i_n} |i_1\rangle \otimes |i_2\rangle \otimes \ldots \otimes |i_n\rangle \tag{1.27}$$

It is apparent that in general one cannot describe the total state as a product of the individual states of the subsystems, therefore: $|\Psi\rangle \neq |\Psi_1\rangle \otimes |\Psi_2\rangle \otimes \ldots \otimes |\Psi_n\rangle$. With this we cannot assign single state vectors to any of the n subsystems. This

represents what we consider entanglement and in comparison to classical superposition we can construct arbitrarily large superpositions with only a small amount of physical resources. The entangled states represented on the left-hand side of equation(1.27) as $|\Psi\rangle$ are often a result of physical interactions. Entanglement can also be created through entanglement swapping, which is the application of the projection postulate [87].

Previously, we considered pure states but in practice we find that most cases we encounter are mixed states. The entanglement of mixed states can no longer be equivalent to being non-product states. Entanglement of a mixed state with n subsystems is defined through the inability to be described by a convex combination of product states. Entanglement of mixed states can be discerned by the following equation:

$$\rho \neq \sum_i p_i \rho_1^i \otimes ... \otimes \rho_n^i \tag{1.28}$$

States that do not satisfy the above equation are deemed separable. Despite this, it is difficult to discern if a state is separable by this definition alone. This difficulty to define separability distinctly is one of the main concerns in entanglement. It is important to note that the above metric is negative since a state is described as entangled if it cannot be written in the form (1.28) Horodecki gives an alternative approach to defining the entangled mixed state by a positive definition, referring to Masanes' et al. approach [88]. Suggesting, that entangled states are those that cannot be simulated through classical correlations. This take on entanglement can be defined by the behavior of the states rather than in terms of their preparation.

For bipartite systems the Hilbert space is represented as $H = H_1 \otimes H_2$ with $dim(H_1) = dim(H_2) = 2$ is spanned by four-Bell-state entangled basis:

$$|\Psi^{\pm}\rangle = \frac{1}{\sqrt{2}} \left(|0\rangle |1\rangle \pm |1\rangle |0\rangle\right) \tag{1.29}$$

$$|\Phi^{\pm}\rangle = \frac{1}{\sqrt{2}} \left(|0\rangle |0\rangle \pm |1\rangle |1\rangle\right) \tag{1.30}$$

These states are known as Einstein–Podolsky–Rosen (EPR) pairs or Bell states and have the property that when measuring only one of the subsystems one finds it with equal probability in state $|0\rangle$ or state$|1\rangle$ [89]. Knowing one of the states gives no knowledge of the other states, but as a whole the states are pure and give maximum knowledge about the overall system. Another important property of these basis is that applying the unitary operator on one of the two subsystems transforms from any Bell state to any one of the other three. The Bell states are special cases of bipartite entangled states in the Hilbert space $C^d \otimes C^d$, represented by:

$$|\Psi\rangle = U_A \otimes U_B \, |\Phi_d^+\rangle_{AB} \tag{1.31}$$

$$|\Phi_d^+\rangle = \frac{1}{\sqrt{d}} \sum_{i=1}^{d} |i\rangle \, |i\rangle \tag{1.32}$$

1.5.3 Entanglement via SPDC

Since we have covered the essentials of quantum entanglement and photon generation we can focus on one particular method used to produce entangled photons. Spontaneous Parametric Down Conversion (SPDC) is a phenomenon that produces entangled photon pairs [90]. As the name would suggest, SPDC is a spontaneous optical process that occurs in a nonlinear crystal, in which a pump photon is down-converted into two lower energy photons, often called the signal and idler photons, the higher frequency photon being dubbed the signal and the lower frequency photon the idler. The SPDC process is governed by energy and momentum conservation. Through energy conservation, the frequency of the signal ω_s and idler ω_i photons must add to be the pump frequency ω_p. Momentum conservation yields the wave vectors of the signal $\vec{k_s}$ and idler $\vec{k_i}$ photons must sum together to be the original wave vector of the pump photon $\vec{k_p}$. These conservation laws give us the two following equations:

$$\omega_p = \omega_s + \omega_i \tag{1.33}$$

$$\vec{k_p} = \vec{k_s} + \vec{k_i} \tag{1.34}$$

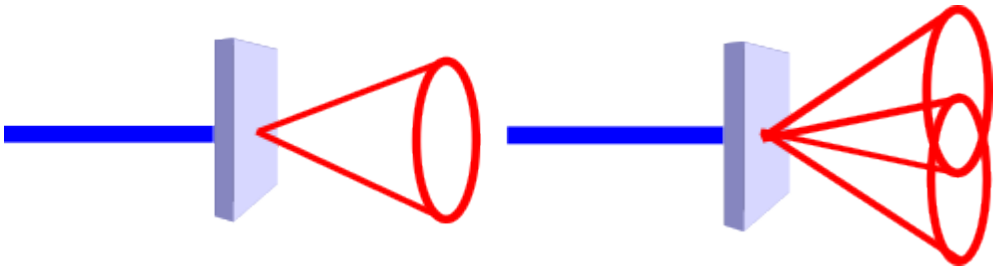

Figure 1.11: SPDC in non-linear crystal. Type 0 and Type I SPDC cone constraint is shown on the left. Type II SPDC is shown on the right

.

SPDC can be categorized into three varieties all characterized by the polarization relationship between the pump photon and the down-converted photons. Type-II SPDC is the most often used form of two-photon entanglement [91], the defining characteristic is that the produced signal and idler photons have perpendicular polarizations. Type-I SPDC is characterized by the signal and idler photons having the same polarization but orthogonal to the pump photon polarization. Type-0 SPDC is described by all the photons sharing the same polarization. A summarized explanation of the theory and derivation of SPDC is given in the work by Catalano [92]. An important feature of SPDC is that due to the conservation of momentum the down-converted photons are constrained to be emitted in cones that are symmetric around the pump beam. Figure (1.11) represents Type-II and Type-I SPDC where the output photons are constrained to one of two respective cones. Type-0 SPDC is similar to Type I in that there is a single emission cone.

1.6 Thesis Work

My PhD research has been focused exploring these key concepts to probe quantum optical phenomena and better our understanding of the quantum realm. In the following section I will introduce my efforts to explore various quantum optic effects. Beginning with an attempt at quantifying the interaction between the

Doppler effect and entanglement. Followed by a brief study of entangled photon generation in non-linear fiber and various interference measurements. The majority of my research was dedicated to an experimental investigation and modeling of the scalar Aharnov-Bohm effect .

Chapter 2

Doppler Effect on Entanglement

Quantum entanglement has always been an obscure topic since its coining in 1935 [93]. Many scientists have dedicated their life long research efforts into understanding entanglement and its many interesting effects on the quantum realm. Not only have these efforts led to a better understanding of quantum mechanics but they have led to an explosion of technological advances utilizing the characteristics of quantum phenomena. Quantum information processing, quantum transport, quantum encryption all are great examples of current quantum entanglement research areas [86]. However, despite all the advances in our understanding of quantum mechanics there always seems to be questions that have yet to be answered. One seemingly unexplored avenue for quantum entanglement is if Doppler shift alters the properties of entangled photon pairs in a measurable or useful way. This section of the manuscript seeks to explore this avenue of research and establish methods that can be used to quantify the effect of Doppler shift on entanglement.

2.1 Doppler Effect

The Doppler Effect is an interesting physical phenomenon that has many implications throughout the study of physics [94–96]. Simply put, it is the effective frequency change of a wave due to the relative motion between an observer and a wave source. It was first described by the Austrian physicist Christian Doppler in 1842 [97]. The most easily observable example of this effect is the change of pitch

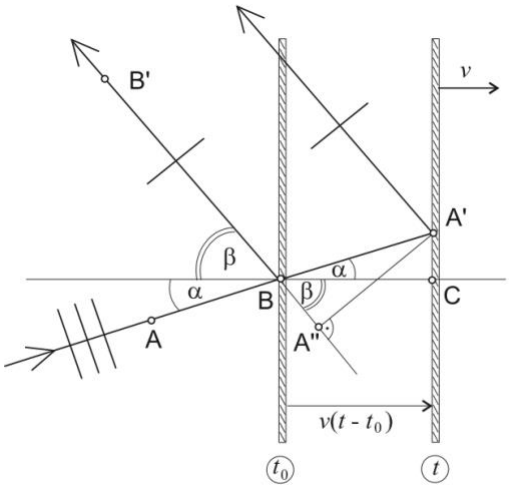

Figure 2.1: Moving plane mirror with incedent light producing a Doppler shift in the reflected light

heard when a nearby car is passing by while honking its horn. While the car is heading towards you the successive wavefronts are emitted closer and closer to the observer, therefore they take less time to arrive causing there to be a perceived upshift in emission frequency of the sound. The inverse is true for the car moving away, the waves then seem to be emitted farther apart in time and yield a downshift in frequency. This phenomenon also applies to light propagation as sources of light also have the ability to be moving relative to an observer. Though what we referred to as an upshift in frequency, for sound, is often referred to as blue shift for light. Similarly, for the downshift we refer to it as a redshift. This is due the perceived light being shifted either in the blue or red direction with respect to the spectrum of light [98]. However, there is a distinct difference between the Doppler Effect for a wave propagating in a medium, such as sound, and one that does not require a medium, such as light. For waves traveling through a medium the total Doppler Effect arises from the motion of the source, motion of the observer, and motion of the medium. For sound all of these effects need to be accounted for individually. However, for light waves no medium is required for propagation so the only thing to consider is the relative motion between the observer and emitter. For the purpose of observing a Doppler shift in an optical lab setting, we will be focus-

ing on the Doppler shift of light as it is reflected off of a moving surface. Following the derivations of Gjurchinovki [99], we can obtain the dynamics of Doppler shift of light reflected off of a uniformly moving mirror. Normally one would take the approach described by Einstein in his discussion of special relativity; However, this approach requires the utilization of Lorentz transformations which can be cumbersome [100]. We can take an easier approach that uses basic knowledge of wave optics along with the constant speed of light postulate. Starting with figure (2.1) we can assume a plane-polarized light wave is incident on a vertical plane mirror that is moving at a constant velocity v to the right. With this, α represents the angle of incidence and β represents the angle of reflection. A and B are the points of two consecutive wavefronts, the distance between the two points is set equal to the wavelength of the light $\overline{AB} = \lambda_0$. It is obvious that the wavefront at B will arrive sooner to the mirror than that of point A, so we will denote the arrival time as t_0 and t respectively. This difference in arrival time is due to the longer path that the wavefront at A will have to travel, $\overline{AA'} = c(t - t_0)$. This larger path difference is attributed to the distance that the mirror will travel to the right from its original position at $t0$, $x(t - t_0)$. While the wavefront at A is traveling to $A\prime$, the wavefront at B will travel the reflected path to $B\prime$, $\overline{BB'} = c(t - t_0)$. One can observe that the paths of the reflected wavefronts will not coincide and that the shortest distance between the planes of reflected wavefronts is equal to the new wavelength of the reflected light, $\overline{A''B' = \lambda}$. According to the geometry of figure (2.1 we have the two relations:

$$\overline{AA'} = \overline{AB} + \overline{BA'} \tag{2.1}$$

$$\overline{A''B'} = \overline{A''B} + \overline{BB'} \tag{2.2}$$

Using the formed triangles from $A^{'}BC$ and $A^{'}AB$ we can obtain:

$$\overline{BA'} = \frac{v(t - t_0)}{\cos\alpha} \tag{2.3}$$

$$\overline{A''B} = v(t - t_0)\frac{\cos(\alpha + \beta)}{\cos\alpha} \tag{2.4}$$

We can rewrite equations (2.1-2.2) as:

$$c(t - t_0) = \lambda_0 + \frac{v(t - t_0)}{\cos\alpha} \tag{2.5}$$

$$\lambda = v(t - t_0)\frac{\cos(\alpha + \beta)}{\cos\alpha} + c(t - t_0) \tag{2.6}$$

Rewriting the term $(t - t_0)$ using (2.5) as:

$$t - t_0 = \frac{\lambda_0}{c - \frac{v}{\cos\alpha}} \tag{2.7}$$

By substituting (2.7) into (2.6) we arrive at:

$$\frac{\lambda}{\lambda_0} = \frac{c + v\frac{\cos(\alpha+\beta)}{\cos\alpha}}{c - \frac{v}{\cos\alpha}} \tag{2.8}$$

By utilizing the following trigonometric identities we can replace the angle of reflection:

$$\cos(\alpha + \beta) = \cos\alpha\cos\beta - \sin\alpha\sin\beta \tag{2.9}$$

$$\sin\beta = \sqrt{1 - \cos^2\beta} \tag{2.10}$$

$$\cos\beta = \frac{-2\frac{v}{c} + (1 + \frac{v^2}{c^2})\cos\alpha}{1 - 2\frac{v}{c}\cos\alpha + \frac{v^2}{c^2}} \tag{2.11}$$

Through some algebraic manipulation we can transform (2.8) into:

$$\frac{\lambda}{\lambda_0} = \frac{1 - \frac{v^2}{c^2}}{1 - 2\frac{v}{c}\cos\alpha + \frac{v^2}{c^2}} \tag{2.12}$$

Taking into account that $\lambda_0 = c/f_0$ and $\lambda = c/f$ equation (2.12) results in the same formulation given by Einstien through his use of Lorentz transformations [100].

$$f = f_0 \frac{1 - 2\frac{v}{c}\cos\alpha}{1 - \frac{v^2}{c^2}} \tag{2.13}$$

2.2 Entangled Photon Pair Generation

As eluded to previously Spontaneous Parametric Down Conversion (SPDC) is a commonly used optical process to generate entangled photon pairs with well defined characteristics [101]. For specific configurations of a SPDC generating non-linear crystal we can fine tune these characteristics [102]. For the purpose of exploring the Doppler effect's influence on entanglement one can utilize degenerate Type-0 SPDC. This configuration results in a photon pair that shares the same values of wavelength, frequency and polarization. Indistinguishable characteristics are desirable as they allow for higher order entanglement between the photon pairs [103].This indistinguishabilty also allows for other interesting quantum effects such as the Hong–Ou–Mandel effect, which will be delved into later in this work [104]. Now that we have a grasp on the desirable characteristics of our initial entangled photon pairs, we can explore how we can efficiently generate these pairs.

In a $\chi^{(2)}$ non-linear medium, non-linear crystal, pump photons interact with the quantum vacuum to cause down-conversion resulting in a photon pair, a signal and idler photon. This process, SPDC, is well understood and can be verified through first principles. One important concept to this work is the efficiency of the entangled photon generation through type-0 SPDC, as one needs a reliable and consistent source of entangled photons in order to make definitive quantum measurements. The expected number of photon pairs can be quantified through the calculation of the biphoton generation rate for a given set of parameters. The

single-mode rate for degenerate type-0 and type-1 SPDC can be represented by the following equation [105]:

$$R_{sm}^{t1/t2} = \sqrt{\frac{2}{\pi^3}} \frac{2}{3\epsilon_0 c^3} \frac{n_{g1} n_{g2}}{n_1^2 n_2^2 n_p} \frac{d_{eff}^2 \omega_p^2}{\sqrt{\kappa}} \left| \frac{\sigma_p^2}{\sigma_1^2 + 2\sigma_p^2} \right|^2 \frac{P}{\sigma_p^2} L_z^{3/2} \tag{2.14}$$

This equation is derived from base principles assuming a constant $\chi^{(2)}$ medium of length L_z and a collimated pump beam. For this work we will be focusing on the use of a periodically poled Potassium Titanyl Phosphate (ppKTP) crystal as the non-linear medium. Some of the advantages of using ppKTP stem from its ability to generate photon pairs at room temperature and low optical pumping power on the order of 5mW [106]. Since the crystal is periodically poled, the value of $\chi^{(2)}$ varies back and forth between two set values throughout the crystal. This is similar to layering multiple crystals in a pattern of alternating $\chi^{(2)}$ values, shown in Fig 2.2. The following equation represents the photon rate of a periodically poled medium, where n represents the order of quasi-phase matching:

$$R_{sm}^{PP(n)} = \frac{4}{n^2 \pi^2} R_{sm} \tag{2.15}$$

$$z_R = \frac{\pi \omega_0^2}{\lambda} \tag{2.16}$$

To maximize the generation rate of photon pairs, it is common practice to focus the pump beam down to the smallest beam waist possible within the crystal [107]. While doing so one must also make sure the depth of focus or Rayleigh length matches that of the optical media. For Gaussian beams, such as the pump laser, the Rayleigh length is defined by Eq 2.16 and describes the distance from the minimum beam waist of a focused beam to the propagation distance at which the beam waist is increased by a factor of $\sqrt{2}$ [108]. With-in this length the beam is considered well focus and will maximize the generation rate of photon pairs. Utilizing Eq 2.14 and Eq 2.15 and assuming first order quasi-phase matching we can estimate a lower bound generation rate for Type-0 SPDC in our specific ppKTP

crystal, with a generation rate of $1.98 * 10^7$ pairs per second. This lower bound is in agreement with other experiments that produce entangled photon pairs via type-0 SPDC in ppKTP on the order of $10^6 \frac{Hz}{mW}$ [109, 110]

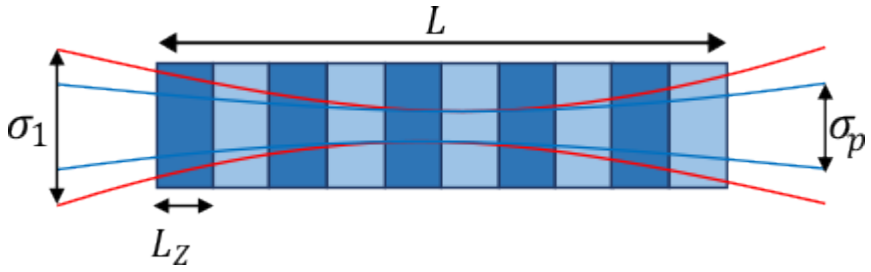

Figure 2.2: Type-0 SPDC in Periodically Poled Potassium Titanyl Phosphate (ppKTP) Pumped by a focused CW laser with σ_p beam waist producing a degenerate photon pair beam with beam waste σ_1. The crystal itself has a width of 2mm, height of 1mm and a length of 30mm, with poling period $L_z = 3.245\mu m$.

2.3 Entangled Photon Apparatus

Our ideal experimental source setup consists of a non-linear crystal such as the periodically-poled potassium titanyl phosphate (ppKTP), set in a Sagnac interferometer pumped by a constant wavelength (CW) 405nm laser. A similar source as been used in the work by M.V. Jabir and G.K. Samanta where they have shown one can produce degenerate photon pairs at room temperature with high spectral brightness using a similar scheme [106]. Figure (2.3) contains the basic optical setup for the entangled photon source where a ppKTP crystal is centered in a polarization Sagnac interferometer. The Sagnac interferometer consists of a dual wavelength polarizing beam splitter (DPBS) and two dual wavelength mirrors (M1,M2), reflective (R¿.90) at both 405nm and 810nm. The ppKTP crystal is symmetrically placed in the interferometer with respect to the output ports of the DPBS.

The optical source can be described as follows : a pump laser at 405nm CW is incident on a 405nm half-wave plate (HWP1) then passes through a dichroic mirror (DM), transmissive at 405nm and reflective at 810nm, and is finally directed into

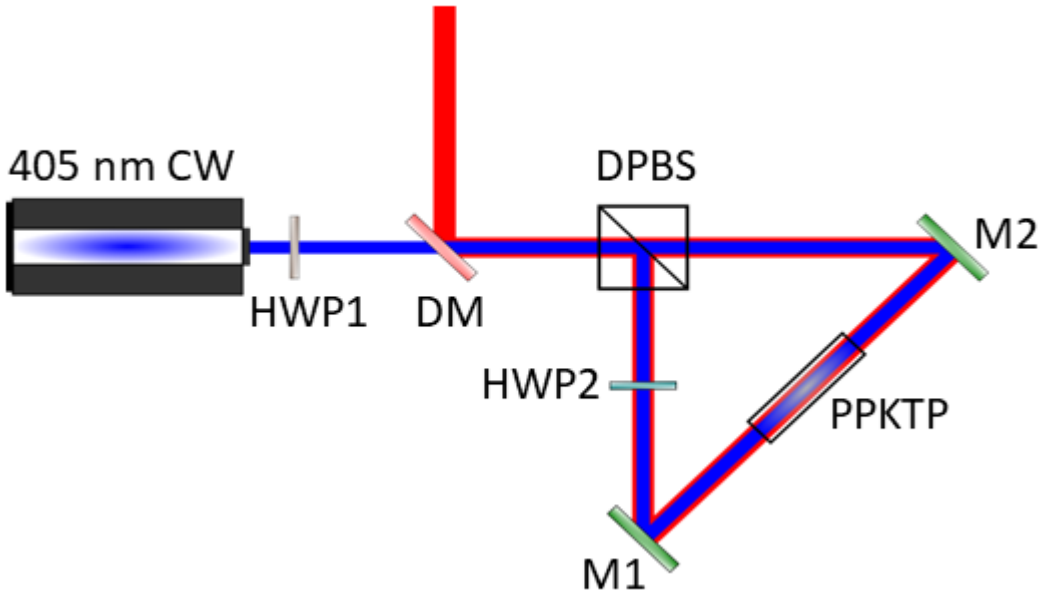

Figure 2.3: Degenerate entangled photon source pumped and 405nm, emitting indistinguishable signal and idler photons at 810nm. Based on placing a ppKTP non-linear crystal symmetrically in a Sagnac interferometer. Basic optics can be used to minimize beam waist to improve generation rate.

a Sagnac interferometer through a dual wavelength polarizing beam splitter. The pump beam has its polarization altered such that the power at the transmitted (vertically polarized) and reflected (horizontally polarized) ports of the DPBS are balanced. The vertically and horizontally polarized photons travel clockwise and counter clock wise respectively through the Sagnac interferometer. The clockwise traveling, vertically polarized, beam produces vertically polarized Type-0 SPDC photons at 810nm. The CCW travelling, horizontally polarized, beam produces horizontally polarized Type-0 SPDC photons at 810nm. There is a dual wavelength half-wave plate (HWP2) placed in one of the arms of the interferometer so that the vertically polarized beam is transformed into a horizontally polarized one and vice versa. This allows for both the clockwise and CCW traveling pump and SPDC photon beams to be collected as they all exit the same port of the DPBS. These two beams are then separated by a dichroic mirror as it reflects the SPDC produced

810nm beam and transmits the 405nm pump beam.

2.3.1 Source Characterization

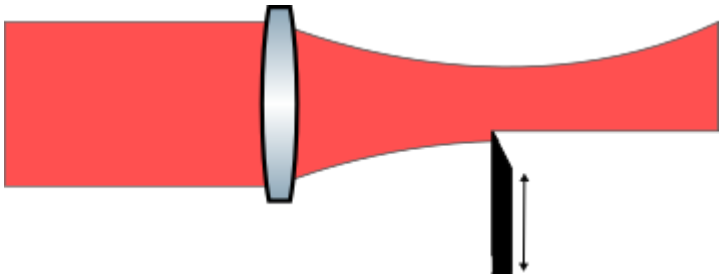

Figure 2.4: Knife edge measurement of a focused Gaussian beam in order to find its beam waist. By translating a fine tipped edge across the beam diameter and measuring the beam power. The positions at which the beam power drops by a factor of $\frac{1}{e^2}$ define the beam waist.

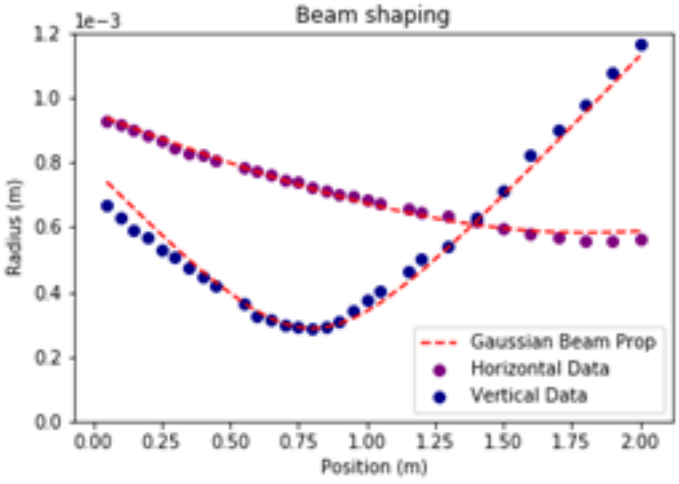

Figure 2.5: Gaussian beam propagation measurements use knife edge technique to determine beam waist as a function of distance from focusing lens.

Utilizing Gaussian beam propagation we can calculate the minimum beam waist we can achieve within the ppKTP crystal [3].By optimizing the parameters in (2.14) we can obtain the correct optics choices to minimize the beam waste. By minimizing the pump beam waist and focusing the beam into the crystal we can

expect a larger generation rate than that of a non-focused beam [107]. Preliminary results showed a beam waist value of $2500\mu m$. The minimum beam waist was determined by performing 'knife edge' measurements, shown in figure (2.4) , to find the beam radius as a function of propagation distance from the focusing lens. The method to perform these measurements consisted of using a very thin edge, similar to that of a knife, to partially block the beam and measure its optical power as the edge is transitioned across the beam's cross sectional diameter. For a Guassian beam, the points at which the optical power is depleted, from the maximum unblocked beam, by a factor $\frac{1}{e^2}$ are used to determine the beam waist. Referring to figure (2.5) the point at which the vertical and horizontal beam waists cross is the point at which beam is perfectly circular and the total beam waist is minimized. The results depict a beam waste of $600\mu m$ for this specific measurement and optical setup, which is satisfactory as it is smaller than the crystal width of 1mm. With further adjustments to optical components we have achieved beam waists of $70\mu m$ which has resulted in a larger generation rate than the original calculated value.

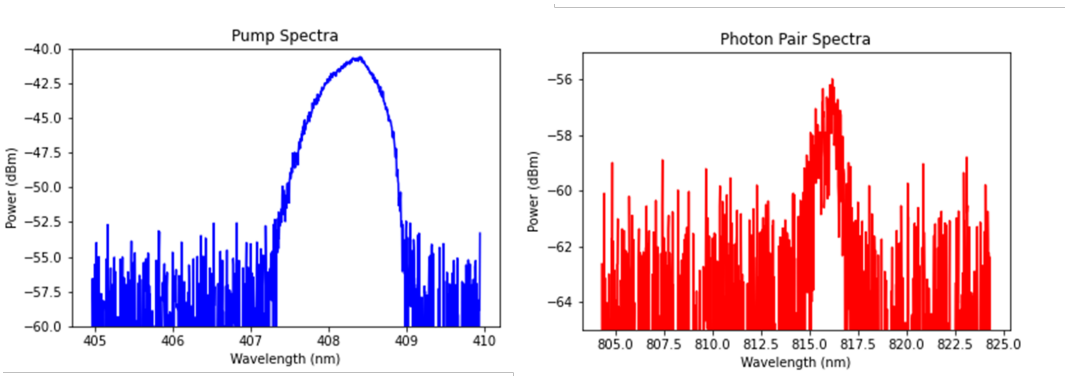

Figure 2.6: Source and Pump spectra from SPDC Type-0 in ppKTP. Pump beam spectra displayed on the left and photon pairs displayed on the right.

To characterize our source we have previously calculated the expected pair generation rate of $1.98 * 10^7$ pairs per second. This rate leads to an estimated production efficiency of $9.74 * 10^{-8}$. This generation rate is only a lower bound and is promising as it is large enough to be detected by both single photon count-

ing modules and optical spectrum analyzers [111]. Some preliminary results have achieved detection rates of $\approx 1.0 * 10^{10}$ with pump power $\approx 100mW$ leading to an efficiency of production of $\approx 4.9 * 10^{-5}$. These results are an order of magnitude larger than previous measurements of SPDC in ppKTP [106, 109, 110]. We calculate the approximate generation rate based on the optical power of the detected 816nm beam shown in figure (2.6), this yields a lower bound as the detections were measured by coupling the output of one side of the crystal to a fiber and into an OSA. This means that due to an innate low coupling efficiency into the fiber one can expect higher actual generation rates.

2.3.2 Measuring Important Probe Quantities

While generation of the entangled photon pairs is an important pillar of this work, detection of these pairs and measuring their characteristics is even more important. With the pair production scheme out of the way we move on to probing the effect Doppler shift has on the entanglement between pairs and in order to do this we must be able to detect and quantify any observable changes. There are two important quantities to consider in probing the effects,one is time delay between the signal and idler Δt, as well as the Doppler shift itself $\Delta\omega_s$. The measurement of Δt allows for us to determine relative position of the reflective object producing the Doppler shift and the measurement of $\Delta\omega_s$ allows for quantification of its relative velocity, through the use of equation (2.13).

Measuring the time delay between the signal and idler photons is the more difficult task of the two. Since detecting single photons is innately difficult one adds another layer of difficulty when making sure they are measuring the correct signal and idler photons. One way to circumvent this is by measuring the correlation between the signal and idler photons upon arrival at two different single photon counters. This measurement would probe the degree of second-order coherence or otherwise known as the second order correlation function $g^{(2)}(\tau)$,equation (2.17), Essentially it is a measurement of intensity fluctuations between two paths with respect to time, which when measured by photon detectors is proportional to the photon count [3].

$$g^{(2)}(\tau) = \frac{\langle I(t)I(t+\tau)\rangle}{\langle I(t)\rangle \langle I(t+\tau)\rangle} = \frac{\langle n_i(t)n_s(t+\tau)\rangle}{\langle n_i(t)\rangle \langle n_s(t+\tau)\rangle} \tag{2.17}$$

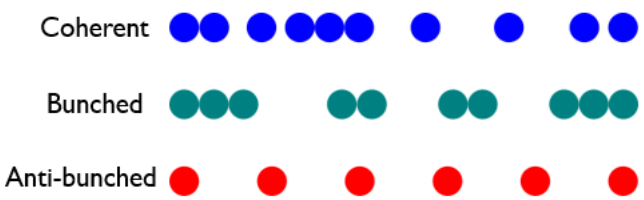

Figure 2.7: Emitted photon grouping in time. Coherent light such as a laser displays random gaps of time between photons. Bunched light is chaotic, such as that emitted from a spectral lamp, meaning photons are emitted in bursts resulting in grouping. Anti-bunched light is strictly a quantum phenomena and is seen as a consistent time gap between all emitted photons.

The second order correlation function also allows us to classify the grouping of individual photons with respect to other photons in time [3]. The classifications are as follows: coherent, bunched and anti-bunched. Coherent light has random gaps of time between emitted photons. Bunched light is classified by photons clumping together in bunches. Anti-bunched light is when the time interval between photons is regular and non-random. Each of these cases can be separated by the values of the second order correlation function. For all classical sources of light, coherent and bunched, we know $g^{(2)}(\tau) \geq 1$ and $g^{(2)}(0) \geq g^{(2)}(\tau)$.In comparison non-classical or anti-bunched light results in $g^{(2)}(0) < g^{(2)}(\tau)$ and $g^{(2)}(0) < 1$. As a result of the incurred time delay from a round trip we anticipate that the time spacing between signal and idler arrival will have little variation. Due to this we can measure the arrival times of the signal and idler photons to determine a total trip time. By varying the time delay to find a value in which $g^{(2)}(\tau)$ is maximized, this would indicate that we have a maximum number of photons arriving simultaneously at both detectors. Which is what one would observe if there was no net time delay and thus the signal and idler photons would be traveling the same distance.

The measurement of the frequency shift of light $\Delta\omega_s$ due to the Doppler effect is much simpler and a diagram of a simple measurement scheme is depicted in figure (2.8).Since our photon source is degenerate we can directly measure the signal

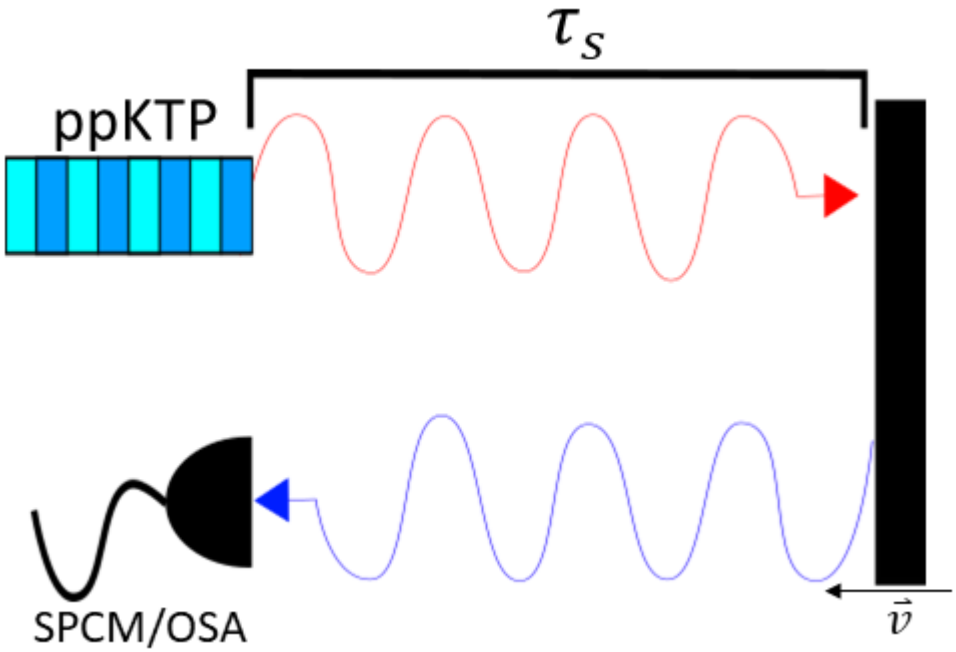

Figure 2.8: A simple measurement of Doppler shifted entangled photon pairs. Where the signal photon is shifted by a moving reflective surface with velocity $\vec{v}$ and measured by an optical spectrum analyzer and compared to its expected original frequecy.

photon's frequency after it has been Doppler shifted to find the frequency shift. This can be accomplished by simply measuring the wavelength of the signal photon stream in an optical spectrum analyzer (OSA) or some other type of optical frequency measuring device. This scheme requires multiple measurements to define the effects Doppler shift has on entangled photon pairs, However there are theoretical schemes that could do these measurements with single photon pairs [112].

2.4 Null-Results and Possible Paths Forward

Despite achieving an adequate entangled photon source, this work hit a dead end in terms of exploring the Doppler effect, due to lack of resources. As a result my PhD work continued on to exploring other interesting quantum phenomena. Through this experience I am able to utilize various optical techniques to probe

quantum phenomena and have laid out the groundwork for any effort to continue probing the Doppler effect on entanglement using a ppKTP degenerate entangled photon source. As a proof of applicability I will present two avenues of possible experimental exploration and their applications. The first is inspired by theoretical work done by Lariontsev EG [113]. In his work Lariontsev derives an interesting result when a entangled photon pair is Doppler shifted by an acousto-optic modulator. The second is the improvement of current light detection and ranging (LiDAR) measurements by utilizing entangled photons as the light source.

2.4.1 Quantum Interference of Entangled Photon Pairs

An interesting phenomenon shows up in the derivation off a frequency shift due to an AOM acting on an entangled photon pair. Referring to Lariontsev's theroy we arrive at an expression for a bi-photon's amplitude after interacting with an AOM:

$$B(t, z_0) = F(\tau) \exp\left(-i[(\omega_p - 2\Omega)t - \phi_p(z_0) - \phi_0]\right) \tag{2.18}$$

Where Ω is the frequency of the sound wave in the AOM. It is apparent that the frequency shift of the bi-photon is twice the frequency of the acoustic wave. However this is not what we see classically for a single non-entangled photon, where one would normally see a frequency shift directly equal to Ω [27].Despite this being apparent in the derivation it is difficult to measure as normal measurements of light are based on coincident rates of photons,R_c, which is directly proportional to the square of the amplitude,$B(t, z_0)^2$, of the incident beam. This results in an independence of the carrier frequency and ultimately removes any trace of this effect due to time averaging and can be seen in equation (2.19). We can restore visibility of this effect by making an interference measurement which is phase sensitive.

$$R_c = |B(t, z_0)|^2 = F(\tau)^2 \tag{2.19}$$

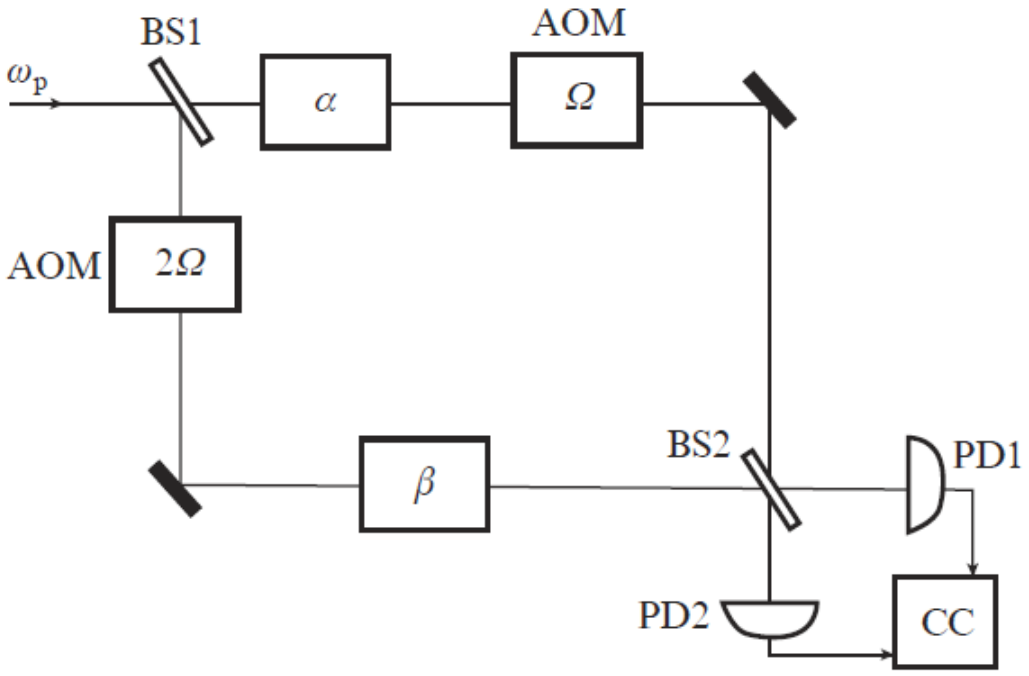

Figure 2.9: Interference measurement of dual AOM and NL crystal configured in a Mach-Zander interferometer, proposed by Lariontsev. In the primary arm a NL crystal generates bi-photons which are shifted by a AOM set to Ω. A secondary AOM set to a frequency shift of 2Ω is placed in one arm of the interferometer followed by another NL crystal which generates bi-photons. The two arms then interfere on a beam splitter and coincidence rates are measured at the outputs

By adding an additional AOM we can observe interference of bi-photons generated by two independent non-linear crystals. This is a simple and well understood phenomena and is sensitive to the phase of the pump beam applied to each crystal [114]. When set in a Mach-Zander interferometer configuration, displayed in figure (2.9), we can write the coincident rate as:

$$R_c = F_\alpha(\tau)^2 + |F_\beta(\tau)|^2 - 2Re(F_\alpha(\tau)F^*_\beta(\tau)) \exp i(\phi_\alpha - \phi_\beta + \phi_{0\alpha} - 2\Omega) \qquad (2.20)$$

In equation (2.20) α and β represent the independent non-linear crystals. Due to the interference of the two different sets of bi-photons the rate of coincidence is no longer carrier frequency independent and as a result the 2Ω shift is observable in R_c. This effect has yet to be proven experimentally and leaves an opportunity

to parse the Doppler effect on entanglement. If one can experimentally implement this theory it can be utilized as a form of two party communication encryption. Where one party sets the frequency of the main arm and the secondary party needs to know this frequency in order for the effect to be observed at the output.

2.4.2 Entanglement Enhanced LiDAR

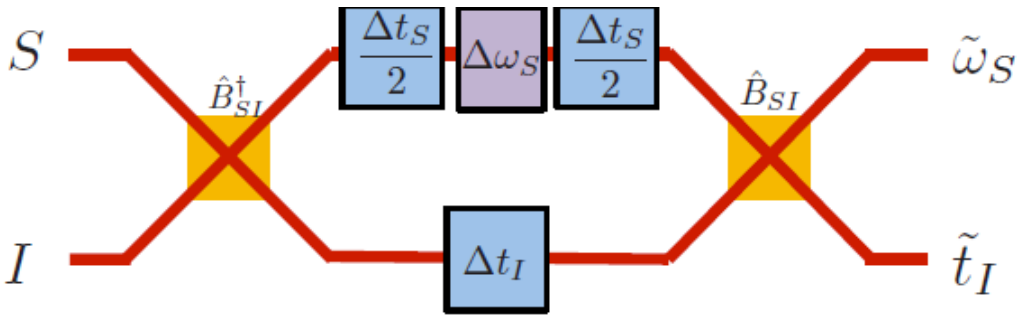

Figure 2.10: Diagram of entanglement enhanced LiDAR. Signal and Idler photons are operated on by a non-linear operator. The signal photon then is sent to be reflected of a moving object incurring a Doppler shift and a propagation time Δt_s. The idler photon is kept and only incurs a propagation time of Δt_I. The photon are then collected and operated on by the conjugate of the original operator allowing for a measurement of relative position and velocity of an object of interest.

Entanglement enhanced LIDAR technology is a possible outcome of Doppler shifted entangled photon pairs. Resulting in a form of quantum metrology technology with advantages to current LIDAR methods and technology. A few advantages can be found in the effectiveness of quantum entanglement as a encrypted measurement tool, efficiency of measurements and the time resolution of quantum measurements. As a result of entanglement any information gained by detection one photon of an entangled photon pair is useless without information about the other photon or the emission conditions. Allowing for a one way measurement that is secure from any secondary observer, leading itself to applications in fields where covertness is a requirement.

Work done by Zhuang et al. proposes a theoretical setup that will enable single photon pair signal-return LIDAR [112,115]. In normal LIDAR measurements

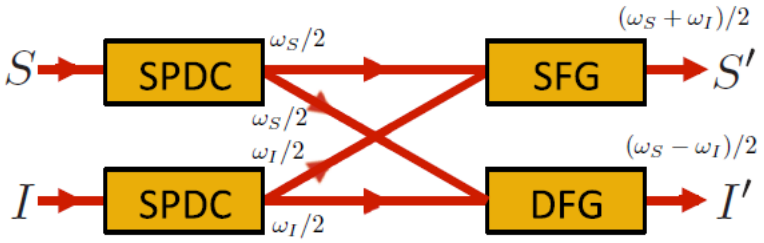

Figure 2.11: Physical interpretation of $\hat{\beta}_{SI}$ through a combination of multiple optical processes in different non-linear crystals. Sum Frequency Generation (SFG) converts two photon into another photon with a frequency equal to the sum of the two input photon frequencies. Difference Frequency Generation (DFG) takes two photons and converts them to a single photon with a frequency equal to the difference of the original two.

multiple photons are sent to a moving object and are Doppler shifted due to the relative velocity between the object and the receiver. These multiple photons are then detected on their return to yield a measurement of both distance and velocity of an object of interest. These measurements pertain to the total time of travel and the frequency shift imparted on the photons. Traditionally multiple measurements are needed to accurately determine these quantities meaning a large number of photons must be used. Zhuang's scheme utilizes entangled photon pairs to get simultaneous measurements of both velocity and distance. The scheme is visualized in figure (2.10). The signal and idler are prepared by a conjugate operator $\hat{\beta}^{\dagger}{}_{SI}$, physically represented by a combination of non-linear crystals. The non-linear crystals will perform the common optical processes of sum frequency generation (SFG), difference frequency generation (DFG) and SPDC. The signal is then sent to probe the object, accruing a frequency shift of $\Delta\omega_s$ and a time delay of Δt_S while the idler is retained for time Δt_I. The signal and idler are then operated on by $\hat{\beta}_{SI}$ allowing for the measurement of $\tilde{t}_I$ and $\tilde{\omega}_s$. By physically interpreting the $\hat{\beta}_{SI}$ operator with non-linear crystals one can improve the efficiency of normal LiDAR by orders of magnitude.

Chapter 3

Effects of Interference on Entangled Photon Pairs

In an effort to continue exploring interesting quantum optical effects on entangled photon pairs the next experimental work revolves around entanglement generation via non-linear optical fiber. Specifically four wave mixing in a $\chi^{(3)}$ non-linear fiber [116]. Utilizing this source of entanglement to probe interference measurements, such as the Hong–Ou–Mandel (HOM) effect. Similar to the previous work the experimental results were limited to preliminary findings and the groundwork being laid for future exploration. This section will present an entangled photon scheme in which interference effects such as , the HOM effect, time-delay and two-photon absorption can be probed.

3.1 Optical Kerr Effect

The base source of entangled photon pairs consisted of an optical fiber with a χ^3 non-linearity. The non-linearity leads to optical effects such has sum frequency generation, difference frequency generation and ultimately four-wave mixing (FWM) [117, 118]. FWM and many other non-linear optical effect originate from the Kerr effect, in which the presence of an electric field changes the index of refraction of a given material. For the optical Kerr effect the electric field is supplied by a beam of light which can be represented by equation (3.1).The ef-

fect itself can be characterized by the electric polarization,$\vec{P}$ of the given material equation (3.2).

$$\vec{E} = E_\omega \cos \omega t \tag{3.1}$$

$$\vec{P} = \epsilon_0 \left(\chi^{(1)} + \frac{3}{4} \chi^{(3)} \left| E_\omega \right|^2 \right) E_\omega \cos \left(\omega t \right) \tag{3.2}$$

Where χ represents the electric susceptibility and ϵ_0 is the vacuum permittivity. From (3.4) we can see that the index of refraction is dependent on the overall electric susceptibility of the material.

$$n^2 = \frac{\epsilon}{\epsilon_0} = 1 + \chi \tag{3.3}$$

$$n = \sqrt{1 + \chi} \tag{3.4}$$

In the case where a material has a non-linear electric susceptibility, the over all χ can be expressed as a combination of the linear and non-linear terms, in the case of a $\chi^(3)$ material we can express χ as (3.5):

$$\chi = \chi_L + \chi_{NL} = \chi^{(1)} + \frac{3}{4} \chi^{(3)} \left| E_\omega \right|^2 \tag{3.5}$$

By applying (3.5) to (3.4) we get an expression for the index of refraction in a $\chi^{(3)}$ material:

$$n = (1 + \chi_L + \chi_{NL})^{1/2} = (1 + \chi^{(1)} + \frac{3}{4} \chi^{(3)} |E_\omega|^2)^{1/2} \approx n_0 (1 + \frac{1}{2 n_0} \chi_{NL}) \tag{3.6}$$

Where $n_0 = \sqrt{1 + \chi_L}$ is the linear refractive index, applying a Taylor expansion, as $\chi_{NL} << n_0$, results in equation (3.6) and knowing $|E_\omega|^2 = I$ we end up with an expression for n that is intensity dependent.

$$n(I) = n_0 + \frac{3}{8n_0}\chi^{(3)}|E_\omega|^2 = n_0 + n_2 I \tag{3.7}$$

$$n_2 = \frac{3}{8n_0}\chi^{(3)} \tag{3.8}$$

n_2 is the second order non-linear refractive index and is often a very small value for most materials requiring large beam intensities such as lasers to have any measurable change to the refractive index [119]. The effect in non-linear optical fibers presents itself through self-phase modulation (SPM) which causes a short pulsed beam to incur a phase and frequency shift as it propagates through the fiber [120]. For pulsed a Gaussian beam with constant phase we can describe its intensity as a function of time with equation (3.9), where I_0 is the beams peak intensity and τ is half of the pulse duration:

$$I(t) = I_0 \exp\left(\frac{-t^2}{\tau^2}\right) \tag{3.9}$$

As the pulsed beam propagates through the fiber a time-varying refractive index is produced:

$$\frac{dn(I)}{dt} = \frac{d}{dt}(n_0 + n_2 I) = n_2 \frac{dI}{dt} = n_2 I_0 \frac{-2t}{2\tau} \exp\left(\frac{-t^2}{\tau^2}\right) \tag{3.10}$$

The time varying index of refraction results in a shift in the instantaneous phase due to the complex wavenumber's, $k = \frac{2\pi}{\lambda}n$, dependence on the index of refraction of a medium. This can be seen in equation (3.11) where ω_0 and λ are the original vacuum frequency and wavelength, L is the distance the pulsed beam has propagated in the medium.

$$\phi(t) = \omega_0 t - kz = \omega_0 t - \frac{2\pi}{\lambda_0} n(I) L \tag{3.11}$$

Due to the time varying phase shift, the instantaneous frequency of the pulse is shifted as well. Resulting from the instantaneous frequency dependence on the time variation of phase:

$$\omega(t) = \frac{d\phi(t)}{dt} = \omega_0 - \frac{2\pi L}{\lambda_0}\frac{dn(I)}{dt} \tag{3.12}$$

plugging in (3.10) results in a frequency shift dependent on beam intensity and time:

$$\omega(t) = \omega_0 + \frac{4\pi n_2 L I_0}{\lambda_0 \tau^2} t \exp\left(\frac{-t^2}{\tau^2}\right) \tag{3.13}$$

The effect is seen as a generation of additional frequencies, stemming from SPM, symmetrically around the fundamental pulse effectively broadening the spectrum due to dispersion. This can be seen when plotting equation (3.13), where the front of the pulse is downshifted in frequency and the end of the pulse is upshifted, shown in figure (3.1) For mediums with anomalous dispersion the reverse process can happen, resulting in a compression of the pulse in time [121]. For specific configurations of mediums and pulse intensity the two effects can be balanced resulting in a soliton, an optical pulse which does not change shape as it propagates [122]. As a result of the additional generated frequencies and phase shifts sometimes phase matched conditions are met allowing for four-wave mixing to occur [116].

3.2 Pair Generation via FWM in $\chi^{(3)}$ Fiber

Four-wave mixing can occur when multiple optical waves, with different optical frequencies, propagate in a non-linear medium together [123]. A simple case can be depicted when two optical beams of frequency ω_1 and ω_2 propagate in a $\chi^{(3)}$ fiber. The two beams induce an index of refraction modulation, due to the previously mentioned optical Kerr effect , centered at the difference between the two frequencies $\omega_2 - \omega_1$. This modulation creates a pair of frequencies symmetric about the center of the difference based on energy conservation, ω_3 and ω_4, represented in eqs...

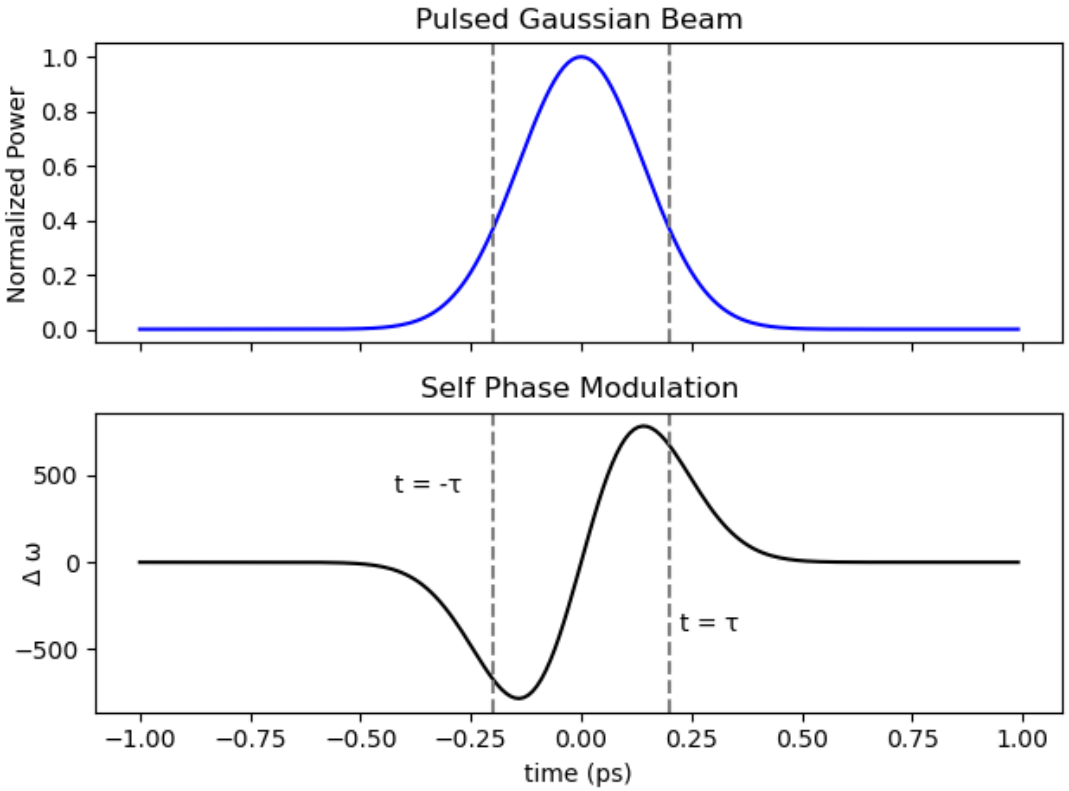

Figure 3.1: Self phase modulation of a pulsed Gaussian beam with $\tau = 10^{-12}s$. The front of the beam is being down shifted in frequency and the back of the beam is being upshifted in frequency. The realative shift is proportional to the peak intensity of the original beam.

$$\omega_3 = \omega_1 - (\omega_2 - \omega_1) = 2\omega_1 - \omega_2 \tag{3.14}$$

$$\omega_4 = \omega_2 + (\omega_2 - \omega_1) = 2\omega_2 - \omega_1 \tag{3.15}$$

If there already exists a propagating beam, at either generated frequency, amplification occurs known as parametric amplification [124]. The rate of generation of these pairs is fundamentally dependent on phase-matching conditions and optical intensity of the generating beams [125]. In order to obey phase-matching conditions all four wave vectors $\vec{k}$ must add to zero.

$$\vec{k}_1 + \vec{k}_2 + \vec{k}_3 + \vec{k}_4 = 0 \tag{3.16}$$

Injection angle, intensity and optical frequency of the pump beams must be taken into consideration as each can independently alter the relative wavevectors [126]. Due to the optical Kerr effect, high intensity beams will generate a multitude of shifted frequencies with varying wave numbers increasing the chance of phase matching. Phase matching can also be met by utilizing pump frequencies which are close to one another. Along with phase matching conditions FWM is effected by the polarization state of the beams involved, as the non-linear susceptibility itself is polarization sensitive [127].By optimizing beam intensity ,chromatic dispersion, polarization and alignment one can achieve optimal FWM generation of entangled photon pairs.

3.2.1 Characterization of Source

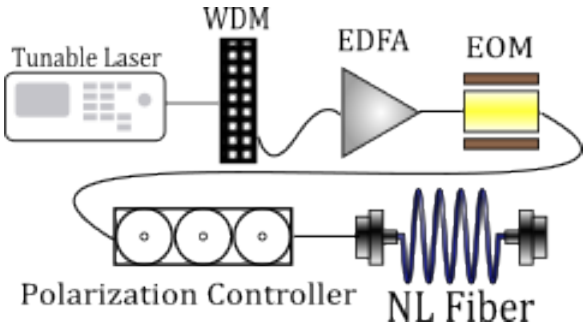

Figure 3.2: Four Wave Mixing source. A 1550 nm tunable laser pumps $\chi^{(3)}$ non-linear fiber to achieve FWM and generate entangled photon pairs. The pump is filtered by a WDM amplified by a Erbium Doped Fiber Amplifier (EDFA) and pulsed via EOM with the polarization controlled by fiber paddles.

For the purpose of creating fiber based entangled photon generation the experimental apparatus consisted of a low power, $100mW$, tunable constant wave length pump laser, filtered by a wavelength division multiplexer [128]. The low power beam was amplified by an Erbium CW fiber amplifier to around 5 Watts.

The amplified pump was then pulsed by an Electro-Optic Modulator (EOM) to achieve ns pulse widths. The polarization of the beam was controlled using manual polarization fiber paddles, which operate on the principle of stress induced birefringence [129].The pump beam was then launched into a 1m long $\chi^{(3)}$ nonlinear fiber for the purposed of inducing FWM and generating entangled photon pairs.

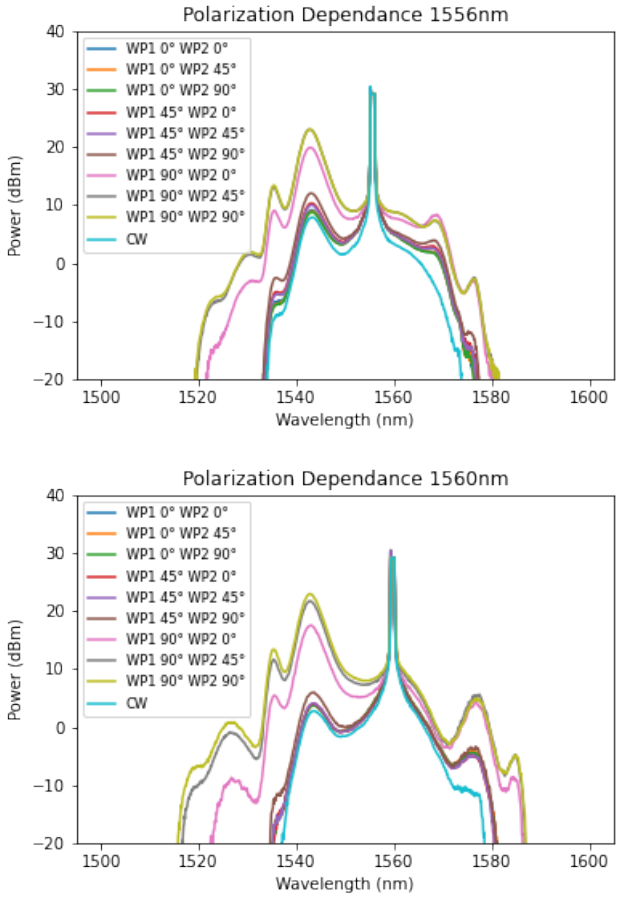

Figure 3.3: Four Wave Mixing in NL fiber at 1556nm and 1560nm. Polarization and peak intensity dependence is observed. With little difference between the two different wavelengths. The polarization was varied via fiber paddles being rotated a given amount. WP1 corresponds to a $\lambda/4$ waveplate and WP2 corresponds to $\lambda/2$ waveplate.

With relative low optical power, 1-2 W, we were able to observe FWM occur within the fiber. As previously mentioned the optical Kerr effect is polarization

dependent and as a result the FWM should be a function of pump polarization. Shown in figure (3.3) where the pulsed pump polarization was varied and compared to the output of the fiber when a CW unpulsed and unpolarized pump beam is launched into the fiber. Compared to the launching of the CW pump we can see the effect of both beam intensity and polarization on the FWM occurring in the fiber. Little significance can be seen in the difference between the two wavelengths of light launched into the fiber, however both establish the dependence on polarization and pump intensity. With the pump intensity being a factor on the efficiency of FWM the next step was to observe the direct effect of varying pump power. To do this one simply needs to increase the amplification of the pump beam. For our specific EDFA we could reach average optical powers of 5 W. While taking measurements at high power, ¿2W, the EDFA experienced fiber fusing due to high peak power and a faulty splice between the EOM and EDFA [130]. The result rendered the EDFA useless without a replacement fiber and as a result impeded the progress of this experiment; However, it also opened the door to exploration of the theory behind this project's purpose, allowing for one to lay the ground work such that progress can be made once the equipment is repaired. Here I will introduce the theory and proposed experiments for exploring the interference effects on photon pairs.

3.3 HOM Effect

The Hong-Ou-Mandel effect is a quantum interference phenomenon, in which two indistinguishable photons arrive at the same time to the two inputs of a beam splitter and exit the same output port, shown in figure (3.4) [104]. The HOM effect is strictly a quantum one and is not classically describable. Classically for a 50:50 beam splitter one would expect that regardless of the nature of the light the probability of detecting a photon at either exit would be equal, hence the 50:50 [131]. The common method of measuring this effect is by using a degenerate entangled photon source such as that of a FWM non-linear fiber or ppKTP crystal and guiding the signal and idler beams to the input ports of a 50:50 beam splitter.

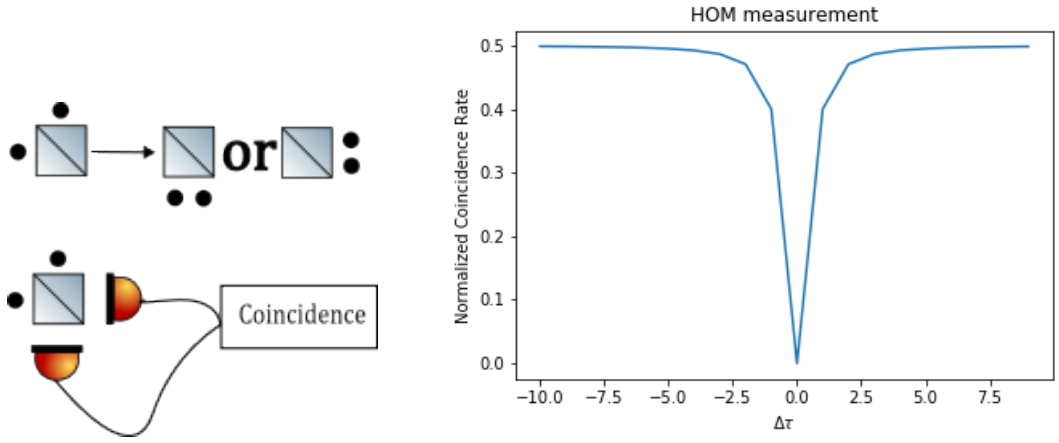

Figure 3.4: Example of the Hong-Ou-Mandel (HOM) effect shown in the top left portion of the figure and a simple measurement scheme shown underneath. Since the HOM effect results in both photons exiting the same port, the coincidence between two detectors should be minimized. This measurement will produce data similar to that of the graph on the right.

The output ports are then monitored by a photo-diode and a general coincidence measurement is made. The results will be a minimum at a point in which both arms of the paths are balanced in time and will be increased for all time delays. One can introduce a variable optical time delay in one of the arms and adjust it such that the minimum of coincidences is found, this will correspond to maximum value of indistinguishable photons arriving at the input ports of the beam splitter. This measurement will be similar to that in figure (3.4) While the HOM effect itself is an interesting phenomena, the time inverted HOM effect provides intriguing questions for time dependent measurements [132]. One possible experiment to probe the reverse HOM effect is looking at the complicated interference of two degenerate entangled photon pairs arriving at a beam splitter.

3.3.1 Reverse-HOM Effect

The HOM effect is time reversible ,which suggests that when a photon pair arrives at a single input of a beam splitter the pair will be separated with one photon at each output of the beam splitter, as shown in figure (3.5) [133]. An interesting situation arises when two indistinguishable photon pairs arrive at both

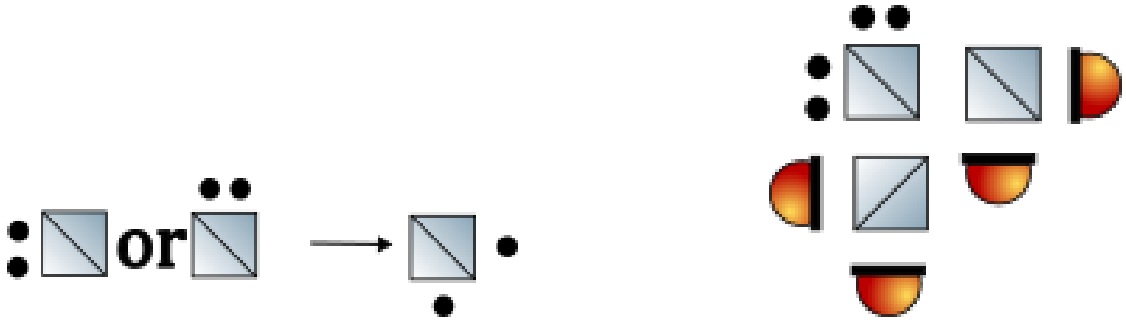

Figure 3.5: Example of the reverse Hong-Ou-Mandel (HOM) effect shown on the left. On the right is a simple measurement scheme to observe the reverse HOM effect on two indistinguishable photon pairs. The four photo-diodes are sensitive to two photon absorption and coincidence measurements can be made between them.

input ports of a beam splitter. To the best of our knowledge no work has been done to explore this scenario. For a simple characterization, one could utilize the normal HOM effect to prepare photon pairs at each input of a beam splitter and introduce a variable time delay in one of the input arms so that the arrival times could be tuned to maximize any HOM effects. A measurement similar to the previous HOM measurement can be made by using photo-detectors that are sensitive to two photon absorption and counting the rate of two photon absorption coincidences between the two ports. One can take another step to directly probe the reverse HOM effect on entanglement, a simple scheme is shown in figure (3.5). With an additional beam splitter cascaded at each output port of the original beam splitter the coincidences between four photo-detectors could be measured. In addition if each photo-detector is sensitive to two photon absorption any direct measurements of two photon absorption reveals that the indistinguishable characteristics of the photons were not maintained and thus the entanglement was destroyed. If coincidences can be maximized one can claim the indistinguishable characteristics were maintained and the HOM effect does not disturb the entanglement of photon pairs.

Chapter 4

Aharonov-Bohm Effect

While only preliminary data and proposed exploration of the HOM and Doppler effects on entanglement, were presented ,it is apparent that efforts into exploring quantum optical effects are promising. Especially those effects that originate from outside stimulation such as an electric field in the case of the Kerr effect and relative motion in the case of a Doppler shift. One such effect substantially explored in this PhD work was the Aharonov-Bohm (AB) effect and will be the main topic of this section.

4.1 Introduction to AB effect

The Aharonov-Bohm (AB) effect occurs due to a charged particle's connection to the electromagnetic potential A through the complex phase, $\varphi(A,t)$, of its wave-function, $\psi_i(r,t)$ [134]. The AB effect can be broken down into magnetic vector and electric scalar potential components. Previous work has been done to observe the magnetic vector effect and attempts have been made to observe the scalar effect however, they all fundamentally rely on observations of interference fringe shifts [135–137]. In this section we will detail our endeavors to spectroscopically detect the scalar Aharonov-Bohm (AB) effect in Rubidium, comparing our findings with theoretical spectra derived from the Nakayama model [138, 139]. To enhance the discernibility of spectral features, we leverage a N-type four-level system to achieve sub-natural linewidth resolution on the order of a few MHz [140]. Despite

these efforts, we have not yet observed the scalar AB effect in our data. With the leading rationale for the absence of observable confirmation being the rapid fall off in optical sideband power due to phase modulation and the dependence on the modulation depth parameter α. Accordingly, we proposed an experimental correction to address this optical sideband power fall off by introducing additional phase modulation and dispersive media. Through simulations we explored the optimal configurations resulting in desirable optical sideband power bandwidth.

4.2 AB Effect Derivation

Originally the vector and scalar potentials were introduced into electrodynamics to simplify the calculation of fields [141]. For the simplest of cases we can classically define the equations of motion with only the fields themselves . However, in quantum mechanics all knowledge of potentials and fields are required for any correct interpretation, exemplified by the AB effect. The classical Hamiltonian of a charged particle moving in a uniform electromagnetic field can be represented by equation (4.1) where we can see the dependence on both the vector potential $\mathbf{A}$ and scalar potential V.

$$\mathcal{H} = \frac{1}{2m}(\mathbf{p} - q\mathbf{A}(\mathbf{x}, t))^2 + qV(\mathbf{x}, t) \tag{4.1}$$

With the Hamiltonian we can formulate the Schrödinger equation as:

$$i\hbar\frac{\delta}{\delta t}\Psi = \mathcal{H}\Psi = \left[\frac{1}{2m}\left(-i\hbar\nabla - \frac{q}{c}\mathbf{A}(\mathbf{x}, t)\right)^2 + qV(\mathbf{x}, t)\right]\Psi \tag{4.2}$$

Due to gauge invariance the resulting wavefunction Ψ can be written as:

$$\psi_i = \Psi_i \exp\left(-\frac{i}{\hbar}E_i t - i\varphi(\mathbf{A}, V)\right) \tag{4.3}$$

Where any vector potential $\mathbf{A}$ and or scalar potential V adds an additional change in the complex phase $\varphi(\mathbf{A}, V)$. When there is an absence of fields but an existence of either a vector potential $\mathbf{A}$ or scalar potential V the charged particle experiences what is known as the AB effect [134].

4.2.1 Vector Potential Effect

In the case of a charged particle traveling in a region with a non-zero **A** but $\mathbf{E} = 0$,$\mathbf{B} = 0$ and $V = 0$ for all values of t we end up with a complex phase only dependent on the vector potential **A**.We classify this case as the magnetic vector AB effect and it has been studied experimentally by placing a solenoid between the slits of a double-slit experiment and observing the resulting interference pattern [137]. The complex phase difference between the two paths is given by:
The change in complex phase results in a splitting of energy levels determined by the magnetic flux of the area between the two paths:

4.2.2 Scalar Potential Effect

Another scenario for the AB effect occurs when a charged particle is in the absence of any field and vector potential but is subject to a time varying scalar potential $V(t)$.My work studies this case and experimentally produces these condition by place a charged particle in a Faraday cage supplied with a time varying potential, maintaining the criteria **B=0** and $\mathbf{E} = -\nabla V = 0$. The Hamiltonian in this case can simply be written as:

$$\mathcal{H} = \mathcal{H}_0 + qV(t) \tag{4.4}$$

The base Hamiltonian $\mathcal{H}_0$ is independent of time and solely depends on position of the charged particle. Whereas qV(t) is independent of position and only depends only on the particle's time spent in the varying potential. The Schrödinger equation for this system can easily be expressed by:

$$i\hbar\frac{\delta\psi}{\delta t} = \mathcal{H}\psi = (\mathcal{H}_0 + qV(t))\psi \tag{4.5}$$

Where $V(t) = V_0 \cos\omega t$ represents the applied time varying potential applied to the Faraday cage. We can apply separation of variables to find a representation for both the time dependent and position dependent equations. For the position

dependent equation, we arrive at the well-known time-independent Schrödinger equation:

$$\mathcal{H}_0\Psi_i(\mathbf{x}) = E_i\Psi_i(\mathbf{x}) \tag{4.6}$$

While integrating the time dependent equation results in a familiar exponential form:

$$T(t) = \exp\left(-\frac{i}{\hbar}E_i t - i\frac{qV_0}{\hbar\omega}\sin\omega t\right) = \exp\left(-\frac{i}{\hbar}E_i t - i\alpha\sin\omega t\right) \tag{4.7}$$

$$\alpha = \frac{qV_0}{\hbar\omega} \tag{4.8}$$

We define α as the phase modulation depth parameter and it determines the strength of effect due to the applied potential. Due the dependence on the applied potential's amplitude V_0 and frequency ω, α is limited by the realistic capabilities of whatever arbitrary signal generator is used. Utilizing Eq's 1.4 and 1.3 results in a the expected formulation of the wavefunction where the complex phase φ originates from the time varying potential $V(t)$:

$$\psi_i = \Psi_i(\mathbf{r})\exp\left(-\frac{i}{\hbar}E_i t - i\varphi(t)\right) \tag{4.9}$$

$$\varphi(t) = \alpha\sin\omega t \tag{4.10}$$

The complex phase of the wavefunction, $\varphi(t)$, can be exponentiated and using Jacobi-Anger expansion one arrives at a full and simplified expression for the wavefunction and the resulting energy levels:

$$\psi_i = \Psi_i(\mathbf{r})\sum_{n=-\infty}^{\infty}(-1)^n J_n(\alpha)\exp\left(-\frac{i(E_i - n\hbar\omega)t}{\hbar}\right) \tag{4.11}$$

$$E_i^{(n)} = E_i \pm n\hbar\omega \tag{4.12}$$

One can find that the resulting infinite energy level sidebands become truncated to two dominating contributions due to the weighting of the Bessel function in the wavefunction. The dominating sidebands occur at $\pm\alpha$. By setting $n = \alpha$ we are left with a single splitting of a given energy level:

$$E_i^{(n)} = E_i \pm qV_0 \tag{4.13}$$

$$f_i^{(n)} = f_i \pm \frac{q}{\hbar}V_0 \tag{4.14}$$

These results are mathematically analogous to Autler-Townes splitting or the AC Stark effect, with similar energy level splitting, but with different proportionality constants [142]. The similarity between the AB effect and AC Stark Effect is one key motivation for seeking spectroscopically observable proof of the scalar AB effect, as the AC Stark effect has been widely observed in many spectroscopic based experiments [143–147].

4.3 Experimental Apparatus

In previous work collaborators proposed a simple apparatus with the goal to spectroscopically observe the scalar AB effect in hydrogen like atoms, illustrated by figure (4.1) [148]. The original apparatus consisted of the quantum system , hydrogen like atoms , placed in a Faraday shell connected to a time-varied voltage source. The hydrogen like atoms would then be prepared into specific states via a scanning pump laser and the effect of the applied potential would be measured spectrally from a photodetector.

My work has expanded on the original experimental apparatus and employed various spectroscopic techniques to parse the scalar AB effect. Figure (4.2) is

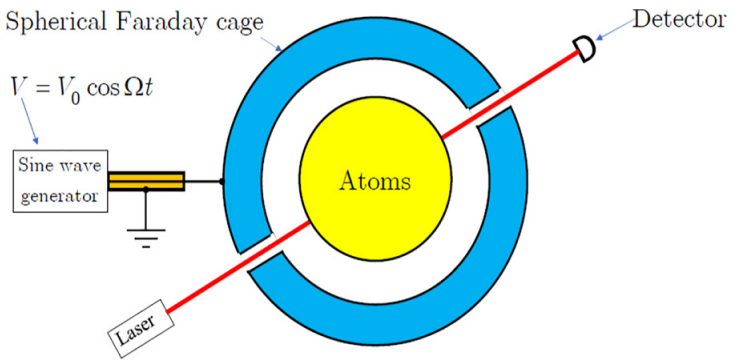

Figure 4.1: Proposed scalar AB Effect experiment with atomic gas contained within a Faraday shell. The atoms experience a time varying potential due to a time varying potential being applied via an arbitrary function generator.

a schematic of the main experimental apparatus containing the multiple excitation configurations. Figure (4.2a) depicts the atomic dressing source, based on the configurations of the Scanning Diode Lasers (SDLs) we can observe standard absorption, saturated absorption, and N-level system preparation. All three configurations are measured using Figure (4.2b) , consisting of a temperature controlled atomic vapor cell contained within a Faraday cage, with an applied time varying potential to the Faraday cage supplied by an arbitrary function generator. The absorption spectra are measured on photodiodes connected to an oscilloscope, where we can observe any effects on the absorption spectra. Utilizing only SDL1 represents a simple absorption spectroscopy measurement utilizing a single beam. This type of measurement is dominated by Doppler broadening of the spectral features and results in spectral features orders of magnitude larger than the natural linewidth of the used atomic gas [149,150].Employing both SDL1 and SDL2 to create a Probe-Pump configuration allows for a Saturated Absorption Spectroscopy (SAS) setup, which is not limited by the Doppler broadening of a single beam configuration [151]. Both configurations prepare the atoms into a Λ or V type three level system [152, 153]. Using both SDLs and an acousto-optic modulator (AOM) creates three co-propagating beams, in a Pump-Coupling-Probe configuration, to prepare the atoms into a combination of a Λ and a V type three-level systems resulting in a four-level N type system

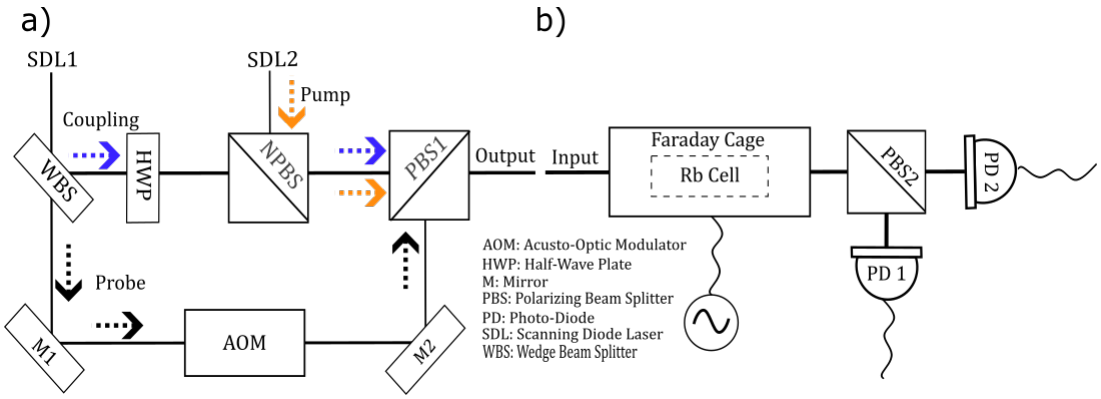

Figure 4.2: Expanded Scalar AB effect schematic. (a) Experimental setup configurations: standard absorption uses a single scanning diode laser (SDL1); saturated absorption utilizes both SDLs; N-level system utilizes both SDLs and an acousto-optic modulator (AOM) for a three-beam configuration; (b) Absorption spectra measurement scheme: temperature controlled Rb vapor cell contained within a Faraday cage, with an applied time varying potential via an arbitrary signal generator, the absorption spectra are measured on two photo-diodes connected to an oscilloscope.

4.4 Absorption Spectroscopy

As previously mentioned the goal of this work is to spectroscopically probe the scalar AB effect. Spectroscopy is the field of optics in which the properties of light are measured and studied to give information about how the light itself was created and the system the created it. In order to make any spectroscopic measurements we need a system in which spectroscopy can be performed. We have shown that hydrogen-like atoms would be the perfect candidate for exploring the AB effect,to do this the measurements themselves revolve around absorption spectroscopy. Absorption spectroscopy is a method that utilizes a material's absorption of electromagnetic radiation in order to define the material's properties and composition [154]. Atoms and materials alike selectively absorb light that is on resonance with very specific energy transitions, allowing for one to utilize broad-spectrum light and observe which frequencies are missing after the absorption takes place. If the specific energy transitions were to be shifted some amount so to would the absorption pattern, giving motivation to pursue an absorption

spectroscopy measurement of the scalar AB effect.

4.5 Rubidium Spectroscopy

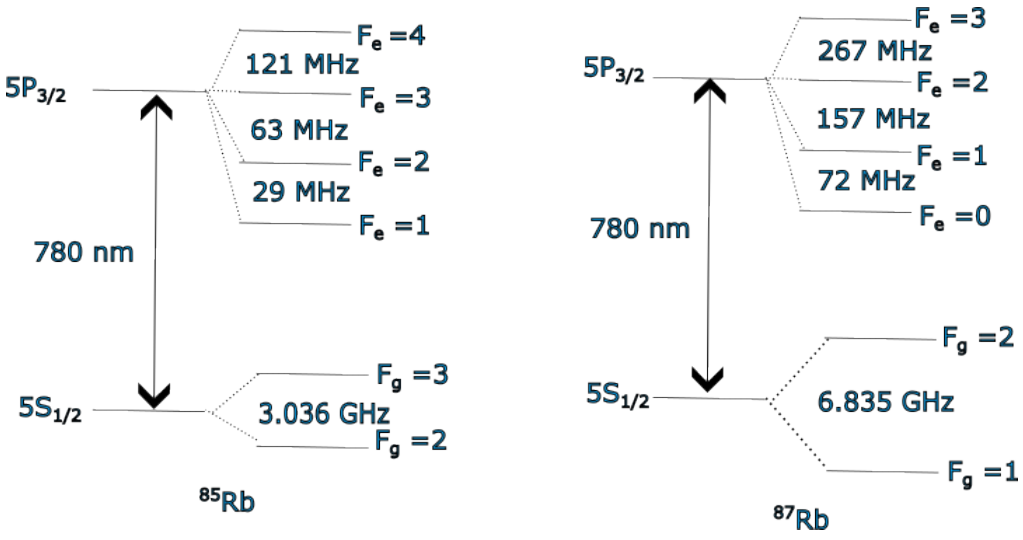

Figure 4.3: Energy level diagram for the D_2 transition lines of naturally occuring ^{85}Rb and ^{87}Rb, created from data obtained by NIST [1]. The transitions are achieved by pumping a Rb vapor cell with a 780nm light source. The excited state fine transitions are made observable by sweeping through slightly off resonance optical frequencies.

The expected energy level splitting of a hydrogen like atomic gas is determined by $\pm eV_0$ and the frequency splitting is $\pm\frac{e}{\hbar}V_0$. As a result, we expect frequency splitting on the order of $\pm 240MHz$ per $1\mu V$ of applied voltage to the Faraday cage. This shift is quite large and should be spectrally distinguishable from normally occurring spectral features, motivating us to pursue spectroscopic observations of well-known and studied atomic gases. The well studied element Rubidium represents an adequate analog to hydrogen. Rubidium (Rb) is a stable alkali metal with atomic number 37 and has two naturally occurring isotopes Rb^{85} and Rb^{87} . An important characteristic of Rb is its single occupancy of its valance shell, outer most electron orbital. It is this single occupancy in Rb's valence shell that makes it 'hydrogen like' and a good model for a charged particle with discrete energy

levels [155].As a result of its useful attributes Rb has been extensively studied in experiments observing the effects of optical pumping, AC Stark splitting, Zeeman splitting, and Bose-Eienstien condensates [145,156,157]. Since the energy states of naturally occurring Rb are well understood it is an obvious candidate for spectral exploration of the AB effect and will be the main system of interest in this work. The energy level diagram in figure (4.3) quantifies the well known energy levels of Rb^{85} and Rb^{87}.

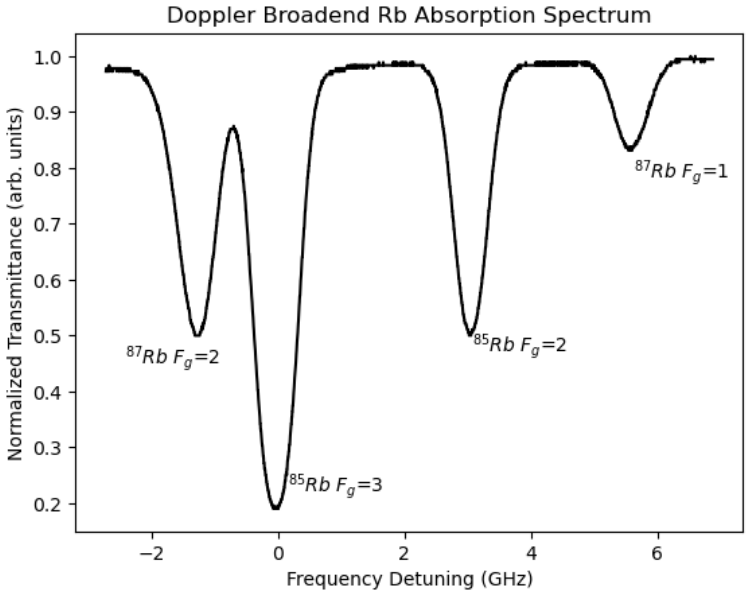

Figure 4.4: Doppler broadened ^{85}Rb and ^{87}Rb absorption spectra. Achieved by single beam absorption spectroscopy. The FWHM of the spectral features are on the order of 1GHz.

Beginning the study into the AB effect in naturally occurring Rb^{85} and Rb^{87}, we must verify the standard energy levels defined by the valence electron in the absences of any external influence. The energy levels of interest are the ground state to excited state transitions of the $5S_{1/2}$ orbital. To make these measurements we performed basic, single laser, absorption spectroscopy and observed the well known doppler broadened absorption spectrum. Our results are shown in figure (4.4) The absorption spectrum displays the Doppler broadened ground state and excited states of Rb^{85} and Rb^{87}.The Doppler broadening is a result of individual

atom motion as the atoms themselves move relative to the beam path and direction of propagation [158]. The absorption dips themselves have a FWHM on the order of 1 GHz. While our results verify the expected frequency separation of energy levels we do not have the resolution to needed observe and quantify any expected shift as a result of the AB effect. To better our resolution one must use more advanced spectroscopic techniques and resolve finer spectral features.

4.6 EIT and EIA in Rb

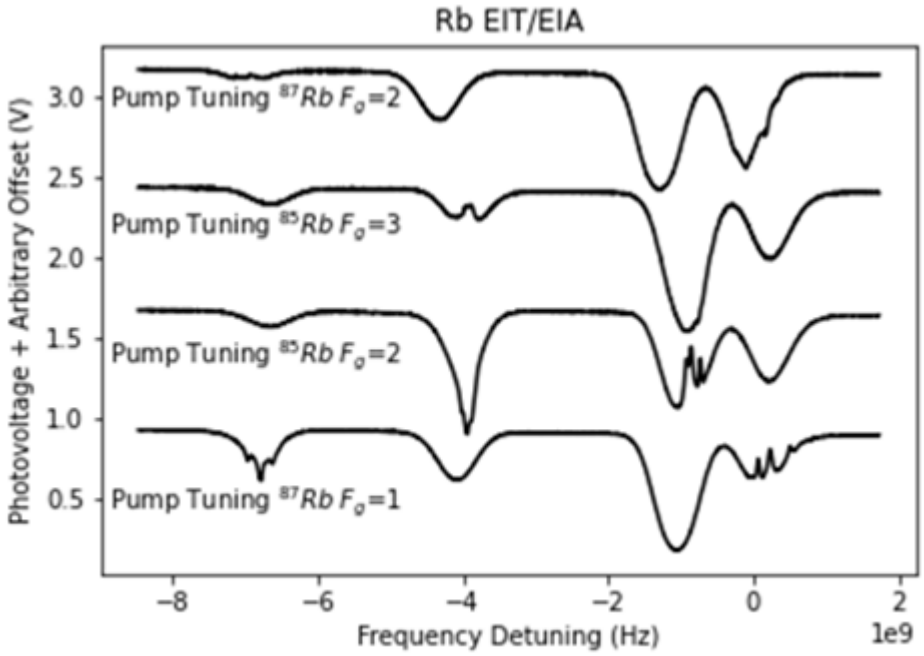

Figure 4.5: Electromagnetically induced transparency and absorption in the ^{87}Rb and ^{87}Rb spectra. Measured by dual beam absorption in which of the lasers is scanning around the transition frequency, revealing the fine transitions.

To vastly eliminate the Doppler broadening a dual beam scheme can be employed. The elimination of the Doppler broadening stems from the interference two or more coherent optical fields in the presence of an optical mediam,often creating low group velocity light or 'slow light' [159]. The two most common methods of achieving this are Electromagnetically Induced Transparency (EIT) or Electro-

magnetically Induced Absorption (EIA) [160,161]. As the names of the phenomena state EIT and EIA describe the creation of a transparency or absorption feature in a typical absorption spectra. By introducing a secondary coherent beam into the Rb absorption measurement one can make measurements of finer spectral features. The primary field is referred to as the 'probe' and is to a frequency slightly of resonance between a transition. The secondary field is referred to as the 'pump' and is tuned to a frequency far off resonance of the original transition. Based on the selection of probe and pump field one can induce either a transparency or a additional window of absorption. The Results of performing EIT and EIA measurements can be seen in figure (4.5). The results match well with common EIT and EIA experiments [162–165]. However the FWHM of the smallest features is still to large to see any fine structure elements and is on the order of a few hundred MHz. Another applicable approach would be through the utilization of Saturated Absorption Spectroscopy (SAS).

4.7 Saturated Absorption in Rb

SAS utilizes the same process of applying two optical fields to a optical media but the fields themselves are aligned and counter-propagating. The opposed fields interfere such that only atoms that have a relative velocity of zero contribute to the probe field's absorption spectra, eliminating Doppler broadening for the full scanned spectra [151].SAS is well explored in Rb and is the common method for spectral measurements of atomic gases at various temperatures [166–168]. This method allows one to observe fine transtions of electrons within an atomic gas . Performing these measurements allowed for the observation of the well known fine transitions of Rb^{85} and Rb^{87}. Our results are shown in figures (4.5-4.6) and match well with the expected transitions. The spectral features of these fine transitions have FWHM on the order of 100Mhz. With this resolution of spectral features it should be possible to see the influence of the AB effect on the fine transitions of Rb.

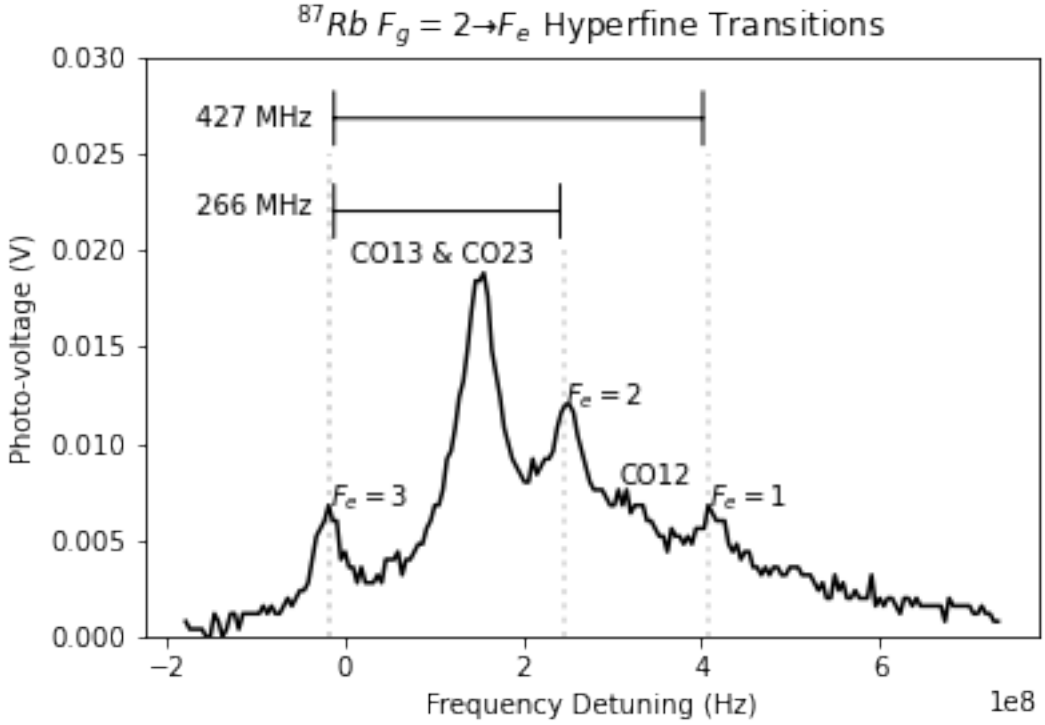

Figure 4.6: Doppler free saturated absorption spectrum in ^{87}Rb revealing fine transitions. The frequcy difference between the fine transitions is displayed along with the expected cross-over features

4.8 Selecting α

According to equation (4.8), the phase modulation depth parameter α depends on the values of amplitude and modulation rate for our time varying potential. Notably for increasing values of α, there is a significant decrease in the peak optical power contained in the sidebands, causing motivation for minimizing the value of α while maintaining experimentally realistic values for the applied voltage and frequency [169]. Figure (4.7) shows the relationship between the value of α, modulation frequency and modulation amplitude. A defined region of visibility can be created by limiting our values to a region between the natural linewidth of $Rb_8 5$ of 6 MHz and the ground state transition separation of 3.05GHz. The measurements performed in my work utilize $\alpha = 1000$, this implications of this selection will become important later in this work.

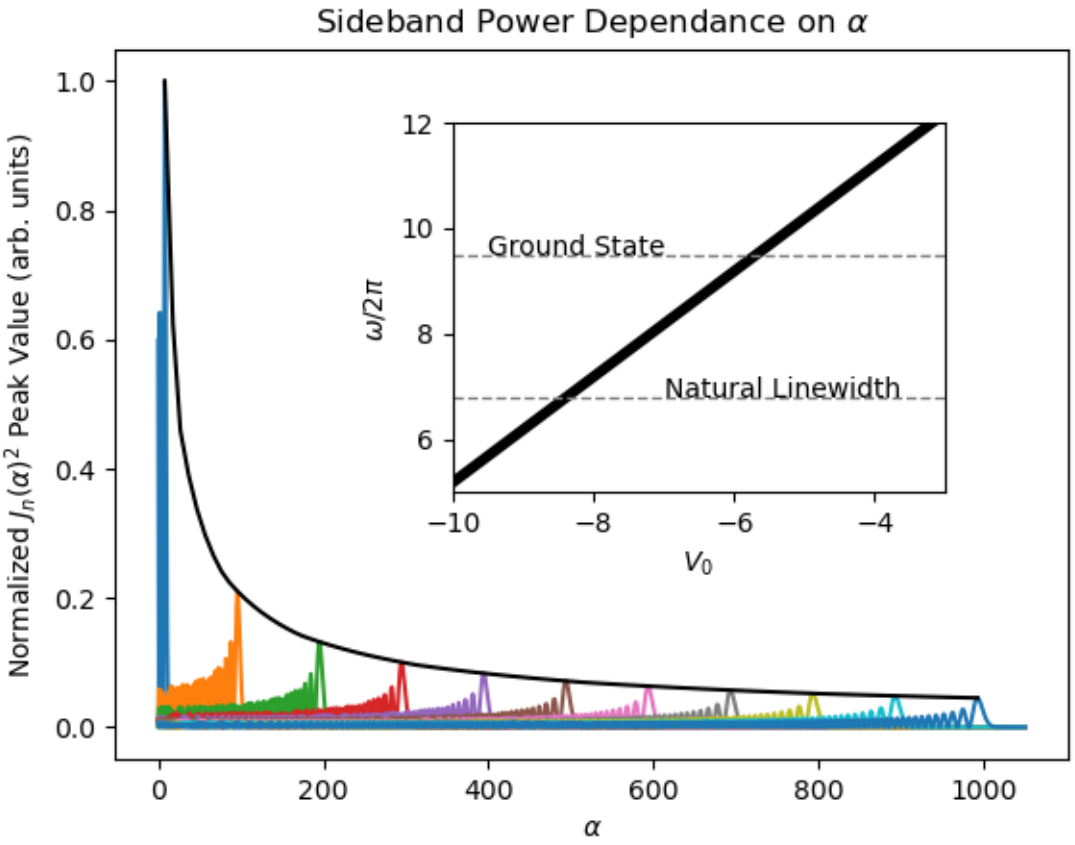

Figure 4.7: Graphical representation of the phase modulation depth parameter α and its dependence on the applied potential's frequency ω and amplitude V_0. In the main plot the normalized squared value of the Bessel function is plotted showing a decrease in peak value as a function of α. The inset depicts, for $\alpha = 1000$, the accepted values of frequency ω and amplitude V_0. Also depicted, are the ground state transition and natural linewidth frequencies, which form a boundary of optical observability as any spectral effect must occur between these two boundaries in order to have any visible effect on the spectra.

4.9 Exploring AB Effect in Rb

Figure (a-b4.8) depicts the results of Rb absorption experiments and compares them to the Nakayama model with the inclusion of an AB splitting effect of all allowed energy levels [138, 139]. Figure (4.8a) contains the well-known Doppler broadened absorption spectrum of a vapor cell containing both naturally occurring

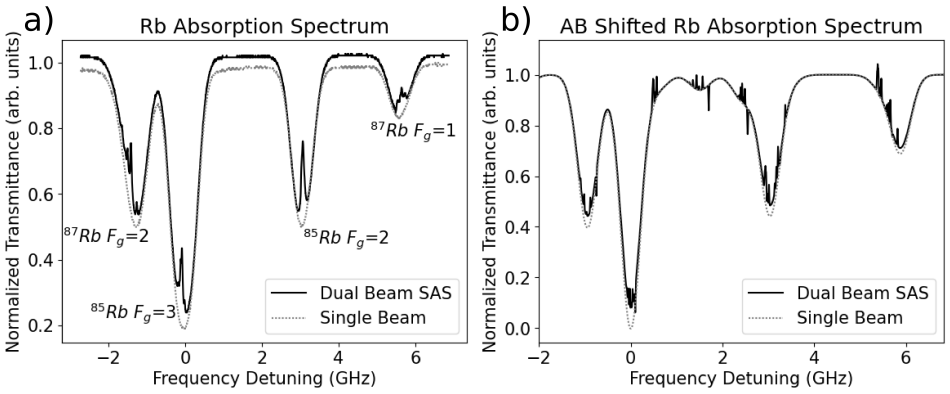

Figure 4.8: Experimentally measured and calculated absorption spectra: (a) Both Doppler broadened and Doppler free Rb absorption spectra measured through standard absorption and saturated absorption techniques, with an applied time varying potential of $V_0 \approx 10\mu V$ (b) theoretical AB shifted Rb spectra.

Rubidium 85 and 87. The spectrum was obtained by utilizing a standard single beam technique depicted in figure (4.2) and measured using the scheme in figure (4.2). A time varying potential with amplitude 10uV was applied to the Faraday cage to stimulate the AB effect. Figure (4.8b) shows the theoretical expected spectrum of figure (4.8a), including the AB effect as a splitting of the of the energy levels shifted $\pm$2450 MHz, corresponding to an applied time varying potential of 10uV. The theoretically generated spectrum has slightly distinguishable features resulting from the splitting of energy states. When comparing the two we can see that the experimental results show no evidence of the AB effect. However, due to doppler broadening, the spectral features have FWHM on the order of 1GHz and may be smearing out the small, in amplitude, effects shown in the theoretical data. To better our sensitivity to these features we were motivated to eliminate the doppler broadening effect by implementing a two beam SAS configuration and performing the same measurements.

Figure (4.8a) also contains the fine transition absorption spectrum of Rb_{85} and Rb_{87}. This spectrum was obtained by performing a standard dual beam SAS technique. The same time varying potential was applied to the Faraday cage. Shown in the theoretically generated spectrum, many obvious spectral features arise from

the splitting of states. Despite many of the expected hyperfine transitions being visible in the experimental spectrum, there is no definitive evidence of AB splitting of normally observable states. The FWHM of the spectral features is on the order of 100MHz and may still be too large for observations of the AB effect. These results motivate us to pursue techniques that will allow for better resolution of the spectral features and observations of other similar spectroscopic effects in the same experimental apparatus.

4.10 N-Level System

As mentioned earlier in the paper, the AC Stark effect is a mathematical analog to the scalar AB effect but the shift of energy eigen values is proportional to the applied field modulation rather than the electric potential modulation. The AC Stark effect generates spectral features comparable with the natural linewidth of the fine transitions of Rb [142]. The similarity and spectral resolution of the AC Stark effect motivated us to observe this analogous effect in the same experimental apparatus. Along with this we sought to observe electromagnetically induced absorption and transparency (EIA, EIT), while in the setting of our experiment. Work done by Bankim Chandra, Das et. al. shows the interplay of EIT, EIA, and AT Splitting in a single optical system [162]. Following in a similar fashion our experimental setup was altered to combine the V and Λ transitions of Rb_{85} $F_g = 2$ to $F\prime = 1, 2$ and $Fg = 2, 3$ to $F\prime = 1, 2$ into a four level N-type system. The optical configuration consists of three co-propagating beams passing through the Rb cell. The rabi-frequencies of the probe and pump beam were held at fixed values, $\Omega_{probe} = 3MHz$ and $\Omega_{pump} = 18MHz$. The coupling beam's Rabi frequency Ω_c was varied from 19MHz to 39MHz. By varying the rabi frequency of the coupling beam we were able to observe the transitions between EIT , EIA , and AT splitting in our absorption spectra shown in figure (4.9). The resulting spectral features allowed us to achieve frequency resolution of 5-12 MHz in comparison to the natural line width of these fine transitions of 6 MHz. Applying a time varying potential did not result in any noticeable spectral change. While this may seem disheart-

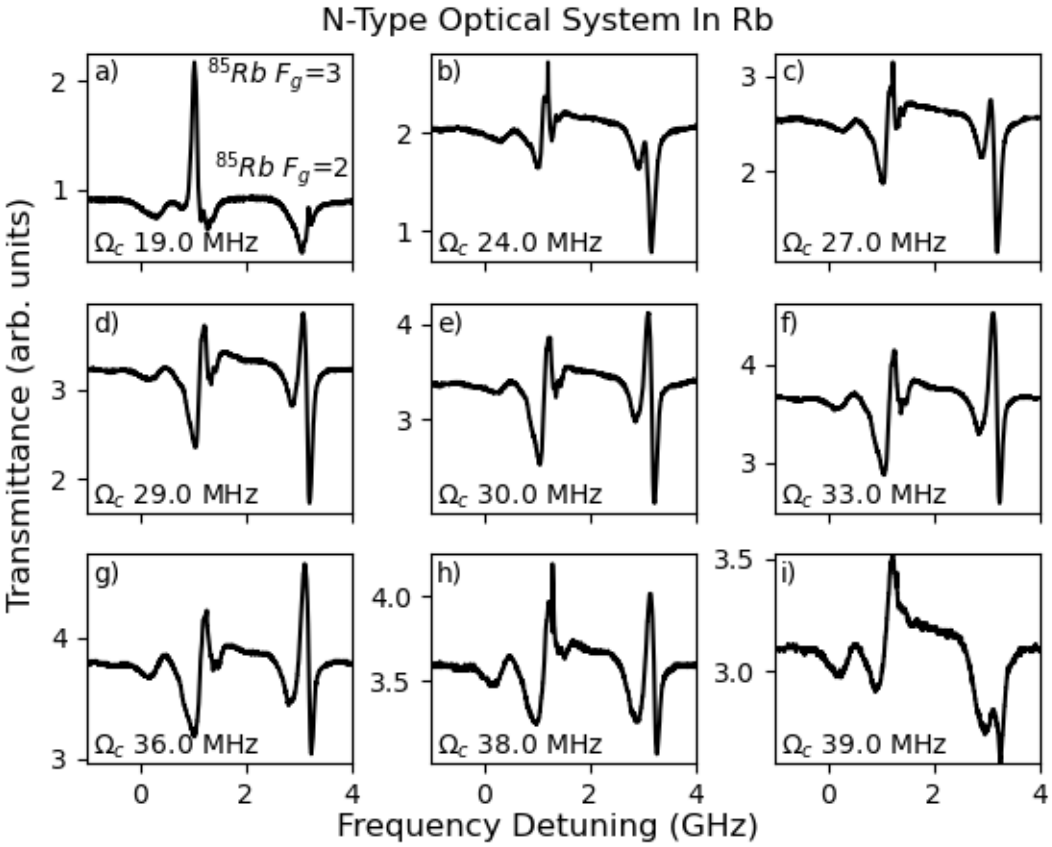

Figure 4.9: (a-i) N-level system Rb absorption spectra for different values of rabi-frequency Ω_c, with the same applied time varying potential. This data was collected using the N-level configuration presented in figure (4.2).The spectral features are depicting changes in the Rb_{85} absorption spectra and show transitions between EIA,EIT and AT splitting.

ening, we were motivated to look for possible explanations causing the absence of detectable observations of the scalar AB effect.

4.11 Rb side band power decay

To better understand the lack of observable influence of the AB effect on our system, we needed to calculate optical power contained in the generated sidebands. By modeling our system as a phase modulated CW light source, we can determine

the optical power in any given sideband.
We can express the electric field of a CW light source, with frequency ν_0, as:

$$E_{cw}(t) = E_0 \exp -i\nu_0 t \tag{4.15}$$

Applying a sinusoidal phase modulation with frequency f_m and modulation index $\Delta\theta$, simplifies to weighted Bessel functions:

$$E_{pm}(t) = E_0 \exp(-i[\nu_0 t + \Delta\theta \sin(2\pi f_m t)]) \tag{4.16}$$

$$= E_0 \sum_{n=-\infty}^{\infty} \mathcal{J}_n(\Delta\theta) \exp(-i[\nu_0 t + 2\pi n f_m t]) \tag{4.17}$$

We know that optical power after phase modulation is proportional to $|E_{pm}|^2$ so the optical power in the nth sideband can be expressed as:

$${}^{n}P_{pm} = |E_0|^2 |\mathcal{J}_n(\Delta\theta)|^2 \tag{4.18}$$

We can see that the optical power in any given side band is proportion to $|\mathcal{J}_n(\Delta\theta)|^2$ plotting this reveals the optical power for all sidebands decays rapidly, shown in the x-z projection of figure (4.10) . Previously discussed, our dominating sidebands occur at $n = \alpha$ and in the experimental configurations $\alpha = 1000$. The power ratio in the 1000th sideband is negligible and as a result should not be detectable in our spectra. In order to observe any effect on our spectra, we would need to be able to 'push' power into a desired sideband. Luckily, work has been previously done to flatten out the optical power spectra for multi carrier light and should be applicable in our experiment.

Yamamoto et al. has presented a method to correct for the power decay in optical sidebands due to phase modulation [170]. In their work they show that by adding additional phase modulation and a specified dispersive media one can flatten their optical power spectra and achieve elongated power bandwidths over

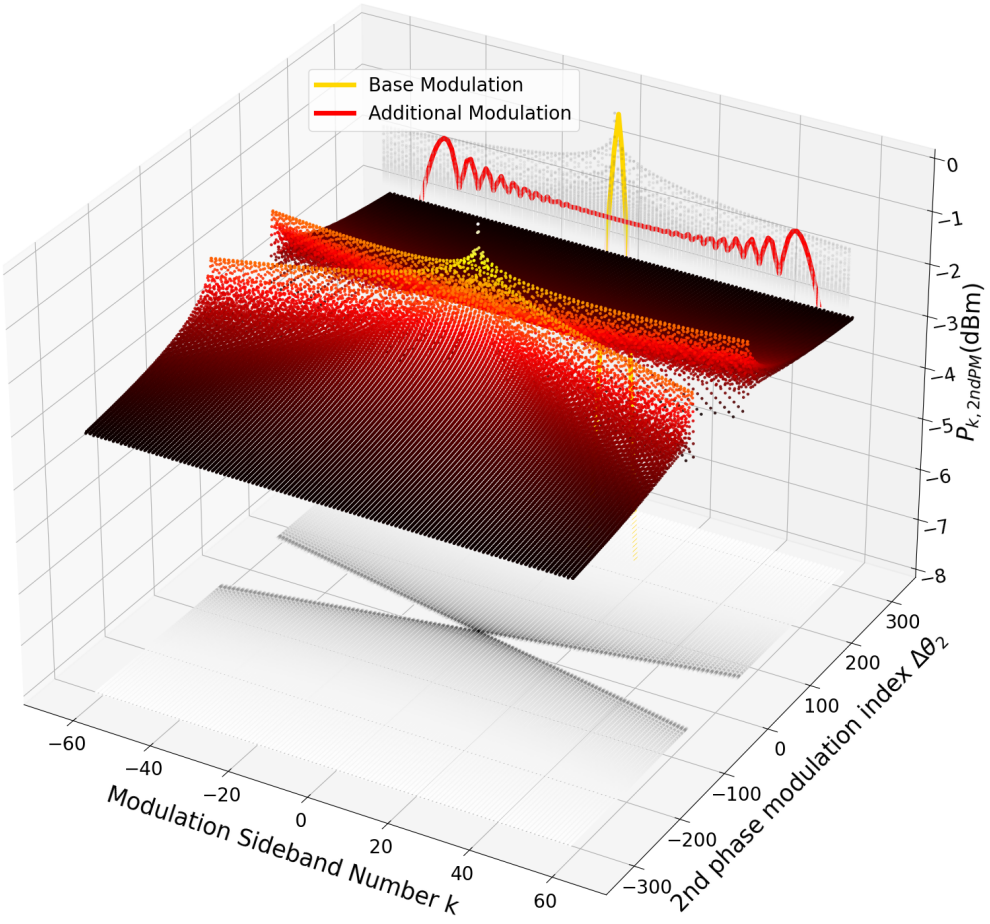

Figure 4.10: Three-dimensional representation of the optical power (z-axis) contained in each sideband (y-axis) for varying values of additional correcting phase modulation (x-axis). The ZY projection depicts the overall trend in optical power for all sidebands as well as two specific configurations displaying the flattening of the power bandwidth when including additional phase modulation. The XY projection is a two-dimensional density plot that reveals the specific values of $\Delta\theta_2$ for any sideband that maximizes the optical power, which fall along the dark X-shape. The three-dimensional surface displays the optimal value of the second phase modulation index $\Delta\theta_2$ for any given optical sideband number.

any number of optical sidebands. We can implement these methods to achieve better optical visibility of the AB effect. To see this, we should derive the evolution of the electric field as it passes through the various components.

Considering our experiment to be modeled by a phase modulation, PM, with modulation index $\Delta\theta = \alpha$ the electric field and optical power in the nth sideband are given by:

$$E = E_0 \sum_{n=-\infty}^{\infty} \mathcal{J}_n(\alpha) \exp(-i[\nu_0 t + 2\pi n f_m t]) \tag{4.19}$$

$$^{n}P = |E_0|^2 |\mathcal{J}_n(\alpha)|^2 \tag{4.20}$$

If we add a dispersive media, following the PM, with a group velocity dispersion of B_2 the electric field and power in the nth optical sideband will follow:

$$E_{dm}(t) = E_0 \sum_{n=-\infty}^{\infty} \mathcal{J}_n(\alpha) \exp\left(i[\phi_n - 2\pi n f_m t]\right) \tag{4.21}$$

$$\phi_n = 2\pi^2 n^2 f_m^2 B_2 \tag{4.22}$$

$$^{n}P_{dm} = |E_0|^2 |\mathcal{J}_n(\alpha)|^2 \tag{4.23}$$

We can see that the power in the nth optical sideband is unchanged however the phase modulation is transformed to intensity modulation and the waveform follows:

$$P_{dm}(t) = |E_0|^2 \left| \sum_{-\infty}^{\infty} \mathcal{J}_a(\alpha) \exp\left(i[\phi_n - 2\pi n f_m t]\right) \right|^2 \tag{4.24}$$

Adding an additional PM with modulation index $\Delta\theta_2$, where t_{diff} is the timing difference of modulations, results in an electric field expressed as:

$$E_0 \sum_{k=-\infty}^{\infty} \sum_{n=-\infty}^{\infty} \mathcal{J}_n(\alpha) \mathcal{J}_{k-n}(\Delta\theta_2) \exp\left(i[\phi_n + \phi_{diff} - \nu_0 t - 2\pi k f_m t]\right) \tag{4.25}$$

$$\phi_{diff} = 2\pi(k-n)t_{diff} \tag{4.26}$$

Applying this model, we can scan through various sideband values and phase modulation indices, for specific values of $\Delta\theta_2$ in which a flattening of the optical power distribution occurs and results in an overall increase of power bandwidth for any given sideband. By flattening the optical sideband power distribution, we can effectively 'push' power into any number of optical sidebands. The flattening of the optical power distribution can be seen in figure (4.10) where the three-dimensional scatter plot depicts the optical power (z-axis) in any given sideband (y-axis) for specific values of $\Delta\theta_2$ (x-axis). The two-dimensional density projection of the x and y axes reveals the specific values of $\Delta\theta_2$ that maximize the power in a specific sideband. The projection of the y and z axes depicts a density distribution of optical power in the sidebands. Two examples of optical sideband power distribution, for specific values of $\Delta\theta_2$, are given alongside the density projection. We can see that the flattening of the distribution of optical power results in a more even distribution of power to multiple sidebands. An advantage of this is that each individual sideband can result in an additional spectroscopically observable feature. In our case, this may result in generating more optically detectable artifacts of the electric scalar AB effect on the Rb absorption spectra. Through simulations, at the desired sideband of $\alpha = 1000$, we can arrive at a configuration in which the power spectrum is flattened and dispersed into a multitude of optical sidebands. One configuration which results in a desirable flattening is with the inclusion of a dispersive media with group velocity dispersion of $B_2 = \frac{1}{4\pi f_m^2}$ and a second phase modulator with a modulation index of $\Delta\theta_2 = \frac{\pi}{4}$.

4.12 Results

Despite not directly observing the AB effect, in our current setups, we have demonstrated that the optical effect should not be visible due to optical sideband decay as a result of the phase modulation that occurs. We presented a model that corrects this by adding a dispersive media and additional phase modulation.

To experimentally implement the simulated results a corrected setup should consist of our original system but with the addition of a dispersive media with value $B_2 = \frac{1}{4\pi f_m^2}$ and an additional PM with modulation index $\Delta\theta_2 = \frac{\pi}{4}$.The dispersive media can be that of a meta material or simply a photonic crystal fiber that can produce an arbitrary tunable GVD [171, 172]. The second PM could be an additional Rb vapor cell setup or more easily an optical phase modulator [173]. Moving forward we will seek to experimentally implement the sideband power corrections and optimize our selection of α to improve the visibility of the AB effect on our system. We also plan to implement another form of charged particle model into our system. One promising way to do this is to utilize a quantum dot or semiconductor crystal as an analogous multi-level system [174].Motivation for this stems from our simplification of the atomic structure of a hydrogen like atom; our model considers the electron to be a negatively charged particle orbiting a positively charged nucleus. These simplifications ignore that the applied potential is from outside the atom and as a result may observe the atom, as a whole, as a neutral particle. While our findings do not provide concrete experimental evidence of the scalar AB effect, we have demonstrated useful spectroscopic techniques to achieve spectral feature tuning and presented methods to better the visibility of power diminished optical sidebands. These results are not only a strong reasoning for continuing the pursuit of spectroscopically observing the AB effect but show promise in applications to Atomic and Molecular Optics. Laser locking, atomic clocks, optical frequency standards and arbitrary optical waveform generation would benefit from tunability of optical features. In the process of generating frequency combs, one could apply these techniques to increase the density of lines in any desired comb. Quantum state preparation is a key to achieving viable quantum computers and these methods could be used to generate robust quantum states. Overall, we have defined limits on spectroscopically observing the electric scalar AB effect in Rb, achieving resolution of spectral features on the order of the natural line-width of the transitions. We expect that in order to make a spectral measurement of the scalar AB effect one will need to implement our method to enhance the optical sideband power diminished by the innate phase modulation that occurs due to the

applied time modulated electric potential.

Chapter 5

Conclusions and Next steps

Through this PhD work, various quantum optical effects were explored in theory and via experimental probing. Starting with the exploration of the Doppler effect on SPDC generated entanglement, laying the foundation for entanglement enhanced LiDAR measurements. The importance of beam characterization in the efficient generation of entangled photon pairs was discussed and quantified. Two methods of probing the Doppler effect were presented alongside theory providing direct path for future continuation of this research.

The second portion of this work found itself focused onto the mechanisms behind the optical Kerr effect resulting in the generation of entangled pairs in optical fiber. All of this with the purpose of questioning the effect quantum interference has on entangled photon pairs. The theory of the quantum interference effect known as the HOM effect was explored and measurement scheme to probe the time reversed HOM effect was highlighted.

As a final addition to the theme of exploring quantum optical effects generated by outside stimulus, the electric scalar AB effect was explored. The findings resulted in an optical setup with the ability to prepare and evaluate atomic states, with functionality useful to frequency locking and spectral feature generation. Through the use of theory, models were developed to predict optimal configurations and results. Despite experimental results not fitting original exceptions many useful findings were presented, invaluable skills developed and avenues for promising fruitful work revealed. This concluding section will focus on tangible

next steps in probing the electric scalar AB effect and other prospective areas of interest in the realm of quantum optics.

5.1 Phase Modulation Communication

One key takeaway from the experimental efforts to verify the scalar AB effect is the introduction of a phase dependent flattening of optical sidebands of a phase modulated signal. In our work we found that the scalar AB effect is drastically obfuscated by a lack of optical power in the particular sidebands that the effect would present itself in. The lack of optical power is attributed to the phase modulation that is intrinsic to the AB effect . While this can be viewed as detrimental to observing the AB effect, this obfuscation can be utilized in a way that is beneficial in a communication application. In a scenario where one seeks to encode information optically via the scalar AB effect or some other method of phase modulation, if the encoded information is contained within an optical sideband that is effected by this optical power fall off, the information cannot be detected. However, if one could restore optical power into the desired sideband then the information could then be interpreted. By applying a specific configuration of dispersion media and additional phase modulation one can flatten the optical sideband structure and restore detectable power into any desired sideband. Noting that the 'specific configuration' is dependent upon the original phase modulation configuration and the desired optical sideband. Without prior knowledge of the original optical source configuration, the information will remain unobservable by a secondary party. One can extend similarities to common encryption techniques for communication and see a possible technological application of this phenomena [5, 6]. A direct useful configuration that can utilize this form of 'encryption', would be a cascade dual SAS scheme using the very same techniques detailed in this manuscript.

5.1.1 Cascaded SAS System

Utilizing our base AB effect apparatus and adding a dispersion media with a specific or tunable GVD we can transform the phase modulation into inten-

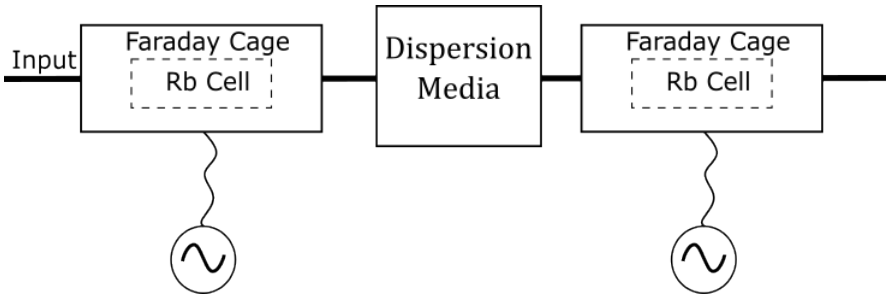

Figure 5.1: Dual SAS scheme utilizing the three beam N-level system preparation. An additional dispersion media with a strategically tuned GVD is added alongside another Rb cell with a specific time varying potential. These additional components flatten the optical sideband power spectra such that any desired sideband can be be optically observed, negating the effects of optical power falloff due to the original phase modulation.

sity modulation following equation (4.24). Expanding on the dispersion media by adding an additional Rb cell stage, we can then tune the time varying potential to a specific modulation index such that our desired sideband α is optically detectable. A simplified schematic can be seen in figure (5.1) where the input is simply the original three beam N-level system preparation configuration. Utilizing equation (4.25) and knowing the specific frequency of modulation of the time varying potential , f_m, and value of α one can 'restore' the visibility of any information encoded by the original Rb cell stage.

5.1.2 Simulation

Through the previously covered simulation data we can determine optimal values via simulation of the optical configurations using equation (4.25). For an optical source of 1W used to 'encode' information into the $n = \alpha_1 = 1000$ sideband we can apply a dispersion media with $B_2 = \frac{1}{4\pi f_m^2}$ and a secondary Rb cell stage with $\alpha_2 = \frac{\pi}{4}$. Doing so will result in an optical power of $20\mu W$ in the desired sideband of $n = 1000$. While compared to the original carrier power the output power is significantly reduced. However when comparing the power in the same sideband without the additional phase modulation it becomes obvious that this method results in a desirable effect. In figure (5.2) we can see the comparison in

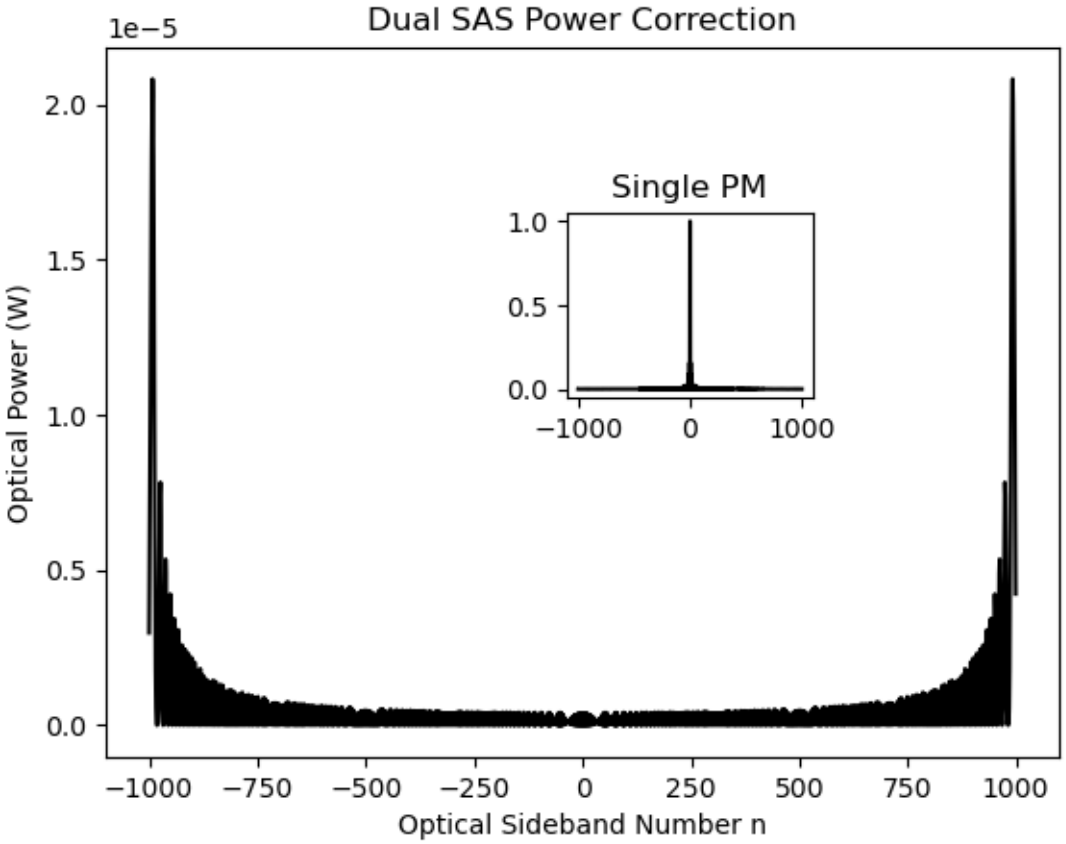

Figure 5.2: Comparison of a single instance of phase modulation and the case with an additional phase modulation. The sideband of interest occurs at n=1000.For a single phase modulation the sideband is undetectable.

the $n = 1000$ sidebands, for a scheme without additional phase modulation there is virtually no optical power. While this may not be a power efficient method of encryption it is still promising as many optical sensors are sensitive enough to detect optical powers on the order of a few micro-Watts [111]. While these simulations pertain specifically to the presented apparatus many different phase modulation techniques could be possibly be implemented [175–177].

5.2 Machine Learning and Optics

One consistent trait of all the previously mentioned works, is that they all need computational analysis and modeling. Through the task of studying various quantum optical effects one is able to develop key skills and insights into the adjacent field of computer science. As a result of this many interesting interdisciplinary opportunities present themselves and require the use of skills and knowledge from both fields. A good example of this is the use of machine learning to identify specific features in optical spectra. Artificial intelligence and machine learning strategies have been proven to be very effective in many classification settings and as a result have been adapted to be used in various spectroscopic experiments [178–181]. While the benefits of using machine learning is obvious in classification functionality it is not limited to it. Neural networks are one of the pillars of machine learning approaches and are fundamentally a powerful mathematical model that can be used to approximate nonlinear functions [182]. Non-linearity is a driving component in optical phenomena, as presented in this manuscript many optical effects are a result of special optical properties that can be described by non-linear functions. The key focus of non-linearity in both optics and neural networks has led to many proposing optical interpretations of neural networks [183–188]. Following in this vain my future work seeks to study the efficacy and viability of an all optical neural network.

5.2.1 Optical NN

While still in the developmental stages of producing an all optical neural network, here we will present a feasible first step and cover the basic functionality of a neural network. Neural networks themselves are a type of machine learning model inspired by the structure and functioning of the human brain [189]. Neural networks consist of layers of interconnected units called neurons or nodes, which process input data and pass it along to the next layer. Each neuron in a neural network can be represented by a mathematical function that takes in inputs, processes them, and outputs a result. When a neuron receives an input it applies a

weight, which determines the importance of the input, adds a bias term, and passes the result through an activation function to produce an output. Activation functions themselves are inherently non-linear in order to model complex systems [182]. The simplest neural network consists of one neuron and was introduced by Frank Rosenblatt in 1958, known as a perceptron [190]. A perceptron can perform binary classification and does not have the ability to approximate non-linear functions. However, by 'stacking' multiple perceptrons into various layers one can create an artificial neural network known as a multi-layer perceptron which can approximate non-linear models [191].

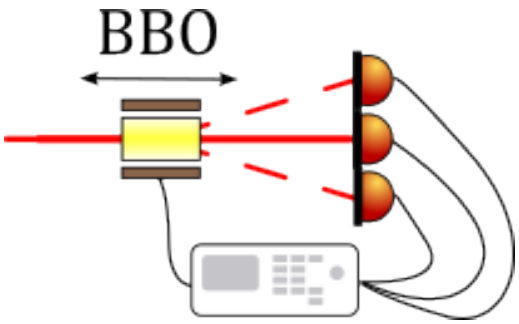

Figure 5.3: Simple optical perceptron scheme consisting of a BBO $\chi^{(2)}$ non-linear crystal modulated by an applied electric field inducing an optical Pockels effect, which varies the index of refraction and thus changes the propagation of the optical input beam through the medium. The output beam is detected on one photo-diode from an array, this output will correspond to a specific assigned value. A time delay can be introduced by a physical translation of the crystal, adding an additional tunable parameter. By adjusting the field and position of the crystal it can be optically 'trained' to output to a specific photo diode for a specific optical input. In a sense the tunable parameters correlate to the weights used in a traditional neuron scheme.

The first step in implementing a fully optical neural network will be in producing a fully optical perceptron. Utilizing the non-linearity of various optical materials one should be able to bestow the defining characteristics of a single neuron. One method of experimental observation is depicted in figure (5.3) where the Pockels effect is utilized to change the index of refraction of a BBO crystal altering the input beam's propagation through the media, modeling the 'weight' characteristic of a neuron. The bias characteristic can be defined by a time or

phase delay being applied to the propagating light. With the combination of these characteristics one can implement a feedback loop in a way that alters these characteristics to effectively train the neuron to have a specific output for a given input. In this case the training will occur by optimizing the photo current of the expected photo-diode. To do this we can utilize equation (5.1) which describes the change in refractive index as a function of applied potential and crystal length. This processes can be made fully autonomous by implementing a feedback loop such as a PID controller [192]. Once a fully optical perceptron is realized then integrating multiple will lead to a viable and more robust all optical neural network.

$$\Delta n = r_{ij} n_0^3 \frac{V}{L} \tag{5.1}$$

Bibliography

[1] J. E. Sansonetti. Wavelengths, Transition Probabilities, and Energy Levels for the Spectra of Rubidium (Rb I through Rb XXXVII). *Journal of Physical and Chemical Reference Data*, 35(1):301–421, March 2006.

[2] Yanhua Shih. *An Introduction to Quantum Optics: Photon and Biphoton Physics (Series in Optics and Optoelectronics) 1st Edition*. CRC Press, 2011.

[3] Mark Fox. *Quantum optics: an introduction*. Number 15 in Oxford master series in physics. Oxford University Press, Oxford ; New York, 2006.

[4] Mirko Lobino, Dmitry Korystov, Connor Kupchak, Eden Figueroa, Barry C. Sanders, and A. I. Lvovsky. Complete Characterization of Quantum-Optical Processes. *Science*, 322(5901):563–566, October 2008.

[5] Gorjan Alagic, Tommaso Gagliardoni, and Christian Majenz. Unforgeable Quantum Encryption. In *Advances in Cryptology – EUROCRYPT 2018*, volume 10822, pages 489–519. Springer International Publishing, Cham, 2018.

[6] Dimitris Kanakidis, Apostolos Argyris, Adonis Bogris, and Dimitris Syvridis. Influence of the Decoding Process on the Performance of Chaos Encrypted Optical Communication Systems. *Journal of Lightwave Technology*, 24(1):335, January 2006.

[7] John Wood Campbell, Perry A. Chapdelaine, Tony Chapdelaine, George Hay, Isaac Asimov, and A. E. Van Vogt. *The John W. Campbell letters*. AC Projects, Franklin, TN, 1985.

[8] Gilbert Grynberg, Alain Aspect, and Claude Fabre. Introduction to Quantum Optics. page 697.

[9] J. P. Gordon, H. J. Zeiger, and C. H. Townes. The Maser—New Type of Microwave Amplifier, Frequency Standard, and Spectrometer. *Physical Review*, 99(4):1264–1274, August 1955.

[10] Mario Bertolotti. *Masers & lasers: an historical approach*. CRC press, Boca Raton, 2nd ed edition, 2015.

[11] Peter Lutzmann, Benjamin Göhler, Chris A. Hill, and Frank van Putten. Laser vibration sensing at Fraunhofer IOSB: review and applications. *Optical Engineering*, 56(3):031215, November 2016. Number: 3.

[12] Jeff Hecht. Short history of laser development. *Optical Engineering*, 49(9):091002, September 2010.

[13] Boris V. Zhdanov and Randy J. Knize. Review of alkali laser research and development. *Optical Engineering*, 52(2):021010, October 2012.

[14] A. L. Schawlow and C. H. Townes. Infrared and Optical Masers. *Physical Review*, 112(6):1940–1949, December 1958.

[15] Barry C. Barish and Rainer Weiss. LIGO and the Detection of Gravitational Waves. *Physics Today*, 52(10):44–50, October 1999.

[16] M Ferray, A L'Huillier, X F Li, L A Lompre, G Mainfray, and C Manus. Multiple-harmonic conversion of 1064 nm radiation in rare gases. *Journal of Physics B: Atomic, Molecular and Optical Physics*, 21(3):L31–L35, February 1988.

[17] A. Ashkin. Acceleration and Trapping of Particles by Radiation Pressure. *Physical Review Letters*, 24(4):156–159, January 1970.

[18] Danai Khemasuwan, Atul C. Mehta, and Ko-Pen Wang. Past, present, and future of endobronchial laser photoresection. *Journal of Thoracic Disease*, 7(Suppl 4):S380–388, December 2015.

[19] Mats Ormö, Andrew B. Cubitt, Karen Kallio, Larry A. Gross, Roger Y. Tsien, and S. James Remington. Crystal Structure of the ***Aequorea victoria*** Green Fluorescent Protein. *Science*, 273(5280):1392–1395, September 1996.

[20] Andrew Neice. Methods and Limitations of Subwavelength Imaging. In *Advances in Imaging and Electron Physics*, volume 163, pages 117–140. Elsevier, 2010.

[21] Davide Castelvecchi. Hunt for gravitational waves to resume after massive upgrade. *Nature*, 525(7569):301–302, September 2015.

[22] Louay Eldada. Optical communication components. *Review of Scientific Instruments*, 75(3):575–593, March 2004.

[23] Christiaan Huygens. *Treatise on light In which are explained the causes of that which occurs in reflexion, & in refraction and particularly in the strange refraction of Iceland crystal.*

[24] J. David Zook. A simple model for diffuse reflection. *Optics Communications*, 17(1):77–82, April 1976.

[25] Max Born and Emil Wolf. *Principles of optics: electromagnetic theory of propagation, interference and diffraction of light*. Cambridge university press, Cambridge New York, 7th (expanded) ed edition, 1999.

[26] Demetrios N. Christodoulides, Iam Choon Khoo, Gregory J. Salamo, George I. Stegeman, and Eric W. Van Stryland. Nonlinear refraction and absorption: mechanisms and magnitudes. *Advances in Optics and Photonics*, 2(1):60, March 2010.

[27] R. Paschotta. Acousto-optic Modulators - an encyclopedia article. In *RP Photonics Encyclopedia*. RP Photonics AG, 2008.

[28] William Bragg. The reflection of X-rays by crystals. *Proceedings of the Royal Society of London. Series A, Containing Papers of a Mathematical and Physical Character*, 88(605):428–438, July 1913.

[29] Christopher J. Sarabalis, Raphaël Van Laer, Rishi N. Patel, Yanni D. Dahmani, Wentao Jiang, Felix M. Mayor, and Amir H. Safavi-Naeini. Acousto-optic modulation of a wavelength-scale waveguide. *Optica*, 8(4):477, April 2021.

[30] Sang-Hee Shim, David B. Strasfeld, Eric C. Fulmer, and Martin T. Zanni. Femtosecond pulse shaping directly in the mid-IR using acousto-optic modulation. *Optics Letters*, 31(6):838, March 2006.

[31] M. Delgado-Pinar, D. Zalvidea, A. Diez, P. Perez-Millan, and M. Andres. Q-switching of an all-fiber laser by acousto-optic modulation of a fiber Bragg grating. *Optics Express*, 14(3):1106, 2006.

[32] M. A. Dugan, J. X. Tull, and W. S. Warren. High-resolution acousto-optic shaping of unamplified and amplified femtosecond laser pulses. *Journal of the Optical Society of America B*, 14(9):2348, September 1997.

[33] Jean-Yves Duclos and André-Marie Taptué. Polarization. In *Handbook of Income Distribution*, volume 2, pages 301–358. Elsevier, 2015.

[34] Aaron Bramson, Patrick Grim, Daniel J. Singer, William J. Berger, Graham Sack, Steven Fisher, Carissa Flocken, and Bennett Holman. Understanding Polarization: Meanings, Measures, and Model Evaluation. *Philosophy of Science*, 84(1):115–159, January 2017.

[35] Fucai Liu, Shoujun Zheng, Xuexia He, Apoorva Chaturvedi, Junfeng He, Wai Leong Chow, Thomas R. Mion, Xingli Wang, Jiadong Zhou, Qundong

Fu, Hong Jin Fan, Beng Kang Tay, Li Song, Rui-Hua He, Christian Kloc, Pulickel M. Ajayan, and Zheng Liu. Highly Sensitive Detection of Polarized Light Using Anisotropic 2D ReS. *Advanced Functional Materials*, 26(8):1169–1177, February 2016.

[36] William A. Shurcliff. *Polarized Light: Production and Use*. Harvard University Press, December 1962.

[37] Colin J. R. Sheppard. Jones and Stokes parameters for polarization in three dimensions. *Physical Review A*, 90(2):023809, August 2014.

[38] H. Kuwahara. Optical isolator for semiconductor lasers. *Applied Optics*, 19(2):319, January 1980.

[39] Fred M. Dickey, editor. *Laser beam shaping: theory and techniques*. CRC Press, Taylor & Francis Group, Boca Raton, second edition edition, 2014.

[40] J. H. Simmons and Kelly S. Potter. *Optical materials*. Academic Press, San Diego, 2000.

[41] L. D. Dickson. Characteristics of a Propagating Gaussian Beam. *Applied Optics*, 9(8):1854, August 1970.

[42] Zheng Kuang, Jiangning Li, Stuart Edwardson, Walter Perrie, Dun Liu, and Geoff Dearden. Ultrafast laser beam shaping for material processing at imaging plane by geometric masks using a spatial light modulator. *Optics and Lasers in Engineering*, 70:1–5, July 2015.

[43] Ashok Kumar, Pravin Vaity, and R.P. Singh. Diffraction characteristics of optical vortex passing through an aperture–iris diaphragm. *Optics Communications*, 283(21):4141–4145, November 2010.

[44] T. Kasuya, T. Suzuki, and K. Shimoda. A prism anamorphic system for Gaussian beam expander. *Applied Physics*, 17(2):131–136, October 1978.

[45] Madison Sutula, Ian Christen, Eric Bersin, Michael P. Walsh, Kevin C. Chen, Justin Mallek, Alexander Melville, Michael Titze, Edward S. Bielejec, Scott Hamilton, Danielle Braje, P. Benjamin Dixon, and Dirk R. Englund. Large-scale optical characterization of solid-state quantum emitters. *Nature Materials*, 22(11):1338–1344, November 2023.

[46] P. W. Kruse. The photon detection process. In Robert J. Keyes, editor, *Optical and Infrared Detectors*, volume 19, pages 5–69. Springer Berlin Heidelberg, Berlin, Heidelberg, 1980.

[47] Chandler Downs and Thomas Vandervelde. Progress in Infrared Photodetectors Since 2000. *Sensors*, 13(4):5054–5098, April 2013.

[48] A. Einstein. Über einen die Erzeugung und Verwandlung des Lichtes betreffenden heuristischen Gesichtspunkt. *Annalen der Physik*, 322(6):132–148, January 1905.

[49] Weixin Ouyang, Feng Teng, Jr-Hau He, and Xiaosheng Fang. Enhancing the Photoelectric Performance of Photodetectors Based on Metal Oxide Semiconductors by Charge-Carrier Engineering. *Advanced Functional Materials*, 29(9):1807672, February 2019.

[50] M. Ossiander, J. Riemensberger, S. Neppl, M. Mittermair, M. Schäffer, A. Duensing, M. S. Wagner, R. Heider, M. Wurzer, M. Gerl, M. Schnitzenbaumer, J. V. Barth, F. Libisch, C. Lemell, J. Burgdörfer, P. Feulner, and R. Kienberger. Absolute timing of the photoelectric effect. *Nature*, 561(7723):374–377, September 2018.

[51] D. Long. Photovoltaic and photoconductive infrared detectors. In Robert J. Keyes, editor, *Optical and Infrared Detectors*, pages 101–147. Springer, Berlin, Heidelberg, 1980.

[52] B.K. Lubsandorzhiev. On the history of photomultiplier tube invention. *Nuclear Instruments and Methods in Physics Research Section A: Accelerators, Spectrometers, Detectors and Associated Equipment*, 567(1):236–238, November 2006.

[53] G.E. Stillman and C.M. Wolfe. Chapter 5 Avalanche Photodiodes. In *Semiconductors and Semimetals*, volume 12, pages 291–393. Elsevier, 1977.

[54] Chandra M Natarajan, Michael G Tanner, and Robert H Hadfield. Superconducting nanowire single-photon detectors: physics and applications. *Superconductor Science and Technology*, 25(6):063001, June 2012.

[55] P. Martyniuk and A. Rogalski. Quantum-dot infrared photodetectors: Status and outlook. *Progress in Quantum Electronics*, 32(3-4):89–120, January 2008.

[56] L.F. Stokes. Selecting an optical spectrum analyzer. *IEEE Circuits and Devices Magazine*, 11(2):51–53, March 1995.

[57] M. Bertolotti. Photon Statistics. In H. Z. Cummins and E. R. Pike, editors, *Photon Correlation and Light Beating Spectroscopy*, pages 41–74. Springer US, Boston, MA, 1974.

[58] G. A. Morton. Photon Counting. *Applied Optics*, 7(1):1, January 1968.

[59] Joseph W. Goodman. *Statistical optics*. Wiley series in pure and applied optics. John Wiley & Sons Inc, Hoboken, New Jersey, second edition edition, 2015.

[60] Orazio Svelto, Stefano Longhi, Giuseppe Della Valle, Günter Huber, Stefan Kück, Markus Pollnau, Hartmut Hillmer, Thomas Kusserow, Rainer Engelbrecht, Frank Rohlfing, Jeffrey Kaiser, Ralf Malz, Gerd Marowsky, Klaus Mann, Peter Simon, Charles K. Rhodes, Frank J. Duarte, Annette Borsutzky, Johannes A. Lhuillier, Markus W. Sigrist, Helen Wächter, Evgeny Saldin, Evgeny Schneidmiller, Mikhail Yurkov, Roland Sauerbrey, Joachim Hein, Michele Gianella, Jürgen Helmcke, Katsumi Midorikawa, Fritz Riehle, Steffen Steinberg, and Hans Brand. Lasers and Coherent Light Sources. In Frank Träger, editor, *Springer Handbook of Lasers and Optics*, pages 641–1046. Springer Berlin Heidelberg, Berlin, Heidelberg, 2012.

[61] Milena D'Angelo, Aldo Mazzilli, Francesco V. Pepe, Augusto Garuccio, and Vincenzo Tamma. Characterization of two distant double-slits by chaotic light second-order interference. *Scientific Reports*, 7(1):2247, May 2017.

[62] Igor Aharonovich, Dirk Englund, and Milos Toth. Solid-state single-photon emitters. *Nature Photonics*, 10(10):631–641, October 2016.

[63] U. M. Titulaer and R. J. Glauber. Correlation Functions for Coherent Fields. *Physical Review*, 140(3B):B676–B682, November 1965.

[64] W.A. Ramadan, H.H. Wahba, and A.S. El-Tawargy. Enhanced short temporal coherence length measurement using Newton's rings interference. *Optics & Laser Technology*, 127:106192, July 2020.

[65] Malvin C. Teich and Bahaa E.A. Saleh. I Photon Bunching and Antibunching. In *Progress in Optics*, volume 26, pages 1–104. Elsevier, 1988.

[66] H. Paul. Photon antibunching. *Reviews of Modern Physics*, 54(4):1061–1102, October 1982.

[67] D. B. Scarl. Measurement of Photon Time-of-Arrival Distribution in Partially Coherent Light. *Physical Review Letters*, 17(12):663–666, September 1966.

[68] D N Klyshko and Anatolii V Masalov. Photon noise: observation, squeezing, interpretation. *Physics-Uspekhi*, 38(11):1203–1230, November 1995.

[69] K. M. Van Vliet. Noise Limitations in Solid State Photodetectors. *Applied Optics*, 6(7):1145, July 1967.

[70] Claude Cohen-Tannoudji, Jacques Dupont-Roc, and Gilbert Grynberg. *Atom—Photon Interactions: Basic Process and Appilcations*. Wiley, 1 edition, April 1998.

[71] N. Bohr. I. *On the constitution of atoms and molecules. The London, Edinburgh, and Dublin Philosophical Magazine and Journal of Science*, 26(151):1–25, July 1913.

[72] Albert Einstein. On the Quantum Theory of Radiation. *Physikalische Zeitschrift*, 18:121–128, 1917.

[73] B. R. Mollow. Stimulated Emission and Absorption near Resonance for Driven Systems. *Physical Review A*, 5(5):2217–2222, May 1972.

[74] D. L. Huber and J. H. Van Vleck. The Role of Boltzmann Factors in Line Shape. *Reviews of Modern Physics*, 38(1):187–204, January 1966.

[75] Max Planck. *The Theory of Heat Radiation*. 1914.

[76] A. Javan, W. R. Bennett, and D. R. Herriott. Population Inversion and Continuous Optical Maser Oscillation in a Gas Discharge Containing a He-Ne Mixture. *Physical Review Letters*, 6(3):106–110, February 1961.

[77] William Happer. Optical Pumping. *Reviews of Modern Physics*, 44(2):169–249, April 1972.

[78] I. A. Walmsley. Quantum optics: Science and technology in a new light. *Science*, 348(6234):525–530, May 2015.

[79] Stephen M. Barnett and Paul M. Radmore. *Methods in Theoretical Quantum Optics*. Oxford University PressOxford, 1 edition, November 2002.

[80] Louis de Broglie. *Recherches sur la théorie des quanta*. PhD thesis, Paris, 1924.

[81] Erwin Schrödinger. 2. Quantisierung als Eigenwertproblem. In *Wellenmechanik*, pages 108–122. De Gruyter, December 1969.

[82] N. Bohr. The Quantum Postulate and the Recent Development of Atomic Theory1. *Nature*, 121(3050):580–590, April 1928.

[83] Jonathan R. Friedman, Vijay Patel, W. Chen, S. K. Tolpygo, and J. E. Lukens. Quantum superposition of distinct macroscopic states. *Nature*, 406(6791):43–46, July 2000.

[84] C. C. Gerry and P. L. Knight. Quantum superpositions and Schrödinger cat states in quantum optics. *American Journal of Physics*, 65(10):964–974, October 1997.

[85] William Marshall, Christoph Simon, Roger Penrose, and Dik Bouwmeester. Towards Quantum Superpositions of a Mirror. *Physical Review Letters*, 91(13):130401, September 2003.

[86] Ryszard Horodecki, Paweł Horodecki, Michał Horodecki, and Karol Horodecki. Quantum entanglement. *Reviews of Modern Physics*, 81(2):865–942, June 2009.

[87] John Von Neumann. *Mathematische Grundlagen der Quantenmechanik*. Springer Berlin Heidelberg, Berlin, Heidelberg, 1996.

[88] Lluís Masanes, Yeong-Cherng Liang, and Andrew C. Doherty. All Bipartite Entangled States Display Some Hidden Nonlocality. *Physical Review Letters*, 100(9):090403, March 2008.

[89] Nicolas Brunner, Daniel Cavalcanti, Stefano Pironio, Valerio Scarani, and Stephanie Wehner. Bell nonlocality. *Reviews of Modern Physics*, 86(2):419–478, April 2014.

[90] Christophe Couteau. Spontaneous parametric down-conversion. *Contemporary Physics*, 59(3):291–304, July 2018.

[91] Morton H. Rubin, David N. Klyshko, Y. H. Shih, and A. V. Sergienko. Theory of two-photon entanglement in type-II optical parametric down-conversion. *Physical Review A*, 50(6):5122–5133, December 1994.

[92] Jesse Catalano. *Spontaneous Parametric Down-Conversion and Quantum Entanglement*. PhD thesis, Portland State University, June 2014.

[93] E. Schrödinger. Die gegenwärtige Situation in der Quantenmechanik. *Die Naturwissenschaften*, 23(48):807–812, November 1935.

[94] Iman Shames, Adrian N. Bishop, Matthew Smith, and Brian D. O. Anderson. Doppler Shift Target Localization. *IEEE Transactions on Aerospace and Electronic Systems*, 49(1):266–276, January 2013.

[95] Y. Takeda. Velocity profile measurement by ultrasound Doppler shift method. *International Journal of Heat and Fluid Flow*, 7(4):313–318, December 1986.

[96] Yanghe Shen, Luping Xu, Hua Zhang, and Peng Yang. Doppler shift and ambiguity velocity caused by relative motion in quantum-enhanced measurement. *Optics Express*, 23(14):18445, July 2015. Number: 14.

[97] Christian Doppler and Frantisek Josef Studnica. *Ueber das farbige licht der doppelsterne und einiger anderer gestirne des himmels*. January 1903. ADS Bibcode: 1903udfl.book.....D.

[98] Mark L. Psiaki. Navigation using carrier Doppler shift from a LEO constellation: TRANSIT on steroids. *NAVIGATION*, 68(3):621–641, September 2021.

[99] Aleksandar Gjurchinovski. The Doppler effect from a uniformly moving mirror. *European Journal of Physics*, 26(4):643–646, July 2005. Number: 4.

[100] A. Einstein. Zur allgemeinen molekularen Theorie der Wärme [AdP 14, 354 (1904)]. *Annalen der Physik*, 517(S1):154–163, February 2005.

[101] Ali Anwar, Chithrabhanu Perumangatt, Fabian Steinlechner, Thomas Jennewein, and Alexander Ling. Entangled photon-pair sources based on three-wave mixing in bulk crystals. *Review of Scientific Instruments*, 92(4):041101, April 2021.

[102] Bikash Kumar Das. A Brief Review on Choice of Non-Linear Crystals for Spontaneous Parametric down Conversion. *SSRN Electronic Journal*, 2021.

[103] Manuel Erhard, Mario Krenn, and Anton Zeilinger. Advances in high-dimensional quantum entanglement. *Nature Reviews Physics*, 2(7):365–381, June 2020.

[104] C. K. Hong, Z. Y. Ou, and L. Mandel. Measurement of subpicosecond time intervals between two photons by interference. *Physical Review Letters*, 59(18):2044–2046, November 1987.

[105] James Schneeloch, Samuel H Knarr, Daniela F Bogorin, Mackenzie L Levangie, Christopher C Tison, Rebecca Frank, Gregory A Howland, Michael L Fanto, and Paul M Alsing. Introduction to the absolute brightness and number statistics in spontaneous parametric down-conversion. *Journal of Optics*, 21(4):043501, April 2019. Number: 4.

[106] M. V. Jabir and G. K. Samanta. Robust, high brightness, degenerate entangled photon source at room temperature. *Scientific Reports*, 7(1):12613, December 2017. Number: 1.

[107] Özgün Süzer and Theodore G. Goodson. Does pump beam intensity affect the efficiency of spontaneous parametric down conversion? *Optics Express*, 16(25):20166, December 2008.

[108] Craig Hoffman and Ronald Driggers. *Encyclopedia of Optical and Photonic Engineering (Print) - Five Volume Set*. CRC Press, Boca Raton, 2 edition, September 2015.

[109] Fabian Steinlechner, Pavel Trojek, Marc Jofre, Henning Weier, Daniel Perez, Thomas Jennewein, Rupert Ursin, John Rarity, Morgan W. Mitchell, Juan P. Torres, Harald Weinfurter, and Valerio Pruneri. A high-brightness source of polarization-entangled photons optimized for applications in free space. *Optics Express*, 20(9):9640, April 2012.

[110] Sang Min Lee, Heonoh Kim, Myoungsik Cha, and Han Seb Moon. Polarization-entangled photon-pair source obtained via type-II non-collinear SPDC process with PPKTP crystal. *Optics Express*, 24(3):2941, February 2016.

[111] Guoxin Li, Yukun Wang, Lixiang Huang, and Wenhong Sun. Research Progress of High-Sensitivity Perovskite Photodetectors: A Review of Photodetectors: Noise, Structure, and Materials. *ACS Applied Electronic Materials*, 4(4):1485–1505, April 2022.

[112] Quntao Zhuang, Zheshen Zhang, and Jeffrey H. Shapiro. Entanglement-enhanced lidars for simultaneous range and velocity measurements. *Physical Review A*, 96(4):040304, October 2017. Number: 4.

[113] E G Lariontsev. Quantum interference of biphotons with a Doppler frequency shift. *Quantum Electronics*, 46(8):749–752, August 2016. Number: 8.

[114] Marin Soljačić, Steven G. Johnson, Shanhui Fan, Mihai Ibanescu, Erich Ippen, and J. D. Joannopoulos. Photonic-crystal slow-light enhancement of nonlinear phase sensitivity. *Journal of the Optical Society of America B*, 19(9):2052, September 2002.

[115] Quntao Zhuang. Quantum Ranging with Gaussian Entanglement. *Physical Review Letters*, 126(24):240501, June 2021. Number: 24.

[116] L J Wang, C K Hong, and S R Friberg. Generation of correlated photons via four-wave mixing in optical fibres. *Journal of Optics B: Quantum and Semiclassical Optics*, 3(5):346–352, October 2001.

[117] John Kerr. XL. *A new relation between electricity and light: Dielectrified media birefringent. The London, Edinburgh, and Dublin Philosophical Magazine and Journal of Science*, 50(332):337–348, November 1875.

[118] Sunish Kumar Orappanpara Soman. A tutorial on fiber Kerr nonlinearity effect and its compensation in optical communication systems. *Journal of Optics*, 23(12):123502, December 2021.

[119] Ichiro Shoji, Takashi Kondo, Ayako Kitamoto, Masayuki Shirane, and Ryoichi Ito. Absolute scale of second-order nonlinear-optical coefficients. *Journal of the Optical Society of America B*, 14(9):2268, September 1997.

[120] Aleksei Zheltikov. Analytical insights into self-phase modulation: beyond the basic theory. *Optics Express*, 26(13):17571, June 2018.

[121] Nils Krebs, Igor Pugliesi, and Eberhard Riedle. Pulse Compression of Ultrashort UV Pulses by Self-Phase Modulation in Bulk Material. *Applied Sciences*, 3(1):153–167, February 2013.

[122] A.C. Scott, F.Y.F. Chu, and D.W. McLaughlin. The soliton: A new concept in applied science. *Proceedings of the IEEE*, 61(10):1443–1483, 1973.

[123] B. Dubetsky and P. R. Berman. Theory of four-wave mixing using an amplitude approach. *Physical Review A*, 47(2):1294–1313, February 1993.

[124] R. Baumgartner and R. Byer. Optical parametric amplification. *IEEE Journal of Quantum Electronics*, 15(6):432–444, June 1979.

[125] S. J. Jung, J. Y. Lee, and D. Y. Kim. Novel phase-matching condition for a four wave mixing experiment in an optical fiber. *Optics Express*, 14(1):35, 2006.

[126] Jay E. Sharping, Marco Fiorentino, Ayodeji Coker, Prem Kumar, and Robert S. Windeler. Four-wave mixing in microstructure fiber. *Optics Letters*, 26(14):1048, July 2001.

[127] Thomas Rappen, Ulf-Gereon Peter, Martin Wegener, and Wilfried Schäfer. Polarization dependence of dephasing processes: A probe for many-body effects. *Physical Review B*, 49(15):10774–10777, April 1994.

[128] C.A. Brackett. Dense wavelength division multiplexing networks: principles and applications. *IEEE Journal on Selected Areas in Communications*, 8(6):948–964, August 1990.

[129] Luís A. Fernandes, Jason R. Grenier, Peter R. Herman, J. Stewart Aitchison, and Paulo V. S. Marques. Stress induced birefringence tuning in femtosecond laser fabricated waveguides in fused silica. *Optics Express*, 20(22):24103, October 2012.

[130] Shin-Ichi Todoroki. *Fiber fuse: light-induced continuous breakdown of silica glass optical fiber*. NIMS monographs. Springer, Tokyo ; New York, 2014. OCLC: ocn863191770.

[131] Z.Y. Ou, C.K. Hong, and L. Mandel. Relation between input and output states for a beam splitter. *Optics Communications*, 63(2):118–122, July 1987.

[132] Yuanyuan Chen, Sebastian Ecker, Sören Wengerowsky, Lukas Bulla, Siddarth Koduru Joshi, Fabian Steinlechner, and Rupert Ursin. Polarization Entanglement by Time-Reversed Hong-Ou-Mandel Interference. *Physical Review Letters*, 121(20):200502, November 2018. Number: 20.

[133] Mehmet Fatih Yanik and Shanhui Fan. Time Reversal of Light with Linear Optics and Modulators. *Physical Review Letters*, 93(17):173903, October 2004.

[134] Y. Aharonov and D. Bohm. Significance of Electromagnetic Potentials in the Quantum Theory. *Physical Review*, 115(3):485–491, August 1959.

[135] B. E. Allman, A. Cimmino, A. G. Klein, G. I. Opat, H. Kaiser, and S. A. Werner. Scalar Aharonov-Bohm experiment with neutrons. *Physical Review Letters*, 68(16):2409–2412, April 1992.

[136] Samuel A Werner and Anthony G Klein. Observation of Aharonov–Bohm effects by neutron interferometry. *Journal of Physics A: Mathematical and Theoretical*, 43(35):354006, September 2010.

[137] R. G. Chambers. Shift of an Electron Interference Pattern by Enclosed Magnetic Flux. *Physical Review Letters*, 5(1):3–5, July 1960.

[138] Shigeru Nakayama. Theoretical Analysis of Rb and Cs D $_2$ Lines in Saturation Spectroscopy with Optical Pumping. *Japanese Journal of Applied Physics*, 23(7R):879, July 1984.

[139] Shigeru Nakayama. Theoretical Analysis of Rb and Cs D $_2$ Lines in Doppler-Free Spectroscopic Techniques with Optical Pumping. *Japanese Journal of Applied Physics*, 24(1R):1, January 1985.

[140] M G Bason, A K Mohapatra, K J Weatherill, and C S Adams. Narrow absorptive resonances in a four-level atomic system. *Journal of Physics B: Atomic, Molecular and Optical Physics*, 42(7):075503, April 2009.

[141] F. E. Neumann. Allgemeine Gesetze der inducirten elektrischen Ströme. *Annalen der Physik*, 143(1):31–44, January 1846.

[142] S. H. Autler and C. H. Townes. Stark Effect in Rapidly Varying Fields. *Physical Review*, 100(2):703–722, October 1955.

[143] J.S. Bakos. AC stark effect and multiphoton processes in atoms. *Physics Reports*, 31(3):209–235, July 1977.

[144] Philip D. Gregory, Jacob A. Blackmore, Jesus Aldegunde, Jeremy M. Hutson, and Simon L. Cornish. ac Stark effect in ultracold polar Rb 87 Cs 133 molecules. *Physical Review A*, 96(2):021402, August 2017.

[145] F. Levi, J. Camparo, B. Francois, C. E. Calosso, S. Micalizio, and A. Godone. Precision test of the ac Stark shift in a rubidium atomic vapor. *Physical Review A*, 93(2):023433, February 2016.

[146] Chang Yong Park, Heeso Noh, Chung Mok Lee, and D. Cho. Measurement of the Zeeman-like ac Stark shift. *Physical Review A*, 63(3):032512, February 2001.

[147] E. Brekke and C. Umland. Rydberg excitation through detuned microwave transition in rubidium. *Journal of the Optical Society of America B*, 40(11):2758, November 2023.

[148] R. Y. Chiao, H. Hart, M. Scheibner, J. Sharping, N. A. Inan, D. A. Singleton, and M. E. Tobar. Energy-level shift of quantum systems via the scalar electric Aharonov-Bohm effect. *Physical Review A*, 107(4):042209, April 2023.

[149] P. J. Chantry. Doppler Broadening in Beam Experiments. *The Journal of Chemical Physics*, 55(6):2746–2759, September 1971.

[150] Alexander Kramida and Yuri Ralchenko. NIST Atomic Spectra Database, NIST Standard Reference Database 78, 1999.

[151] Daryl W. Preston. Doppler-free saturated absorption: Laser spectroscopy. *American Journal of Physics*, 64(11):1432–1436, November 1996.

[152] Hyun-Jong Kang and Heung-Ryoul Noh. Coherence effects in electromagnetically induced transparency in V-type systems of ˆ87Rb. *Optics Express*, 25(18):21762, September 2017.

[153] Yong-qing Li and Min Xiao. Electromagnetically induced transparency in a three-level -type system in rubidium atoms. *Physical Review A*, 51(4):R2703–R2706, April 1995.

[154] Ulrich Platt and Jochen Stutz. Differential Absorption Spectroscopy. In *Differential Optical Absorption Spectroscopy*, pages 135–174. Springer Berlin Heidelberg, Berlin, Heidelberg, 2008.

[155] R. Van Leeuwen, E. Van Lenthe, E. J. Baerends, and J. G. Snijders. Exact solutions of regular approximate relativistic wave equations for hydrogen-like atoms. *The Journal of Chemical Physics*, 101(2):1272–1281, July 1994.

[156] Ho Seong Lee, Sang Eon Park, Jong Dae Park, and Hyuck Cho. Zeeman effect in the saturation spectroscopy of the ˆ87Rb D_2 line. *Journal of the Optical Society of America B*, 11(4):558, April 1994.

[157] D. J. McCarron, H. W. Cho, D. L. Jenkin, M. P. Köppinger, and S. L. Cornish. Dual-species Bose-Einstein condensate of Rb 87 and Cs 133. *Physical Review A*, 84(1):011603, July 2011.

[158] Makoto Matsui, Kimiya Komurasaki, Satoshi Ogawa, and Yoshihiro Arakawa. Influence of laser intensity on absorption line broadening in laser absorption spectroscopy. *Journal of Applied Physics*, 100(6):063102, September 2006.

[159] Jacob B. Khurgin and Rodney S. Tucker, editors. *Slow Light: Science and Applications*. CRC Press, 0 edition, October 2018.

[160] J. P. Marangos. Electromagnetically induced transparency. *Journal of Modern Optics*, 45(3):471–503, March 1998.

[161] A. Lezama, S. Barreiro, and A. M. Akulshin. Electromagnetically induced absorption. *Physical Review A*, 59(6):4732–4735, June 1999.

[162] Bankim Chandra Das, Arpita Das, Dipankar Bhattacharyya, Shrabana Chakrabarti, and Sankar De. Interplay between electromagnetically induced transparency (EIT), absorption (EIA), and Autler-Townes (AT) splitting in an N -type atomic system: experiment and theory. *OSA Continuum*, 2(3):994, March 2019.

[163] Chandan Das, Sekhar Dey, and Biswajit Ray. Study of EIT line shape in optically thin and thick media using ^{87} Rb D $_1$ and D $_2$ lines: theory and experiment. *Physica Scripta*, 97(9):095401, September 2022.

[164] Hoon Yu, Jung Dong Kim, Tae Young Jung, and Jung Bog Kim. Transformation of EIA to EIT by incoherent pumping of the 85Rb D1 line. *Journal of the Korean Physical Society*, 61(8):1227–1231, October 2012.

[165] A. M. Akulshin, S. Barreiro, and A. Lezama. Electromagnetically induced absorption and transparency due to resonant two-field excitation of quasidegenerate levels in Rb vapor. *Physical Review A*, 57(4):2996–3002, April 1998.

[166] J. L. Hall. Saturated Absorption Spectroscopy with Applications to the 3.39 m Methane Transition. In *Atomic Physics 3*, pages 615–646. Springer US, Boston, MA, 1973.

[167] Wenhao Bu, Yuhe Zhang, Qian Liang, Tao Chen, and Bo Yan. Saturated absorption spectroscopy of buffer-gas-cooled Barium monofluoride molecules. *Frontiers of Physics*, 17(6):62502, December 2022.

[168] Qian-Hao Liu, Ya-Nan Lv, Chang-Ling Zou, Cun-Feng Cheng, and Shui-Ming Hu. Saturated absorption spectroscopy of HD at 76 K. *Physical Review A*, 106(6):062805, December 2022.

[169] Ralf Behr, Oliver Kieler, and Bernd Schumacher. A Precision Microvolt-Synthesizer Based on a Pulse-Driven Josephson Voltage Standard. *IEEE Transactions on Instrumentation and Measurement*, 66(6):1385–1390, June 2017.

[170] T. Yamamoto, T. Komukai, K. Suzuki, and A. Takada. Multicarrier Light Source With Flattened Spectrum Using Phase Modulators and Dispersion Medium. *Journal of Lightwave Technology*, 27(19):4297–4305, October 2009.

[171] Babak Dastmalchi, Philippe Tassin, Thomas Koschny, and Costas M. Soukoulis. Strong group-velocity dispersion compensation with phase-engineered sheet metamaterials. *Physical Review B*, 89(11):115123, March 2014.

[172] Yunhui Zhu, Joel A. Greenberg, Nor Ain Husein, and Daniel J. Gauthier. Giant all-optical tunable group velocity dispersion in an optical fiber. *Optics Express*, 22(12):14382, June 2014.

[173] Oguz Tolga Celik, Christopher J. Sarabalis, Felix M. Mayor, Hubert S. Stokowski, Jason F. Herrmann, Timothy P. McKenna, Nathan R. A. Lee, Wentao Jiang, Kevin K. S. Multani, and Amir H. Safavi-Naeini. High-bandwidth CMOS-voltage-level electro-optic modulation of 780 nm light in thin-film lithium niobate. *Optics Express*, 30(13):23177, June 2022.

[174] Lorenzo Leandro, Jacob Hastrup, Rodion Reznik, George Cirlin, and Nika Akopian. Resonant excitation of nanowire quantum dots. *npj Quantum Information*, 6(1):93, December 2020.

[175] Guozhen Liang, Heqing Huang, Aseema Mohanty, Min Chul Shin, Xingchen Ji, Michael Joseph Carter, Sajan Shrestha, Michal Lipson, and Nanfang Yu. Robust, efficient, micrometre-scale phase modulators at visible wavelengths. *Nature Photonics*, 15(12):908–913, December 2021.

[176] Seitaro Tani, Yuma Sato, Shun Harada, Zheqing Sun, Shuhei Otsuka, Tatsuki Ishijima, and Takahide Sakamoto. Endless Spatial Optical Phase Modulation by Complex Vector Synthesis Using LCoS. In *2024 Conference on Lasers and Electro-Optics Pacific Rim (CLEO-PR) (2024), paper Th1K_2*, page Th1K_2. Optica Publishing Group, August 2024.

[177] William Davis, Paul Burdekin, Tabijah Wasawo, Sarah E Thomas, Peter J Mosley, Joshua Nunn, and Cameron McGarry. Fast, low-loss all-optical phase modulation in warm rubidium vapour, 2023.

[178] I. Magnus, M. Virte, H. Thienpont, and L. Smeesters. Combining optical spectroscopy and machine learning to improve food classification. *Food Control*, 130:108342, December 2021.

[179] Xinzhong Chen, Ziheng Yao, Suheng Xu, Alexander S. McLeod, Stephanie N. Gilbert Corder, Yueqi Zhao, Makoto Tsuneto, Hans A. Bechtel, Michael C. Martin, G. Lawrence Carr, Michael M. Fogler, Stefan G. Stanciu, D. N. Basov, and Mengkun Liu. Hybrid Machine Learning for Scanning Near-Field Optical Spectroscopy. *ACS Photonics*, 8(10):2987–2996, October 2021.

[180] Joonyoung F. Joung, Minhi Han, Jinhyo Hwang, Minseok Jeong, Dong Hoon Choi, and Sungnam Park. Deep Learning Optical Spectroscopy Based on Experimental Database: Potential Applications to Molecular Design. *JACS Au*, 1(4):427–438, April 2021.

[181] Carlos A. Meza Ramirez, Michael Greenop, Lorna Ashton, and Ihtesham Ur Rehman. Applications of machine learning in spectroscopy. *Applied Spectroscopy Reviews*, 56(8-10):733–763, November 2021.

[182] Tomasz Szandała. Review and Comparison of Commonly Used Activation Functions for Deep Neural Networks. In Akash Kumar Bhoi, Pradeep Kumar Mallick, Chuan-Ming Liu, and Valentina E. Balas, editors, *Bio-inspired Neurocomputing*, pages 203–224. Springer, Singapore, 2021.

[183] Mustafa Yildirim, Niyazi Ulas Dinc, Ilker Oguz, Demetri Psaltis, and Christophe Moser. Nonlinear processing with linear optics. *Nature Photonics*, 18(10):1076–1082, October 2024.

[184] Tohru Ishihara, Jun Shiomi, Naoki Hattori, Yutaka Masuda, Akihiko Shinya, and Masaya Notomi. An Optical Neural Network Architecture based on Highly Parallelized WDM-Multiplier-Accumulator. In *2019 IEEE/ACM Workshop on Photonics-Optics Technology Oriented Networking, Information and Computing Systems (PHOTONICS)*, pages 15–21, Denver, CO, USA, November 2019. IEEE.

[185] Xingyuan Xu, Mengxi Tan, Bill Corcoran, Jiayang Wu, Thach G. Nguyen, Andreas Boes, Sai T. Chu, Brent E. Little, Roberto Morandotti, Arnan Mitchell, Damien G. Hicks, and David J. Moss. Photonic Perceptron Based on a Kerr Microcomb for High-Speed, Scalable, Optical Neural Networks. *Laser & Photonics Reviews*, 14(10):2000070, October 2020.

[186] Runqin Xu, Pin Lv, Fanjiang Xu, and Yishi Shi. A survey of approaches for implementing optical neural networks. *Optics & Laser Technology*, 136:106787, April 2021.

[187] Tianyu Wang, Shi-Yuan Ma, Logan G. Wright, Tatsuhiro Onodera, Brian C. Richard, and Peter L. McMahon. An optical neural network using less than 1 photon per multiplication. *Nature Communications*, 13(1):123, January 2022.

[188] Tianyu Wang, Mandar M. Sohoni, Logan G. Wright, Martin M. Stein, Shi-Yuan Ma, Tatsuhiro Onodera, Maxwell G. Anderson, and Peter L. McMahon. Image sensing with multilayer nonlinear optical neural networks. *Nature Photonics*, 17(5):408–415, May 2023.

[189] Wojciech Samek, Grégoire Montavon, Sebastian Lapuschkin, Christopher J. Anders, and Klaus-Robert Müller. Explaining Deep Neural Networks and Beyond: A Review of Methods and Applications. *Proceedings of the IEEE*, 109(3):247–278, March 2021.

[190] Frank Rosenblatt. The Perceptron: A Probabilistic Model for Information Storage and Organization (1958). In *Ideas That Created the Future*, pages 183–190. The MIT Press, February 2021.

[191] Luis B. Almeida. Multilayer perceptrons. In *Handbook of Neural Computation*. CRC Press, 1996.

[192] Athindran Ramesh Kumar and Peter J. Ramadge. DiffLoop: Tuning PID Controllers by Differentiating Through the Feedback Loop. In *2021 55th Annual Conference on Information Sciences and Systems (CISS)*, pages 1–6, Baltimore, MD, USA, March 2021. IEEE.